2008

# Analysis and design of metal-surface mounted radio frequency identification (RFID) transponders

Sanyi Zhan
*Iowa State University*

# Analysis and design of metal-surface mounted radio frequency identification (RFID) transponders

by

**Sanyi Zhan**

A dissertation submitted to the graduate faculty

in partial fulfillment of the requirements for the degree of

DOCTOR OF PHILOSOPHY

Major: Electrical Engineering

Program of Study Committee:
Robert J. Weber, Co-major Professor
Jiming Song, Co-major Professor
John R. Bowler,
Akhilesh Tyagi
Jaeyoun Kim

Iowa State University

Ames, Iowa
2008

# Table of Contents

# LIST OF FIGURES

# LIST OF TABLES

# ASTRACT

With the development of the radio frequency integrated circuit (RFIC), contactless radio frequency identification (RFID) technology, as one of the fastest growing sectors of automatic identification procedures (Auto-ID), gains broad application in tracking assets in supply chain management. However, one of the largest challenges for the RFID industry is that the ultra high frequency (UHF) RFID transponder doesn't function well when it is applied to any conductive surface. In this dissertation, the communication principle of wireless transceivers is illustrated. As one fast-growing application field of wireless communication, the distinct operating principle of the RFID is clarified. The factors that limit the reading/writing distance of UHF RFID transponders are discussed in detail. Some potential solutions are proposed and verified. One nondestructive solution is to apply a metamaterial such as a frequency selective surface (FSS) or a mushroom-like electromagnetic bandgap (EBG) surface to block the transmission of electromagnetic waves from the RFID antenna to the metal ground and thus boost the antenna radiation efficiency. For this solution, a new design approach suppressing the TM wave but supporting the TE wave is demonstrated. Another low-cost solution is to use an inexpensive substrate material and obtain the most power-efficient antenna structure. More than six potentially patentable planar RFID transponder antennas were invented, designed and tested. Their compact size, low profile, low cost and superior performance paves the way for the RFID industry to expand their market share in the near future.

# CHAPTER 1 OVERVIEW

## 1.1 Introduction

Automatic identification procedures (Auto-ID) extract distinct information about people, animals and a variety of items. It includes the barcode system, optical character recognition (OCR), smart cards, RFID and voice and fingerprinting identifications. Smart cards and RFID systems have their maximum data capacity due to the development of integrated circuits. Most of the above identification procedures work over short distances (less than 50 cm). It is no surprise that by virtue of RF technology, the RFID, with the capability to read and write information remotely, will dominate the Auto-ID market in the near future.

### 1.1.1 A simple history of RFID

Electromagnetic energy exists everywhere in the universe. Although electromagnetic energy existed at the very beginning of our existence, it took a long journey for us to understand it and further learn how to harness it. Since Maxwell unified the equations to describe the phenomena of electricity and magnetism, our ability to utilize the hidden energy grew. An early paper by Harry Stockman titled “Communication by Means of Reflected Power” [1] predicted that "…considerable research and development work has to be done before the remaining basic problems in reflected-power communication are solved, and before the field of useful applications is explored." This paper explored the theoretical background about using backscattering to communicate remotely.

Electromagnetic waves can be applied to carry information and transmit through a long

distance. It has been applied to wireless communication and remote sensing. As a part of remote sensing or remote identification, the predecessor to RFID was first reported as an espionage tool which was invented by Leon Theremin in 1946 [2]. It can modulate incident radio waves with audio information and re-send them.

Since the 1970s, with the development of radio frequency integrated circuits and antenna theory, UHF passive and active RFID by using backscattering to communicate remotely became possible. Since the 1980s, the commercial application of RFID began and has exploded. In 21$^{st}$ century, radio frequency CMOS integrated circuits became mainstream, which further lowers the cost to implement a RFID system. In 2008, the major semiconductor companies have adopted 45 nm CMOS technology to design wireless transceivers, which further reduces the cost of RF transceiver. It can be seen in the near future, with a reduced cost to adopt a RFID system, the applications of RFID will expand further. For passive and active UHF RFID tags, one of the major challenges is to search for faster nonvolatile memory to replace electrically erasable programmable read-only memory (EEPROM), which should be suitable for the low power characteristics of RFID. Since the transponder size,

Table 1.1 Time table of the RFID history

| Time | The development of RFID |
|---|---|
| 1940 ~ 1950 | Radar technology becomes mature due to the effort of World war II. RFID is invented in 1946. |
| 1950 ~ 1960 | Theoretical and laboratory explorations of RFID technology. |
| 1960 ~ 1970 | The theory of RFID is developed. The application trial starts. |
| 1970 ~ 1980 | The early implementation of RFID |
| 1980 ~ 1990 | Commercial applications of RFID grow |
| 1990 ~ 2000 | RFID standards emerge. |
| 2000 ~ 2008 | 600nm~45nm CMOS RF transceiver dominates the market. The estimated RFID market is $ 7.26 billion in 2008 [3]. |

performance and cost are dominantly determined by the RFID antennas, the design of antennas becomes more important. A simple time table for RFID history modified from [2] is shown in Table. 1.1.

### 1.1.2 Types of RFID

RFID tags or transponders can be named as passive or active. A passive RFID tag means the device doesn't have a fixed DC power supply. The power needed to power the RFID transponder is extracted from the incident electromagnetic wave. An active RFID tag is given a fixed DC power supply and thus has a longer reading range. The wireless communication for an active RFID is not very sensitive to the environment. However considering the high volume demand for supply chain management, the cost of an active RFID in the range of a few dollars per unit is still too high. A passive RFID tag is the potential alternative to replace the traditional barcode system due to its low cost ($0.05 ~ $ 0.2 each) and superior performance.

RFID can operate in various frequency bands, which covers from 0~135 KHz, and the ISM (Industrial-Scientific-Medical) frequency ranges like 6.78 MHz, 13.56 MHz, 27.125 MHz, 40.68 MHz, 433.92 MHz, 869.0 MHz (Europe), 915.0 MHz (US), 2.45 GHz, 5.8 GHz and 24.125 GHz [4]. Although the market share of the HF RFID (13.56 MHz) is the largest among all of the RFIDs, the market of UHF (ultra high frequency) RFID transponders grew quickly due to the perfect compromise between reading distance and antenna size.

HF RFID utilizes the effects of magnetic coupling and load modulation to realize near-field communication. In the reactive near field region, which is defined as $0.62\sqrt{D^3/\lambda} > r > 0$ [5],

the magnetic field is inversely proportional to $r^3$, where $D$ is the maximum dimension of the antenna, $\lambda$ is the wavelength of the radiated electromagnetic wave, and $r$ is the distance from the radiation source (antenna) to the observer. Therefore the magnetic field decreases over distance at a rate of 60 dB per decade. The maximum readable range for a RFID tag at low frequency will be low (typically less than 1 m). The inductive coupling between the reader coil and the transponder antenna can be effectively modeled as a transformer with mutual inductance. A systematic analysis will be simplified by this equivalent circuit approach. Once the load impedance is varied due to the load modulation, the effects will be shown as a variance of the input impedance at the source terminal of the transformer.

In the far field (Fraunhofer) region, which is defined by $r > 2D^2 / \lambda$ [5], the field decays at the rate of $1/r$. Therefore the fields decay over distance at a rate of 20 dB per decade. By virtue of backscattering technology, the reading/writing distance can be much larger (about 10 meters). The data rate can be much higher due to the larger bandwidth in the UHF frequency band. In this dissertation, we concentrate on the UHF RFID transponders.

### 1.1.3 Market of RFID

As one of the fastest growing sectors of automatic identification procedures (Auto-ID), contactless radio frequency identification (RFID) technology has gained broad application for tracking assets in supply chain management. More retailers are replacing the traditional barcode with an RFID tag to save their labor and cost. It has also become an integral part of our life. It can be used to track animals or library books, control the entrance to buildings or manage traffic.

Compared with the optical barcode system, RFID has the advantage of a much longer reading range, is reprogrammable, and has a larger information storage capacity. In the semiconductor industry, with a smaller feature size, a lower cost of the chip is expected. The unit cost of a RFID chip has continuously decreased. As one can imagine, when the cost of a RFID tag becomes comparable to a barcode, RFID would fully replace the barcode eventually. According to ID TechEx, the trend of replacing the barcode has now appeared since the RFID market is going to reach 7.26 billion in 2008 [3].

### 1.1.4 Basic principle of RFID

As a method of wireless communication, a RFID system includes a RFID reader, a RFID chip and a RFID transponder antenna. The data or information stored in a silicon chip can be retrieved by a RFID reader through the RFID transponder antenna. A low cost passive RFID transponder doesn't include any internal DC power supply. The RFID reader sends both information and power to the RFID tag by virtue of electromagnetic waves. The RFID tag is

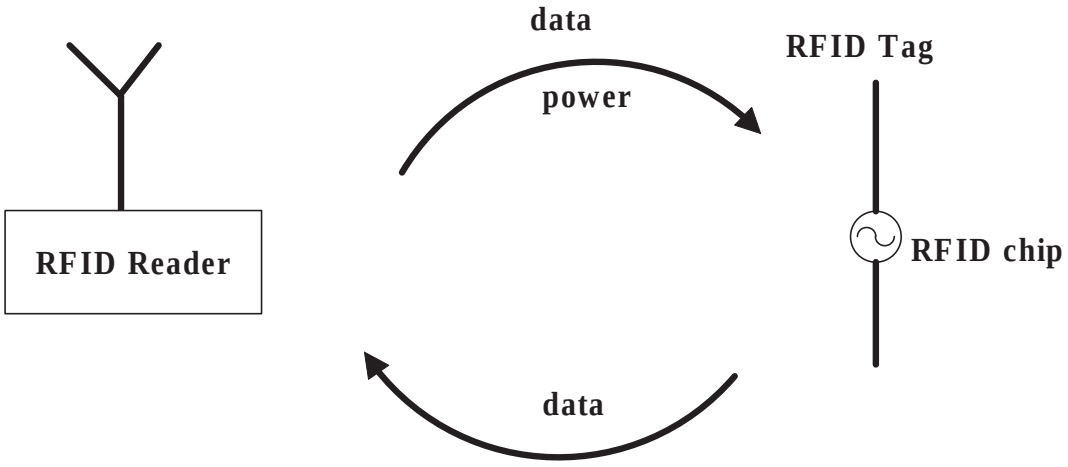


Fig. 1.1 A simplified RFID system

able to receive the incident radio frequency (RF) power and extract the data sent by the RFID reader by demodulation. In the reading stage, the data stored in the chip modulates the impedance of the RFID tag antenna so that the backscattering waves are different for a digit "0" or a digit "1". Then the reader retrieves the data sent by the RFID transponder. Fig. 1.1 shows the simplified RFID system.

### 1.1.5 RFID transponder on metal surface

As one of the largest challenges for the radio frequency identification (RFID) industry, the RIFD tag can't be read with dipole type antennas when the antennas are attached to a conductive surface. Fig. 1.2 shows an example of a passive RFID tag, which is unable to be read if it is placed above a conductive surface.

Fig. 1.2 A passive RFID tag (Courtesy of Alien Technology)

The reason why the dipole type RFID tag can not be read is simply explained in Fig. 1.3, which shows that the image dipole below the metal surface has an equal but opposite current from that of the original dipole. If the space between the dipole and its image is very small (much less than one wavelength), then the total effective current approaches zero. Therefore the total radiation field is negligible. The RFID is then unable to capture data and power from the reader.

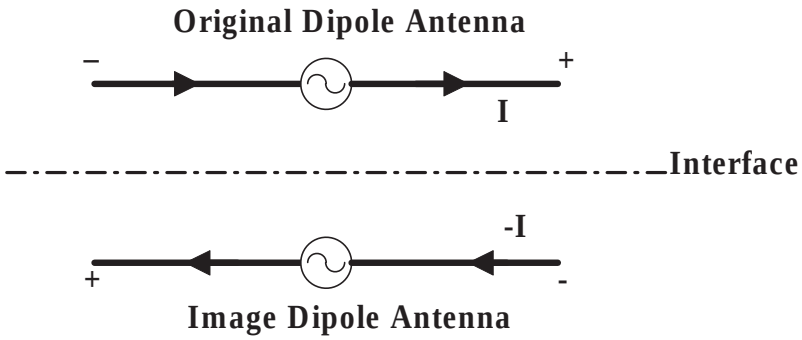


Fig. 1.3 A dipole antenna above a perfect electric conductor (PEC) and its image

### 1.1.6 Goal of this dissertation

There is a big portion of the RFID market which needs the RFID attached to metal or conductive surfaces. It is well known that the dipole type antenna is unable to radiate well on metal. There is no good available solution for this problem. In fall of 2005, as a major provider for automatic ID tags, Metalcraft I.D. Plates and Labels desired to find a solution to this problem. Metalcraft and ISU's IPRT Company Assistance co-funded a research project, which resulted in a major portion of this dissertation. Our goal was to develop a method to allow a RFID tag to work on metal. The major requirements are that the RFID tag on metal should maintain a good reading range (>10 feet). More importantly, the solution should be low cost and have a low profile.

## 1.2 Basic antenna theory

A good understanding of how a dipole antenna radiates was necessary for solving the metal surface mounted RFID problem. The well-known Maxwell's equations for time harmonic fields in phasor form are written as,

$$\nabla \times \boldsymbol{E} = -j\omega \boldsymbol{B} \tag{1.1}$$

$$\nabla \times \boldsymbol{H} = j\omega \boldsymbol{D} + \boldsymbol{J} \tag{1.2}$$

$$\nabla \cdot \boldsymbol{D} = \rho_e \tag{1.3}$$

$$\nabla \cdot \boldsymbol{B} = 0 \tag{1.4}$$

The current continuity equation can be derived from (1.1) to (1.4),

$$\nabla \cdot \boldsymbol{J} = -j\omega \rho_e \tag{1.5}$$

From those equations, it is obvious that if the volume current density $\boldsymbol{J}$ and material properties are known, the electric field intensity $\boldsymbol{E}$ and magnetic field intensity $\boldsymbol{H}$ can be derived by solving the differential equations with the aid of constitutive relations $\boldsymbol{B} = \mu \boldsymbol{H}$ and $\boldsymbol{D} = \varepsilon \boldsymbol{E}$ [6]. An approximate approach to find the analytical solution for antenna parameters is to assume a current distribution. For an infinite small dipole antenna of length $\boldsymbol{l} \ll \lambda$, the current distribution is assumed to be a constant [5]. For a half-wavelength dipole antenna orientated towards the z direction, the current distribution is approximately written as [5],

$$\boldsymbol{I}(z') = \hat{a}_z I_0 \sin[k(l/2 - |z'|)], 0 \le |z'| \le l/2 \tag{1.6}$$

where $k$ is the wave number, $l$ is the length of the dipole antenna and equal to $\lambda/2$, $I_0$ is the maximum value of the current in z direction, and $z'$ represents the location of source current.

With the introduction of vector potential $\boldsymbol{A}$ by letting $\boldsymbol{B} = \nabla \times \boldsymbol{A}$ and applying the Lorentz gauge, equations (1.1) and (1.2) can be decoupled as,

$$\nabla^2 \boldsymbol{A} + k^2 \boldsymbol{A} = -\mu \boldsymbol{J} \tag{1.7}$$

The solution of the inhomogeneous vector Helmholtz equation in a homogeneous medium can be derived by introducing a dyadic Green's function,

$$\nabla^2 \bar{\boldsymbol{G}} + k^2 \bar{\boldsymbol{G}} = -\bar{\boldsymbol{I}}\delta(\boldsymbol{r} - \boldsymbol{r}') \tag{1.8}$$

$$\bar{\boldsymbol{G}}(\boldsymbol{r}, \boldsymbol{r}') = \bar{\boldsymbol{I}} \frac{e^{-jk|\boldsymbol{r}-\boldsymbol{r}'|}}{4\pi|\boldsymbol{r}-\boldsymbol{r}'|} \tag{1.9}$$

The unit dyadic is written as $\bar{\boldsymbol{I}} = \boldsymbol{a}_x\boldsymbol{a}_x + \boldsymbol{a}_y\boldsymbol{a}_y + \boldsymbol{a}_z\boldsymbol{a}_z$, where $\boldsymbol{a}_x$, $\boldsymbol{a}_y$ and $\boldsymbol{a}_z$ are unit vectors, $\boldsymbol{r}$ represents the position vector starting from the coordinate origin to the observation point, $\boldsymbol{r}'$ is the position vector from the coordinate origin to the source point. The solution of equation (1.7) can then be expressed using Green's function as (1.10), which is a universal formula to find the vector potential.

$$\boldsymbol{A}(\boldsymbol{r}) = \mu \iiint_V \bar{\boldsymbol{G}}(\boldsymbol{r}, \boldsymbol{r}') \cdot \boldsymbol{J}(\boldsymbol{r}') dv' \tag{1.10}$$

The electric field and magnetic field can be derived from the vector potential. For the case of a multilayer structure, by matching the boundary condition and source excitation, the dyadic Green's function should be modified. By applying the method of moments (MOM), the 3D current distribution can be finally solved [5].

A simple and explicit expression helps us gain some insight to certain problems. For an ideal dipole antenna, infinitesimally thin, line current density can be approximated as (1.6), which has a line current flowing in one direction. The vector potential is expressed as,

$$\boldsymbol{A}(\boldsymbol{r}) = \frac{\mu}{4\pi} \int_c \boldsymbol{I}_e(x', y', z') \frac{e^{-jk|\boldsymbol{r}-\boldsymbol{r}'|}}{|\boldsymbol{r}-\boldsymbol{r}'|} dl' \tag{1.11}$$

In the far field region, the integration can be done analytically for a half-wave dipole antenna with assumed sinusoidal current distribution. The components of a spherical wave can be clearly derived as,

$$E_\theta = j\eta \frac{I_0 e^{-jkr}}{2\pi r} \frac{\cos(\frac{\pi}{2}\cos\theta)}{\sin\theta} \tag{1.12}$$

$$H_\phi = j \frac{I_0 e^{-jkr}}{2\pi r} \frac{\cos(\frac{\pi}{2}\cos\theta)}{\sin\theta} \tag{1.13}$$

where $\theta$ is the angle between the antenna orientation z and space vector $\boldsymbol{r}$ and $\eta$ is the wave impedance.

The time-average radiation power density and the average power radiated by an antenna are written as,

$$\boldsymbol{W}_{rad}(x,y,z) = \frac{1}{2}\mathrm{Re}(\boldsymbol{E} \times \boldsymbol{H}^*) \tag{1.14}$$

$$P_{rad} = \oiint_s \boldsymbol{W}_{av}(x,y,z) \bullet d\boldsymbol{s} \tag{1.15}$$

Therefore, the input resistance, the radiation intensity U, beam width and directivity D can be derived analytically for this dipole antenna.

However, the hand calculation is seldom useful for an accurate estimation and can't predict the input reactance of the ideal dipole antenna. Even for the ideal infinitesimally thin dipole, a numerical analysis is necessary in order to find the reactance. For a simple one dimension case, the following Hallen's integral equation can be derived for a numerical analysis [5],

$$\int_c I_e(z') \frac{e^{-jk|\boldsymbol{r}-\boldsymbol{r}'|}}{4\pi|\boldsymbol{r}-\boldsymbol{r}'|} dz' = -j\sqrt{\frac{\varepsilon}{\mu}}[B_1 \cos(kz) + C_1 \sin(k|z|)] \tag{1.16}$$

The coefficients $B_1$ and $C_1$ can be found by applying the boundary conditions and source excitation.

A common numerical method to solve the integration equation and find the current distribution is the method of moments (MOM) [7]. First, the current can be approximated by a linear combination of N basis functions, which can be a local basis or a global basis. By choosing a weighting basis and then an operation of the inner product, the integration equation is decomposed into a series of linear equations. The coefficients of the current basis can be found by solving the linear equations. One major difficulty of the MOM is that it is difficult to find the Green's function for a complex structure. However the merit for this method is that the boundary condition is included in the Green's function; therefore it is more CPU time and memory efficient.

Since differential equations can be approximated by finite difference equations, other numerical methods to solve the differential equations such as finite difference time domain (FDTD) or finite element methods (FEM) are popular for a complex 3D structure [8]. These methods first divide the whole region into numerous small elements, for example, tetrahedral elements for 3D space, triangle elements for 2D space. For FDTD, Maxwell's equations are solved directly by satisfying the boundary and excitation conditions. For FEM, the functional is found by constructing a variational principle for the differential equation. Then in each element, the governing functional is derived. After all of the elements are assembled, a group of new equations for each element can be derived by minimizing the functional. Then the field values at each point or edge can be solved.

Some technical areas such as power engineering and digital and analog integrated circuits have relatively simple circuit models to start with. However these simple models assist people in analyzing and building very complicated systems such as a digital computer or a wireless communication system. For the antenna problem, finding the fields based on the

excitation and boundary conditions is not an easy task even for a single structure. For a real dipole antenna, the diameter of the dipole is not infinitesimally small. The current distribution is not uniform in all directions any more. Thus a hand calculation is not possible due to difficulty in accurately finding the current distribution. Due to the complexity, a simple model is not easily found to predict the performance of an antenna. Therefore, a full wave numerical electromagnetic simulation based on Maxwell's equations has to be taken in order to find a possible solution. For a more complicated problem involving irregular geometry, the simulation becomes incredibly complicated and usually can not be handled by a personal computer.

In our work, a Method of Moments (MoM) based commercial software Momentum [9] and Finite Element Method (FEM) based 3D electromagnetic simulation tool Ansoft HFSS V10 [10] were applied to analyze the antenna problem. Whenever possible, some quasistatic approximation analyses were performed to give some physical insight.

## 1.3 Summary

In this chapter, the history of RFID, various types of RFID and main challenges for the RFID industry are stated. The motivation of this work is given based on the real challenge to develop a metal-surface mounted RFID transponder. Some major numerical and analytical techniques to study antennas are discussed.

# CHAPTER 2 RFID READING RANGE

## 2.1 Introduction

When a RFID transponder with a dipole antenna is attached to a metal surface, it can not be read or written. To be able to solve the problem, we have to understand all of the factors that affect the reading/writing range.

As we'll see, the wireless communication between the RFID reader and transponder is different from the popular cellular communication. In this chapter, in order to gain a better understanding of the distinct property of RFID, a brief introduction to the wireless communication and cellular transceiver is given. The basic principle and structure of a transponder integrated circuit are explained. The internal structure and function of a state-of-the-art RFID reader are illustrated. The difference between a RFID reader and other wireless transceivers is analyzed. The radar range equation and Friis transmission equation are reexamined to facilitate a better understanding of the factors used to determine the reading range. A few available modulation methods for the RFID are discussed. The effects of different modulation schemes on the signal to noise ratio (SNR) and bit error rate (BER) are analyzed. A calculation of link-budget is conducted and the limiting factors to determine the RFID reading/writing range are discussed.

## 2.2 Basic principle of wireless communications

The people in electrical engineering (EE) deal with two major problems: generating or transmitting electrical energy and processing or communicating information [11]. A

communication system is designed to transmit and receive information in the presence of noise.

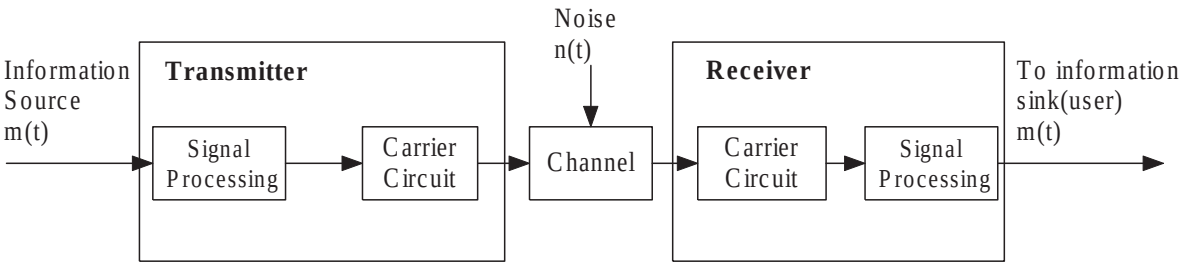


Fig. 2.1 A general communication system [11]

As shown in Fig. 2.1, the information source/sink $m(t)$ has spectrum concentrated near zero frequency generally called baseband signals. The signal processing block can be simply an analog low pass filter which is applied to narrow the bandwidth in an analog system. It can include an analog-to-digital converter (ADC) to transform the analog waveform into a digital signal, digital circuits to do the function of compression, coding/interleaving and a pulse shaping circuit to provide a tight spectrum and inter-symbol interference (ISI) free operation.

The processed baseband signal is converted into a proper frequency band by the carrier circuit. Based on the properties of the channel, a communication system is divided into two types: wired communication and wireless communication. For wireless communication, the channel might be air, free space, or seawater. In order to have the signal effectively transmitted through the medium over a certain distance, a device called a transmitting antenna has to be used to radiate the power from the transmission line medium to free space. In order to capture the transmitted power/signal, another antenna has to be placed at the front end of the receiver to transform the electromagnetic wave into conduction current in the

transmission line. Since the antenna can only radiate signal power effectively when the antenna has a dimension near an integer numbers of quarter-wavelengths [5], in order to decrease the size of the antenna, the baseband frequency spectrum is usually modulated to a higher frequency. Another reason to up convert to a higher frequency is the larger available bandwidth [12]. A wired channel includes various transmission lines and waveguides. For a wired channel, the signal frequency can also be modulated to a higher frequency. For example, in optical communication, the signal frequency is modulated onto light frequencies to enable the signal to be transmitted in the optical fiber which are even higher than the frequencies used for general wireless communication.

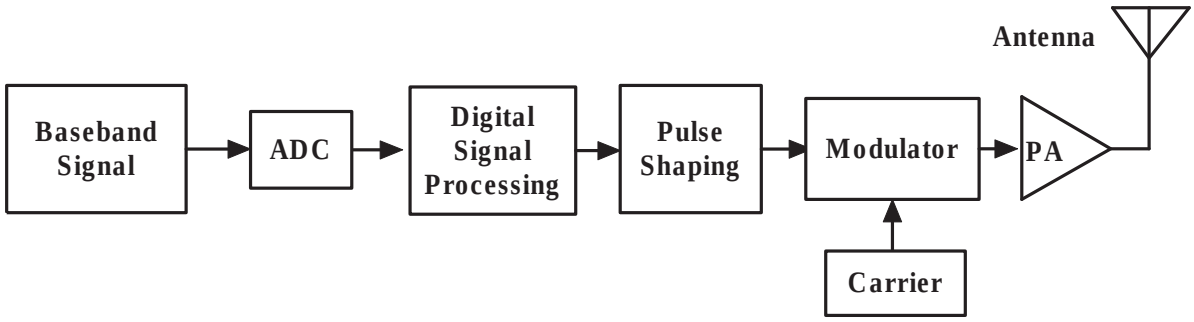


Fig. 2.2 A general wireless transmitter [13]

As shown in Fig. 2.2, after the baseband signal is processed and then modulated onto a higher carrier frequency, the modulated signal is amplified by a power amplifier to provide power to be radiated by the antenna and make long distance communication possible.

In the receiver side, the received signal with additional channel noise and interference is captured by the receiving antenna. In order to extract the very low-power signal in the presence of noise and large interference, the receiver has to be carefully planned and designed.

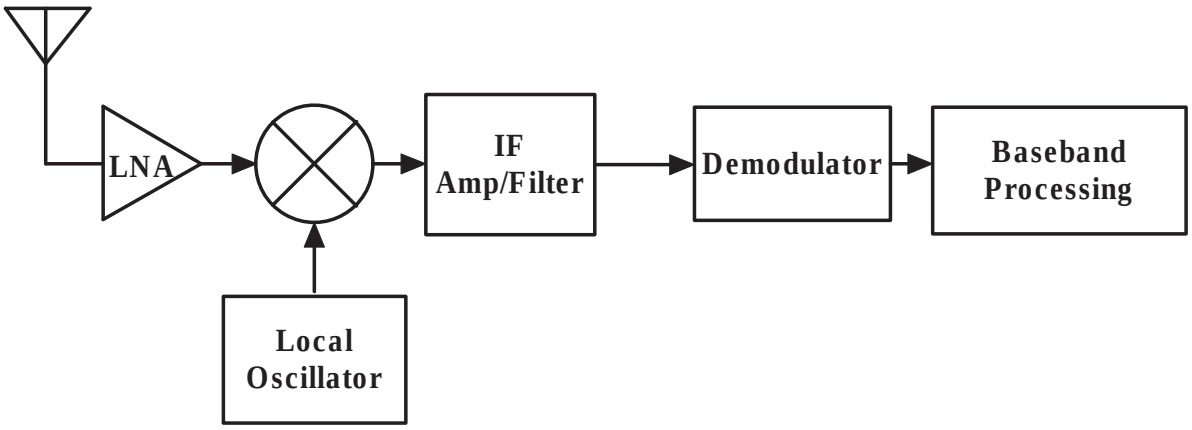


Fig.2. 3 A general wireless receiver [14]

As shown in Fig. 2.3, a low noise amplifier (LNA) with enough power gain will dominate the noise figure performance of the receiver front-end. After the signal is amplified by the LNA, the high frequency signal is then down-converted by a mixer to a lower frequency, which is called the intermediate frequency (IF). After filtering and demodulation, the signal is converted to base band frequency. The signal may be converted to digital form by an analog to digital converter (ADC). The signals are then processed in the digital world.

Depending on the methods of wireless communications, a system may be classified as simplex, half-duplex or full-duplex [12]. A simplex system allows communication only in one direction. The paging system is an example. A half-duplex system allows two-way communication. Since the same channel is used for transmission and reception, the user can only transmit or receive information at a given time. The common 2-way radio walkie-talkie is an example. By virtue of frequency division duplex (FDD) or time division duplex (TDD), a full-duplex system allows simultaneous radio transmission and reception.

## 2.3 Cellular transceiver

A cellular phone has a wireless transceiver and base band processor. GSM (global system

Table 2.1 Major parameters of GSM standards [14]

| Parameters | GSM-850 | GSM-900 | GSM-1800 (DCS-1800) | PCS-1900 |
|---|---|---|---|---|
| Transmit Band/uplink | 824-848 MHz | 890-915 MHz | 1710-1785 MHz | 1850-1910 MHz |
| Receive Band/downlink | 869-894 MHz | 935-960 MHz | 1805-1880 MHz | 1930-1990 MHz |
| Channel Spacing | 200 KHz | 200 KHz | 200 KHz | 200 KHz |
| Methods of Multiple Access | TDMA/FDM | TDMA/FDM | TDMA/FDM | TDMA/FDM |
| Duplex | FDD | FDD | FDD | FDD |
| Modulation scheme | GMSK | GMSK | GMSK | GMSK |
| Total users | 1000 | 1000 | 3000 | 2400 |
| Channel bit rate | 270.833 kb/s | 270.833 kb/s | 270.833 kb/s | 270.833 kb/s |

for mobile communications) as the second digital standard includes GSM-850 (North America), GSM-900 (Europe), GSM-1800 (DCS-1800, the United Kingdom) and PCS-1900 (North America) [14]. The detailed parameters are listed in Table 2.1.

For GSM 900, the uplink and downlink are located at 890-915 MHz and 935-960MHz, respectively. So a duplexer (two bandpass filters) is usually enough to separate signals in the

receiving frequency band from signals in the transmitting frequency band. The air interface is shown in Fig.2.4.

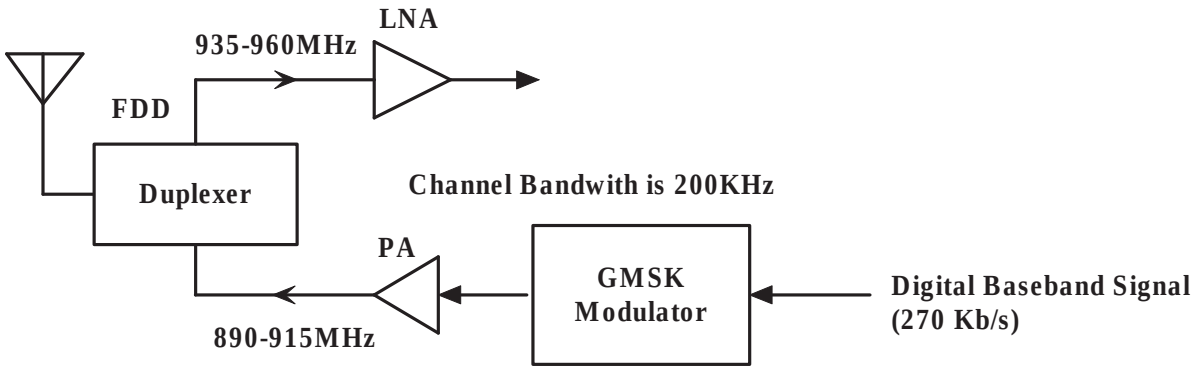


Fig. 2.4 GSM 900 air interface [13]

Gaussian Minimum Shift Keying (GMSK) modulation is obtained by first passing the baseband signal through a Gaussian filter with an impulse response $h(t) = e^{-\alpha t^2}$, which makes the shaped pulse possesses the minimum product of period and bandwidth [13]. GMSK is a spectrally efficient modulation scheme.

Since the RFID uses an ISM frequency band of 902 ~ 928 MHz in the US, the frequency band has an overlap with the GSM-900 uplink frequency band. A GSM-900 cellular phone can transmit a strong in band interferer to a RFID reader. A RFID reader can send strong in band interference signal to a base station. Since the desired signals are usually very weak when they arrive at the wireless receiver, the presence of strong in band interferers makes an accurate recognizance of useful signals even harder. For a wireless receiver, one of the biggest challenges is to pick up the tiny useful signal in the presence of strong interferers.

The magnitude and frequency of the blocker signal set the phase noise parameters of a VCO or LO. The phase noise at a certain offset frequency is determined as [14],

$$L(\Delta f)(\text{dBc/Hz}) \le P_{signal}(\text{dBm}) - P_{bloc\,ker}(\text{dB}) - SNR(\text{dB}) - 10\log(B) \quad (2.1)$$

## 2.4 RFID transponder

### 2.4.1 Basic structure and principle of RFID transponder

A RFID chip has to maintain an effective communication with the reader. It has three basic modes: power-up mode, addressing mode, and reading mode [15]. During the power-up mode, the RFID tag antenna captures the RF power from the reader. Then the RF power is rectified into DC power for the chip. When the DC voltage increases to a threshold voltage, a power on reset circuit turns the transponder into an addressing mode. During the addressing mode, the transponder decodes the incoming on-off keying (OOK) or phase shift keying (PSK) modulated signals and compares them with the ID stored in the EEPROM. If it detects its ID sent by the reader, it changes to the reading mode and starts to modulate at an intermediate (IM) frequency. The other transponders change into a quiet mode. By backscattering, the modulated electromagnetic wave is detected by the reader. Then the reader sends RF interrupts to force the transponder to communicate its next bit of information. Depending on its modulation scheme and its next bit stored in the register, the transponder will switch "ON" or "OFF" to backscatter the digits to the reader. Therefore the reader receives the data sent from the RFID transponder and demodulates it. Then the data from the transponder is compared with the ID the reader sends. If they agree with each other, then the reader exhibits the ID number on the screen.

The structure of a RFID transponder is shown in Fig. 2.5. The voltage multiplier is used to extract the RF power and convert it to a higher DC voltage. The demodulator is used to retrieve the data sent from the reader and clock information. In the Gen2 chip, an EEPROM is used to store the data information which can be rewritten remotely by the reader. In order to send the data stored in the EEPROM, a clock signal is generated by a ring oscillator and the data is retrieved and shifted by the shift register. Then the data sequence modulates the modulator to backscatter the signal through the antenna to the reader.

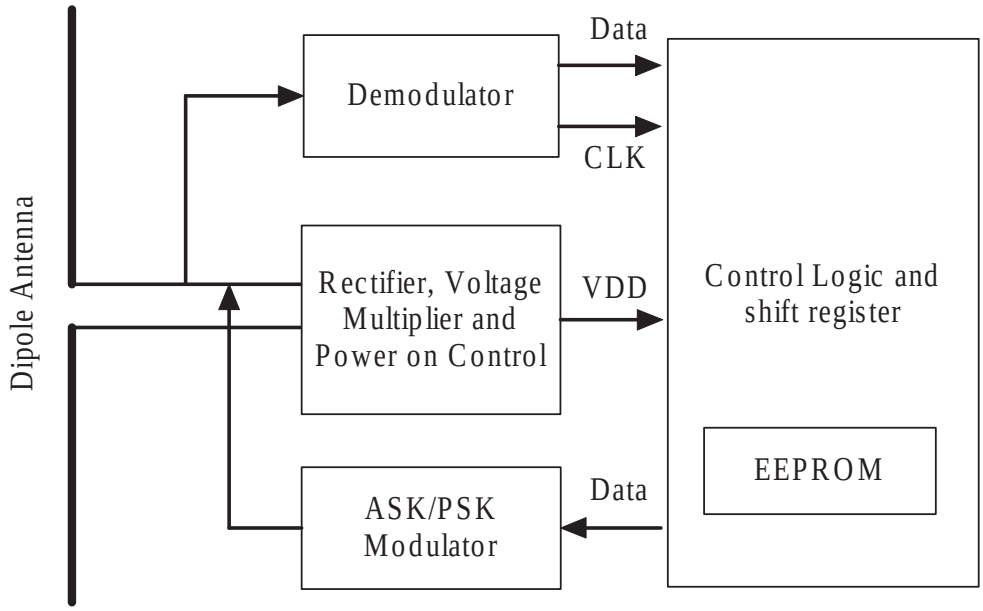


Fig. 2.5 A RFID Transponder [15]

### 2.4.2 DC power supply of a passive RFID

The passive RFID chip needs a minimum voltage to turn on the circuit. A major task is to extract the highest voltage possible from the tiny RF input power. Therefore a rectifier and a voltage multiplier are required at the front end of the chip.

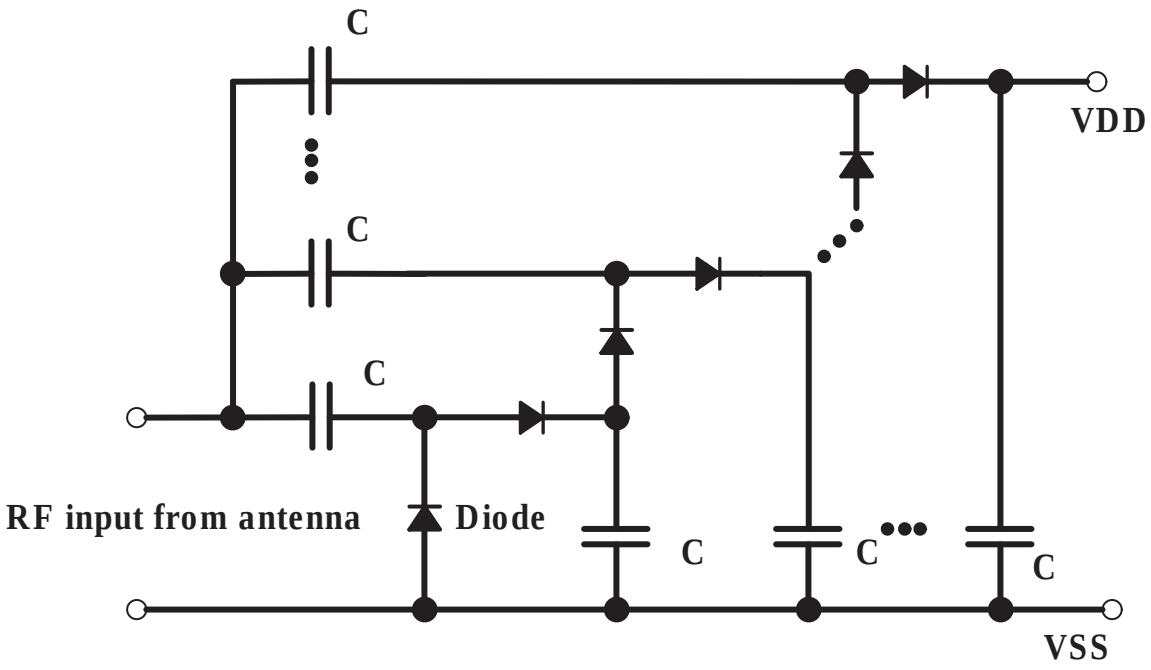


Fig. 2.6 A rectifier and voltage multiplier [15]

As shown in Fig. 2.6, $V_{out}$ is equal to $n \times (V_{RF} - V_{D0})$, $n$ is the total number of diodes, $V_{D0}$ is the forward on voltage of a schottky-barrier diode (SBD), which is formed by contacting metal onto an n-type semiconductor material. Due to the absence of a p-type semiconductor, the potential drop through the junction is approximately one half of a normal P-N junction diode. Under the conjugate matching condition, the maximum possible input power to the load is $P_{av}$. Then the source voltage (in RMS) is equal to $V_s = 2\sqrt{P_{av} R_a}$, which shows a larger antenna read impedance should increase the voltage to the RFID chip.

In a later section, it'll be demonstrated that the low overall rectifying efficiency (10%~20%) [15] becomes one major limiting factor to the passive RFID reading/writing range.

### 2.4.3 Modulation

The backscattered wave is a modulated signal which is used to distinguish the digits '0" and "1". Two major modulation schemes are used: amplitude shift keying (ASK, OOK) or phase shift keying (PSK). For an amplitude shift keying (ASK or OOK) modulation, during the on and off two states, the reflection coefficient changes its amplitude depending on the state "0" or "1". Therefore the amplitudes of the scattered power $P_{scatter}$ are different in each state. The input power for the rectifier is also different in each state. Therefore a trade off has to be made to maintain enough DC power supply and optimum backscattered power. The advantage of ASK is its simple implementation and achieving the maximum magnitude of the output DC voltage.

For a phase shift keying (PSK) modulation, the phase of the reflection coefficient changes with the modulated signal. Since the magnitude of $\Gamma_L$ doesn't change with the modulation,

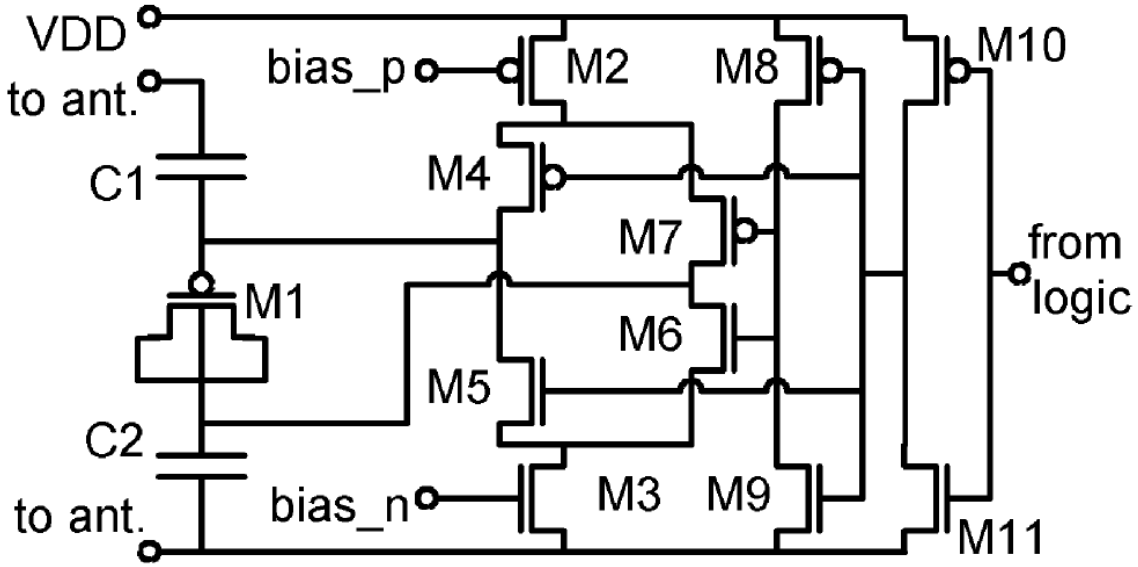


Fig. 2.7 Schematic of a PSK circuit [15]

the input power to the rectifier doesn't vary. It'll be shown in the next section that the bit error rate (BER) of the PSK is superior to the ASK. The disadvantage for PSK is its relatively complicated circuit structure. Fig. 2.7 shows a possible circuit to do the phase modulation. The varactor diode is built using a PMOS with drain and source shorted to each other. The varactor capacitance is changed by changing the DC voltage across it. The DC voltage is controlled by the input logic signal. A proper design would allow only the phase change for the reflection coefficient. However for a real circuit, due to the parasitic parameters, a pure ASK or PSK won't exist, instead, a hybrid mode exists which raises the complexity of the analysis.

### 2.4.4 Signal to noise ratio and bit error rate of ASK and PSK

If the RFID transponder uses ASK or PSK modulation, the modulated signal is equal to the product of the carrier and the base band signal. For digital communication, the base band signal is a square wave rather than a sine wave as in analog communication. If we assume the carrier signal is a sine wave, then the backscattered signal is a switched sine wave. The following analysis shows the spectrum of the switched sine wave.

Assuming a rectangular pulse has the following function,

$$X_b(t) = \begin{cases} 1, t \in \left[ -\frac{T_b}{2}, \frac{T_b}{2} \right] \\ 0, otherwise \end{cases} \tag{2.2}$$

The Fourier transform of $X_b(t)$ is

$$X_b(j\omega) = \int_{-\infty}^{\infty} X_b(t) e^{-j\omega t} dt = 2\frac{\sin(\frac{\omega T_b}{2})}{\omega} = T_b \frac{\sin(\frac{\omega T_b}{2})}{\frac{\omega T_b}{2}} = T_b \sin c(\frac{\omega T_b}{2}) \tag{2.3}$$

If the RFID uses ASK, the backscattered signal $X_m(t)$ is equal to the product of a rectangular pulse $X_b(t)$ and carrier $X_c(t)$ in the time domain,

$$X_m(t) = X_c(t)X_b(t) \tag{2.4}$$

A sinusoidal carrier signal $X_c(t) = A\cos(\omega_c t)$ with zero initial phase has a Fourier transform,

$$X_c(j\omega) = \pi A\left[\delta(\omega-\omega_c)+\delta(\omega+\omega_c)\right] \tag{2.5}$$

In the frequency domain, the spectrum of the signal product is derived based on the convolution properties of a Fourier transform,

$$\begin{aligned} X_m(j\omega) &= X_c(j\omega) * X_b(j\omega) = \frac{1}{2\pi}\int_{-\infty}^{\infty} X_c(j\theta)X_b(j(\omega-\theta))d\theta \\ &= \frac{1}{2\pi}\int_{-\infty}^{\infty} \pi A\left[\delta(\theta-\omega_c)+\delta(\theta+\omega_c)\right]T_b \sin c(\frac{(\omega-\theta)T_b}{2})d\theta \\ &= \frac{AT_b}{2}\left[\sin c(\frac{(\omega-\omega_c)T_b}{2})+\sin c(\frac{(\omega+\omega_c)T_b}{2})\right] \end{aligned} \tag{2.6}$$

Therefore the backscattered spectrum can be expressed as a sinc function, which is continuous and centered at the carrier frequency.

For coherent detection, with a matched-filter reception, with the existence of Gaussian channel noise, it can be shown that the ASK and FSK has a probability of bit error [11],

$$P_e = Q(\sqrt{\frac{E_b}{N_0}}) \tag{2.7}$$

where $E_b$ is the signal power and $N_0$ is the noise power.

For PSK, a probability of bit error is given as,

$$P_e = Q(\sqrt{\frac{2E_b}{N_0}}) \tag{2.8}$$

where $$Q(x) = \frac{1}{\sqrt{2\pi}} \int_x^{\infty} e^{(-\frac{u^2}{2})} du \qquad (2.9)$$

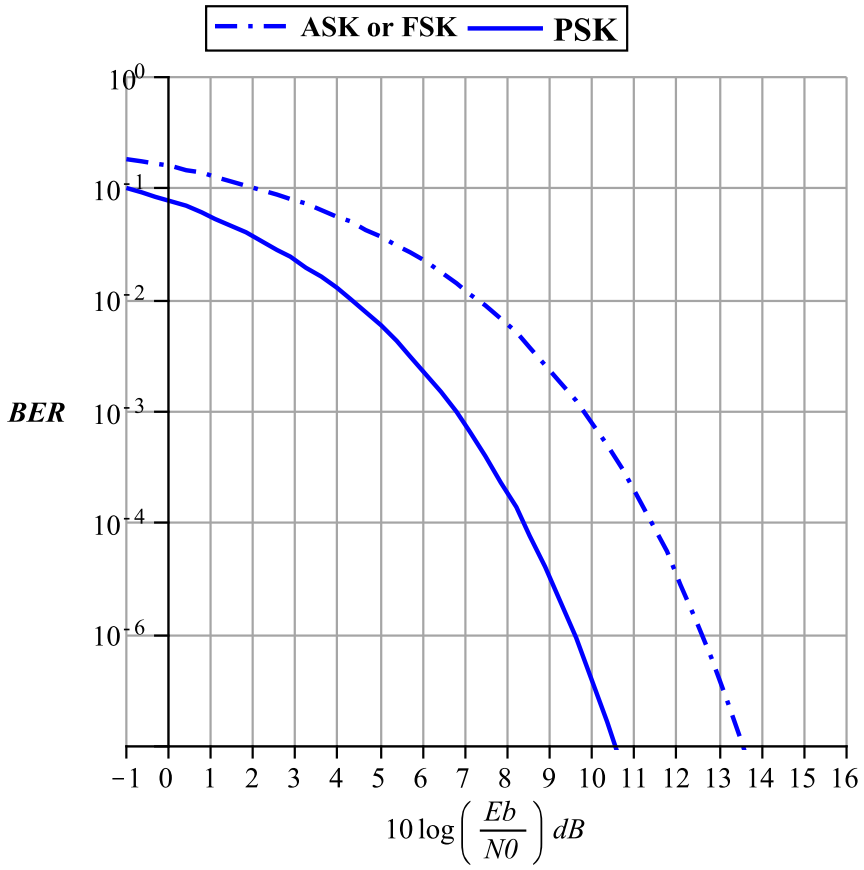


Fig. 2.8 Comparison of the probability of bit error for a coherent ASK/FSK and PSK

As shown in Fig. 2.8, for the same bit error rate (BER), PSK has a 3 dB SNR advantage over ASK/FSK. However, ASK is much easier to be implemented in a RFID transponder. For a BER of 1E-4, the SNR for the ASK is about 11.5 dB. This sets the minimum SNR requirement for the receiver.

## 2.5 RFID reader

The RFID communication is different from cellular communication since the RFID uses the backscattering communication technique [1]. A RFID reader sends the signal and power through an antenna to a RFID transponder. After the RFID transponder is powered up, it is going to modulate the radar cross section of the RFID transponder antenna so that the backscattered electromagnetic energy has different magnitude (ASK) or phase (PSK). It can be seen that for a RFID reader, the received signal and transmitted signal have the same carrier frequency. This is the major difference from the cellular phone or other wireless applications. For other wireless transceivers, transmitting and receiving either use different frequencies (frequency division duplex or FDD) or operate at different time slots (time division duplex or TDD). Therefore, there is a good isolation between transmitting signals and receiving signals.

RFID includes a near field reader and far field reader. A far field reader can be divided into a handheld reader and a port station. The handheld reader we used has an isotropic radiated power (EIRP) $P_{EIRP}$ of 4W. The equivalent radiated power (ERP) $P_{ERP}$ equals to the $P_{EIRP}$ divided by the gain of the antenna. For a half-wavelength dipole antenna with gain 1.643, $P_{ERP}$ equals to 2.435W.

A RFID reader is a transceiver working in the RF frequency range. In order to generate 33.87 dBm (2.435W) input power for the reader antenna, it needs a RF oscillator and power amplifier modules. It requires a circuit unit to do the digital modulation and demodulation. A mixer is used to lower the received RF frequency to an intermediate frequency (IF). A circulator is used to separate the input and output RF signal connecting to the antenna. Fig.

2.9 shows a simplified diagram of a RFID reader [16] which uses one antenna for transmitting and receiving RF signals.

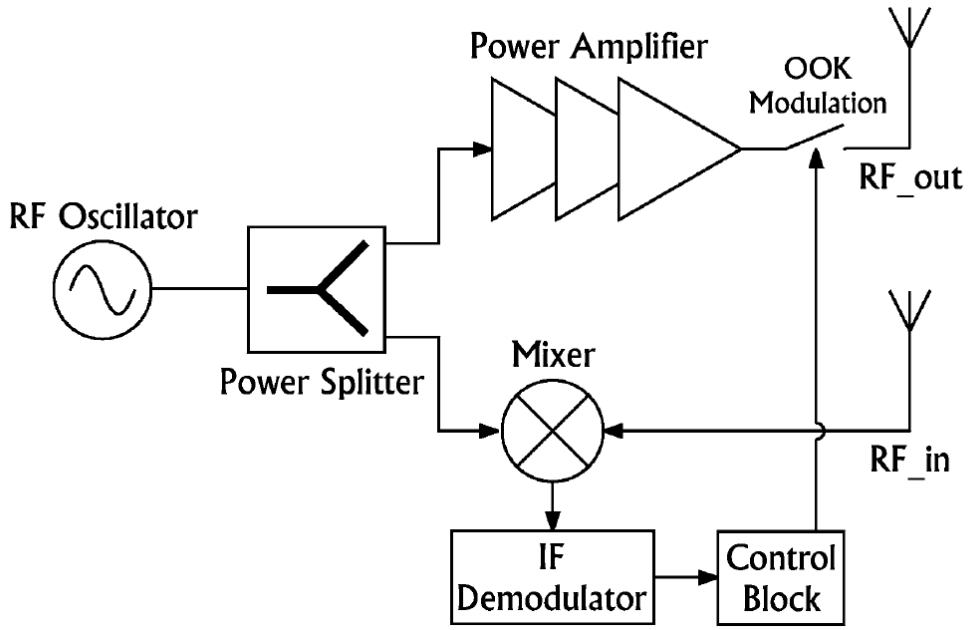


Fig. 2.9 A RFID reader [16]

A RFID reader includes two major types: stationary reader and mobile reader. A stationary reader has a different TX antenna and RX antenna. It receives electromagnetic waves backscattered from a RFID transponder via the RX antenna. The TX antenna and RX antenna can be placed at different locations. The physical distance usually guarantees a good isolation between the TX antenna and the RX antenna. A mobile or hand-held-type reader shares one antenna for both the TX and the RX path because of limited space. Unfortunately, since the passive RFID communication is using a back-scattered response, which means a reader transmits and receives signals at the same time and at the same carrier frequency, TDD or

FDD is not applicable to RFID communication. Therefore a directional coupler or a circulator instead of a duplexer or switch has to be used in a hand-held-type reader. However, either the directional coupler or circulator can't completely separate transmission from reception. Some of the TX power will leak into the receiver.

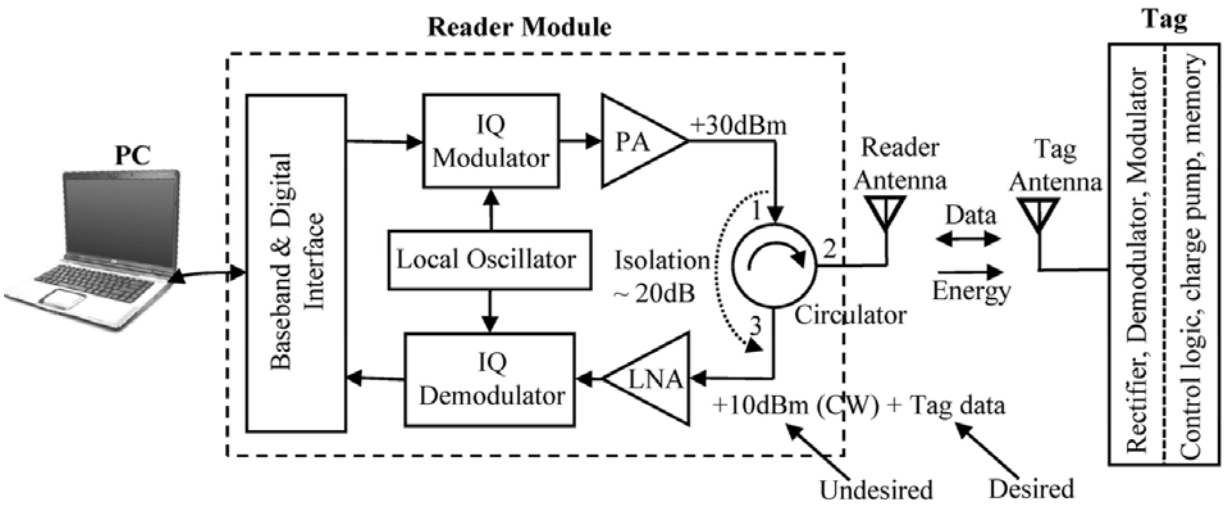


Fig. 2.10 A RFID communication system [17]

Fig. 2.10 shows a RFID communication system [17]. The internal circuit block of the RFID reader is shown in Fig. 2.11. I-channel and Q-channel baseband signals are first processed by a digital to analog converter (DAC), then processed by a pulse shaping filter (PSF). After that, the I/Q signals are modulated by an I-Q modulator and converted to the carrier frequency (902MHz ~ 928 MHz). The signal is amplified by a power amplifier and transmitted through the circulator and antenna. The transmitted energy is captured by the transponder antenna and then rectified to a DC voltage. Once the transponder is powered up, it demodulates the captured data sequence. It then sends the stored digital data to the reader by modulating the antenna radar cross section. The backscattered signals are accepted by the RFID reader

antenna and amplified by a LNA. I-Q mixers will convert the input signals to baseband frequency. Then the signals are amplified and selected by a channel select filter (CSF). A variable gain amplifier (VGA) is essential to keep a large dynamic range for the receiver. After the I/Q demodulator, the digital data from the RFID transponder are acquired. ADCs are applied when further digital processing is necessary. The I-Q LO signals are generated by a dual loop phase-locked loop (DLPLL). A PLL tracks the phase or frequency of the input signals.

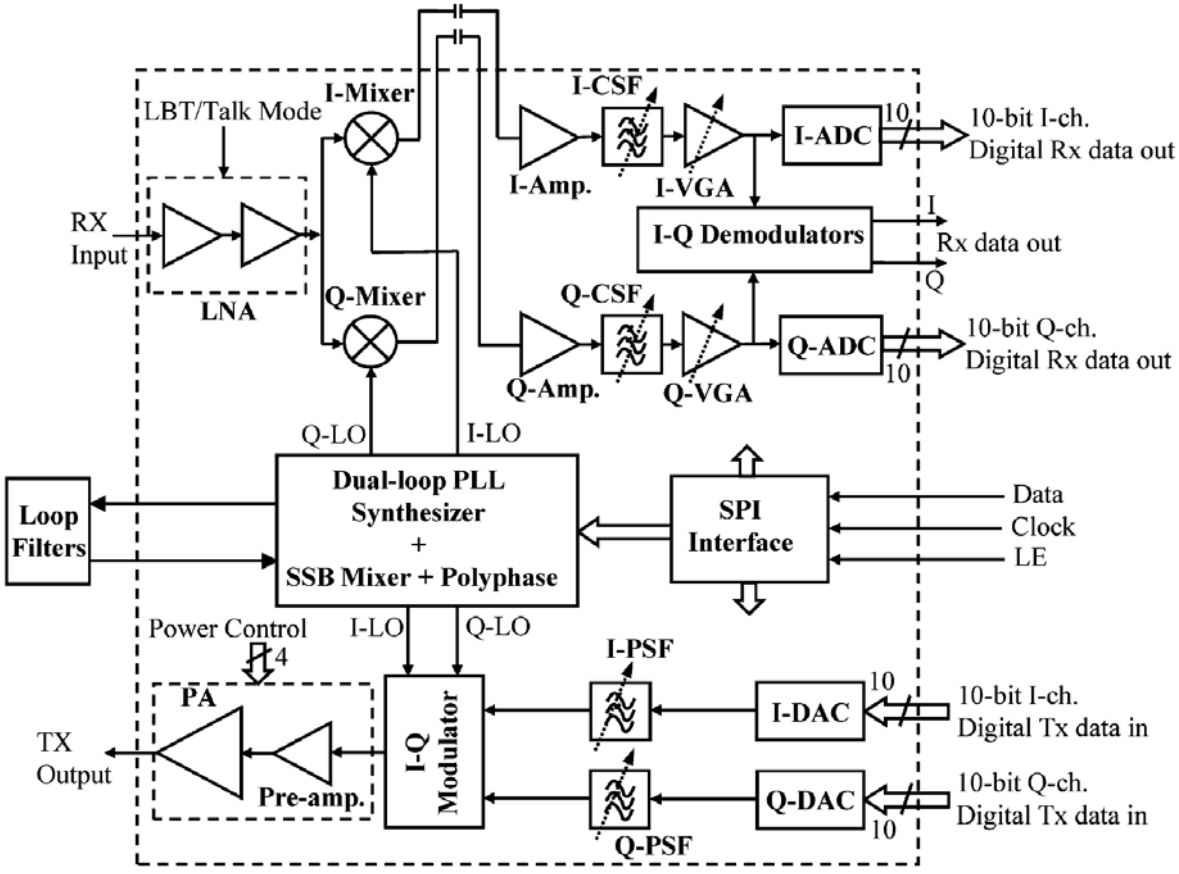


Fig. 2.11 A RFID reader integrated circuit architecture [17]

The Symbol MC9000-G RFID reader [18] supports EPC Gen 1 (Class 0 & Class 1) and Gen 2 standards. It works for a frequency range from 902MHz~ 928 MHz. The output power is 1 W (4W EIRP) with an antenna gain of 4 (6 dBi antenna gain). This was the handheld RFID reader we used for this work.

## 2.6 Radar cross section (RCS) and backscattering radiation

Since the RFID transponder uses backscattering to send the data to the reader, the radar cross section of the receiving antenna at different loads is a figure of merit in determining the communication quality.

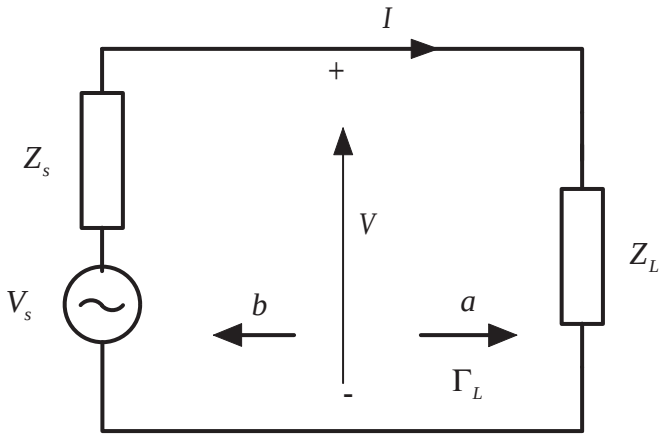


Fig. 2.12 Equivalent circuit for the RFID transponder antenna

A simplified analysis based on the antenna equivalent circuit in Fig. 2.12 is followed. $V$ and $I$ are the maximum values. Antenna input impedance $Z_s$ equals to $R_s + jX_s$. The antenna load impedance $Z_L$ equals to $R_L + jX_L$. $R_s$ is the sum of the antenna equivalent loss resistance $R_c$ and radiation resistance $R_r$.

The power waves $a$ and $b$ are defined as [19],

$$a = \frac{V + Z_s I}{2\sqrt{R_s}} \tag{2.10}$$

$$b = \frac{V - Z_s^* I}{2\sqrt{R_s}} \tag{2.11}$$

where $Z_s^*$ is the conjugate impedance of $Z_s$.

The voltage $V$ and current $I$ can be solved from (2.10) and (2.11),

$$V = \frac{Z_s^* a + Z_s b}{\sqrt{R_s}} \tag{2.12}$$

$$I = \frac{1}{\sqrt{R_s}}(a - b) \tag{2.13}$$

Then the load reflection coefficient can be derived as,

$$\Gamma_L = \frac{b}{a} = \frac{V - Z_s^* I}{V + Z_s I} = \frac{Z_L - Z_s^*}{Z_L + Z_s} \tag{2.14}$$

The power consumed by the load is equal to available input power minus reflected power, which is derived as,

$$P_L = \frac{1}{2}|a|^2(1 - |\Gamma_L|^2) = \frac{1}{2}|a|^2\left[1 - \frac{(R_L - R_s)^2 + (X_L + X_s)^2}{(R_L + R_s)^2 + (X_L + X_s)^2}\right] = |a|^2 \frac{2R_L R_s}{|Z_L + Z_s|^2} \tag{2.15}$$

The scattered power by the antenna is derived as,

$$P_{scatter} = \frac{1}{2}|I|^2 R_r = \frac{1}{2}\left|\frac{1}{\sqrt{R_s}}(a - b)\right|^2 R_r = \frac{R_r}{2R_s}|a|^2 |1 - \Gamma_L|^2 = |a|^2 \frac{2R_r R_s}{|Z_L + Z_s|^2} \tag{2.16}$$

The power consumption due to the loss resistance is derived as,

$$P_{loss} = \frac{1}{2}|I|^2 R_c = \frac{1}{2}\left|\frac{1}{\sqrt{R_s}}(a - b)\right|^2 R_c = \frac{R_c}{2R_s}|a|^2 |1 - \Gamma_L|^2 = |a|^2 \frac{2R_c R_s}{|Z_L + Z_s|^2} \tag{2.17}$$

The antenna radiation efficiency is defined as [5],

$$\varepsilon_{cd} = \frac{R_r}{R_r + R_c} = \frac{R_r}{R_s} \tag{2.18}$$

Under conjugate matching condition, $P_{scatter} + P_{loss} = P_L$, in order to capture 50% power for the RFID chip, 50% power has to be reradiated or consumed by the antenna itself. So the scattered power can be expressed as,

$$P_{scatter} = \varepsilon_{cd} P_L \tag{2.19}$$

Under the conjugate matching condition, the available power can be easily derived as,

$$P_{av} = \frac{1}{2}|a|^2 = \frac{1}{2}\left|\frac{V + Z_s I}{2\sqrt{R_s}}\right|^2 = \frac{1}{2}\left|\frac{V_s - Z_s I + Z_s I}{2\sqrt{R_s}}\right|^2 = \frac{V_s^2}{8R_s} = A_{em} W_i = \frac{\lambda^2}{4\pi} G_r W_i \tag{2.20}$$

Then $|a|^2$ can be derived as,

$$|a|^2 = 2 A_{em} W_i \tag{2.21}$$

$A_{em}$ is the maximum effective area, $W_i$ is the input power density, $G_r$ is the gain of the receiving antenna. Combining (2.16) and (2.21), the scattered power is written as the product of the radar cross section and input power density,

$$P_{scattered} = \sigma W_i = A_{em} W_i \frac{4R_s R_r}{|Z_L + Z_s|^2} \tag{2.22}$$

The radar cross section of the antenna can be then expressed as a function of the antenna gain, antenna impedance, load impedance and wavelength,

$$\sigma = \frac{\lambda^2 G_r}{4\pi} \frac{4R_s R_r}{|Z_s + Z_L|^2} = \frac{\lambda^2 G_r}{4\pi} \frac{4R_s^2 \varepsilon_{cd}}{|Z_s + Z_L|^2} = \frac{\lambda^2 D_r}{\pi} \frac{\varepsilon_{cd}^2 R_s^2}{|Z_s + Z_L|^2} \tag{2.23}$$

The radar cross section at the conjugate matching condition has a maximum value, which is equal to the maximum effective area with 100% efficiency. Under any other conditions, since $Z_s = R_s + jX_s$ is a complex number, and $R_s \ll X_s$ for RFID transponders, even with a shorted load, the radar cross section would be much less than $A_{em}$.

Since the transmitter and receiver are at the same location, the radar cross section is called a monostatic or backscattering RCS, otherwise, it is called a bistatic RCS.

If the reflection coefficient and input power at the interface between the RFID reader antenna and RFID reader generator are expressed as $\Gamma_t$ and $P_{in}$, respectively, with an antenna gain $G_t$, the radiated power density at a distance R to the RFID reader is,

$$W_t = \frac{P_{in} G_t}{4\pi R^2}(1 - |\Gamma_t|^2) \tag{2.24}$$

After the power is captured by the RFID transponder antenna, it'll be backscattered to the RFID reader. Therefore the scattered power density can be written as,

$$W_s = \frac{\sigma W_t}{4\pi R^2} \tag{2.25}$$

The amount of power delivered to the RFID reader is,

$$\begin{aligned} P_r &= A_r W_s = \frac{\lambda^2 G_t}{4\pi}(1 - |\Gamma_t|^2) W_s \left|\hat{\rho}_s \bullet \hat{\rho}_r\right|^2 = \frac{\lambda^2 G_t}{4\pi}(1 - |\Gamma_t|^2)\frac{\sigma W_t}{4\pi R^2}\left|\hat{\rho}_s \bullet \hat{\rho}_r\right|^2 \\ &= \frac{\lambda^2 G_t}{4\pi}(1 - |\Gamma_t|^2)\frac{\sigma}{4\pi R^2}\frac{P_{in} G_t}{4\pi R^2}(1 - |\Gamma_t|^2)\left|\hat{\rho}_s \bullet \hat{\rho}_r\right|^2 = \sigma \frac{P_{in}\lambda^2 G_t^2}{(4\pi)^3 R^4}(1 - |\Gamma_t|^2)^2 \left|\hat{\rho}_s \bullet \hat{\rho}_r\right|^2 \end{aligned} \tag{2.26}$$

The term $\left|\hat{\rho}_s \bullet \hat{\rho}_r\right|^2$ accounts for the polarization loss between the scattered waves and receiving antennas. Based on the above formulation, in order to more accurately describe

the RCS of an antenna, a more strict procedure should be followed. The scattered electrical field can be written as [5],

$$\boldsymbol{E}^s(Z_L) = \boldsymbol{E}^s(Z_A) - \Gamma_A \boldsymbol{E}_t \frac{I_m}{I_t} \tag{2.27}$$

where $\boldsymbol{E}^s(Z_A)$, $\Gamma_A$ and $I_m$ are the scattered electric field, reflection coefficient and scattering current when the load impedance is $Z_A$ and $I_t$ and $\boldsymbol{E}_t$ are the antenna current and electric field radiated by the antenna in the transmitting mode, respectively.

Since the electromagnetic waves radiated by an antenna in the far field region ($r > 2D^2/\lambda$) are approximately a plane wave, and the S parameters are derived based on the assumption of plane wave, the S matrix shown in Fig. 2.13 can be applied to describe the behavior of the reader-transponder antenna link.

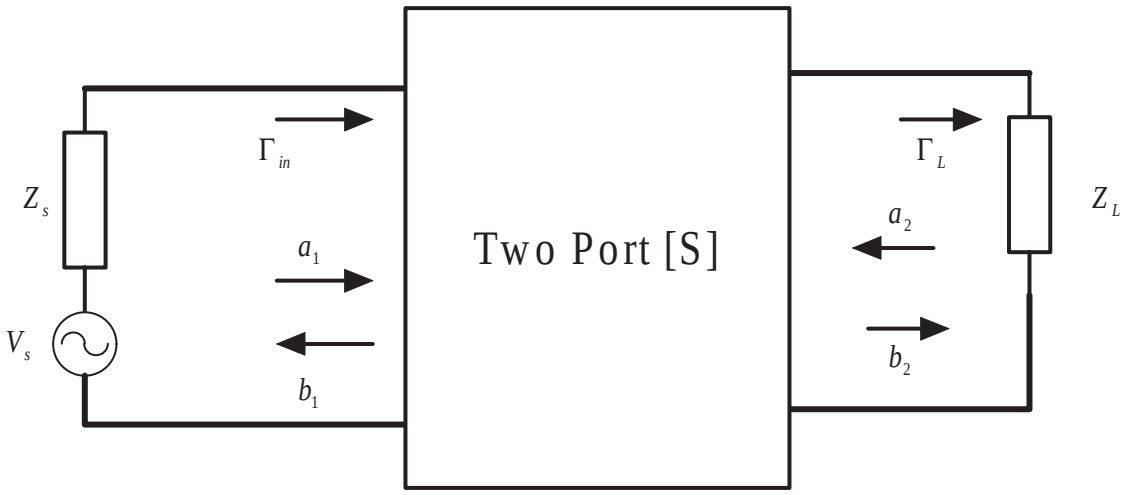


Fig. 2.13 Equivalent scattering matrix description for the link of the RFID reader and transponder

The scattering matrix of the two ports is written as [20],

$$b_1 = S_{11}a_1 + S_{12}a_2 \tag{2.28}$$

$$b_2 = S_{21}a_1 + S_{22}a_2 \tag{2.29}$$

The load reflection coefficient $\Gamma_L$ is expressed as,

$$\Gamma_L = \frac{a_2}{b_2} \tag{2.30}$$

From (2.28) and (2.30), the reflection coefficient $\Gamma_{in}$ at the input port can be derived as,

$$\Gamma_{in} = \frac{b_1}{a_1} = \frac{S_{11}a_1 + S_{12}a_2}{a_1} = S_{11} + S_{12}\frac{a_2}{a_1} = S_{11} + S_{12}\frac{\Gamma_L b_2}{a_1} \tag{2.31}$$

Combining (2.29) and (2.30), $b_2 = S_{21}a_1 + S_{22}a_2 = S_{21}a_1 + S_{22}\Gamma_L b_2$, therefore,

$$b_2 = \frac{S_{21}a_1}{1 - S_{22}\Gamma_L} \tag{2.32}$$

From (2.31) and (2.32), the input reflection coefficient is clearly related to the load reflection coefficient by the following equation [20],

$$\Gamma_{in} = S_{11} + \frac{S_{12}S_{21}\Gamma_L}{1 - S_{22}\Gamma_L} \tag{2.33}$$

Since $\Gamma_{in}$ can be measured with a network analyzer, if $S_{11}, S_{12}S_{21}, S_{22}$ are treated as three complex variables, by varying the load impedance or equivalently $\Gamma_L$ to three known complex numbers, in principle, by three measurements, the scattering parameters can be determined.

During the period of reader-transponder downlink communication, the received power scattered by the RFID antenna $P_{r\_scattered}$ can be written as,

$$P_{r\_scattered} = P_{in}(|\Gamma_{in}|^2 - |\Gamma_t|^2) \tag{2.34}$$

$P_{r\_scattered}$ derived by (2.34) should be the same as the received power derived by the Radar Range Equation (2.26). So the RCS can be derived as,

$$\sigma = (|\Gamma_{in}|^2 - |\Gamma_t|^2)\frac{(4\pi)^3 R^4}{\lambda^2 G_t^2}\frac{1}{(1-|\Gamma_t|^2)^2\left|\hat{\rho}_s \bullet \hat{\rho}_r\right|^2} \tag{2.35}$$

With a conjugate matching at the input port between transmitting antenna and generator and with zero polarization loss, the above formula for a RCS of the RFID transponder can be simplified as,

$$\sigma = |\Gamma_{in}|^2 \frac{(4\pi)^3 R^4}{\lambda^2 G_t^2} \tag{2.36}$$

Therefore the RCS can be measured more accurately. With a matched load, $\Gamma_{in} \approx S_{11}$. Only a one port S parameter is needed to measure the RCS with a matched load. The approach by using a full two-port S matrix is theoretically stricter for any load impedance.

From (2.26), the maximum distance for a receiver which is able to pick up a signal with a signal level $P_r$ with an acceptable signal to noise ratio (SNR) or bit error rate (BER) at a given input power $P_{in}$ is,

$$R = \sqrt[4]{\sigma\frac{P_{in}\lambda^2 G_t^2}{P_r(4\pi)^3}(1-|\Gamma_t|^2)^2\left|\hat{\rho}_s \bullet \hat{\rho}_r\right|^2} = \sqrt[4]{\sigma\frac{P_{in}c^2 G_t^2}{P_r(4\pi)^3 f^2}(1-|\Gamma_t|^2)^2\left|\hat{\rho}_s \bullet \hat{\rho}_r\right|^2} \tag{2.37}$$

where $c$ is the speed of light in free space and $f$ is the fundamental signal frequency.

## 2.7 The factors to determine the reading/writing range

As we mentioned before, for a backscattering communication system, the transmission signals and receive signals have the same carrier frequency and the transmitting and

receiving process happens almost simultaneously due to the short distance, therefore frequency division duplex (FDD) or time division duplex (TDD) can't be applied to the transceiver front-end. This is one distinct difference from the other wireless communication like mobile phone service or GPS (Global Positioning System).

### 2.7.1 Directional coupler (circulator)

To separate the transmitting signals and receiving signals, some other methods like a directional coupler should be applied. The common circulator is a passive microwave device which usually has three ports. It can be built with a stripline connector, ferrite disk and bias magnet [21]. The scattering matrix description for a three port device is given as,

$$[S]=\begin{bmatrix} S_{11} & S_{12} & S_{13} \\ S_{21} & S_{22} & S_{23} \\ S_{31} & S_{32} & S_{33} \end{bmatrix} \tag{2.38}$$

If all of the ports are matched, then $S_{11}$, $S_{22}$ and $S_{33}$ should be each equal to zero. If the 3-port network is lossless, than based on energy conservation, the S matrix should be unitary, which means the following condition should be met [21],

$$[S]^T[S]^* = [I] \text{ or } \sum_{k=1}^{N} S_{ki}S_{kj}^* = \delta_{ij}, i, j = 1...N \tag{2.39}$$

It can be easily shown that for the matched reciprocal matrix, it can't be unitary, which means that a three-port lossless reciprocal network that is matched at all ports doesn't exist. Since the properties of matching and loss are more important for maximum power transfer, a practical ferrite circulator is built with those properties but it is nonreciprocal. The S matrix of an ideal circulator is expressed as [21],

$$[S]=\begin{bmatrix}0 & 0 & 1\\ 1 & 0 & 0\\ 0 & 1 & 0\end{bmatrix} \tag{2.40}$$

From the matrix description, the RF power is able to transfer from port 1 to port 2, port 2 to port 3 and port 3 to port 1. Due to the symmetry, any port can be defined as port 1. Once port 1 is chosen, based on the structure of the circulator, port 2 and 3 are fixed. If port 1 is chosen as the transmitting port, port 2 and 3 should be the antenna port and receiving port, respectively. The ferrite circulator usually has a minimum 20 dB isolation from the input port to the isolated port. We'll show that the finite isolation of the circulator exerts a high linearity requirement for the receiver.

### 2.7.2 Noise figure, sensitivity, IIP3 and dynamic range

Noise figure is defined as the input signal-to-noise ratio (SNR) to the output signal-to-noise ratio. For a cascaded system, the overall noise figure is expressed as [20],

$$NF_{total}=1+NF_1-1+\frac{NF_2-1}{G_{a1}}+\frac{NF_3-1}{G_{a1}G_{a2}}+\ldots \tag{2.41}$$

where $NF_1$, $NF_2$ and $NF_3$ are the numeric noise figures of stage 1, 2 and 3, respectively. $G_{a1}$ and $G_{a2}$ are the numeric available power gains for stage 1 and 2, respectively. $NF_{total}$ represents the overall numeric noise figure of the receiver.

For a receiver, the first amplification stage usually dominates the overall noise performance. Therefore a LNA with a low noise figure but enough power gain is placed as the first amplifier to amplify the received signal without introducing much additional noise.

The sensitivity of a RF receiver determines the lower bound of the magnitude of the

received signal, which is defined as the minimum input signal level for a given SNR or BER. Mathematically, it is expressed as [13],

$$P_{in,\min} = -174\text{dBm/Hz} + NF + 10\log B + SNR_{\min} \tag{2.42}$$

where $P_{in,\min}$ is the minimum allowed input signal power, $-174$dBm/Hz accounts for the available thermal noise power in a unit bandwidth, $NF$ is the overall noise figure of the receiver, $B$ is the bandwidth in Hertz and $SNR_{\min}$ is the minimum SNR requirement for a given BER.

For a given nonlinear system, when two input signals with different frequencies are fed to the system, the system will generate frequencies which are different from the harmonics of the two input frequencies, the phenomenon is called intermodulation (IM). In dBm units, for a two-tone test, the input third interception point (IIP3) is expressed as [13],

$$IIP3\big|\text{dBm} = P_{in,\omega 1} + \frac{1}{2}(P_{out,\omega 1} - P_{out,IM3}) \tag{2.43}$$

where $IIP3\big|$dBm represents the IIP3 in a unit of dBm, $P_{in,\omega 1}$ is the input signal power at frequency $\omega_1$, $P_{out,\omega 1}$ is the output signal power at $\omega_1$, and $P_{out,IM3}$ is the output IM3 power, all in units of dBm.

In cascaded stages, the overall IIP3 is express as [13],

$$\frac{1}{A_{IP3,t}^2} \approx \frac{1}{A_{IP3,1}^2} + \frac{A_{v1}^2}{A_{IP3,2}^2} + \frac{A_{v1}^2 A_{v2}^2}{A_{IP3,3}^2} + \ldots \tag{2.44}$$

where $A_{IP3,1}$, $A_{IP3,2}$ and $A_{IP3,3}$ are the IIP3's of the first stage, second stage and third stage, respectively. $A_{v1}$ and $A_{v2}$ are the voltage gains of the first stage and second stage, respectively. $A_{IP3,t}$ represents the overall IIP3 of the cascaded system.

The upper bound of the received signal level is determined by the nonlinearity of the system, which is defined as the maximum input signal level in a two-tone test for which the input IM3 is equal to the noise floor [13],

$$P_{in,\max} = \frac{2P_{IIP3} + F}{3}, F = -174\text{dBm/Hz} + NF + 10\log B \tag{2.45}$$

The spurious free dynamic range (SFDR) is the difference between the maximum allowed input-signal and minimum detectable input-signal [13],

$$SFDR = \frac{2P_{IIP3} + F}{3} - (F + SNR_{\min}) = \frac{2(P_{IIP3} - F)}{3} - SNR_{\min} \tag{2.46}$$

A receiver should have a low NF in order to keep the sensitivity of the system at the desired low level. The linearity, such as IIP3, should be good so that the receiver is able to recognize useful signals even in the presence of the strong in-band interference.

### 2.7.3 1-dB compression point and IIP3 of a RFID reader

Assuming the receiver has an input-output relationship $y(t) = f(x(t))$, a Taylor's series expansion gives,

$$y(t) = f(x(t)) = f(x_0) + f'(x_0)(x - x_0) + \frac{f''(x_0)}{2!}(x - x_0)^2 + \ldots \tag{2.47}$$

As a weakly nonlinear system, the higher order term is smaller. Therefore the receiver input-output relationship can be approximately described as the following polynomials,

$$y(t) = \alpha_0 + \alpha_1 x(t) + \alpha_2 x^2(t) + \alpha_3 x^3(t) \tag{2.48}$$

The strong interferer from the transmitter at the carrier frequency can be expressed as,

$$X_I(t) = A_I \cos(\omega_c t) \tag{2.49}$$

When the RFID transponder modulates the scattered wave at a frequency $\omega_b$ , the backscattered signal in time domain can be approximately written as,

$$X_s(t) = A_s\left[\cos(\omega_c - \omega_b)t + \cos(\omega_c + \omega_b)t\right] \tag{2.50}$$

The total input signals to the receiver is the sum of the interferer and backscattered signal,

$$x(t) = X_I(t) + X_s(t)\,, \tag{2.51}$$

The higher order polynomials will cause inter-modulation terms which are equal to the useful frequencies $\omega_c - \omega_b$ and $\omega_c + \omega_b$ . The term at $\omega_c \pm \omega_b$ including the IM term can be easily derived as [13],

$$\omega_c \pm \omega_b : \alpha_1 A_s + \frac{9}{4}\alpha_3 A_s^3 + \frac{9}{4}\alpha_3 A_I^2 A_s \tag{2.52}$$

For a relatively small input due to backscattering, the $\frac{9}{4}\alpha_3 A_s^3$ term can be neglected. When the $\omega_c \pm \omega_b$ terms are equal to zero, the useful base band information will be lost after down conversation. When $\alpha_1 A_s + \frac{9}{4}\alpha_3 A_I^2 A_s = 0$ , $A_I$ is,

$$A_I = \frac{2}{3}\sqrt{\left|\frac{\alpha_1}{\alpha_3}\right|} \tag{2.53}$$

It is common that $\alpha_3 < 0$ for a stable receiver system.

The input third interception point can be derived as [13],

$$A_{IIP3} = \sqrt{\frac{4}{3}\left|\frac{\alpha_1}{\alpha_3}\right|} \tag{2.54}$$

Therefore,

$$A_{IIP3} = \sqrt{3}A_I \tag{2.55}$$

Expressed in dBm,

$$A_{IIP3}\left|\text{dBm} = (A_I + 4.77)\right|\text{dBm} \tag{2.56}$$

The 1-dB compression point is derived as [13],

$$A_{1dB} \approx \sqrt{0.145\left|\frac{\alpha_1}{\alpha_3}\right|} \tag{2.57}$$

which gives

$$A_{IIP3}\left|\text{dBm} = (A_{1dB} + 9.63)\right|\text{dBm} \tag{2.58}$$

$$A_{1dB}\left|\text{dBm} = (A_I - 4.86)\right|\text{dBm} \tag{2.59}$$

For an handheld RFID reader with 4 W EIRP and 1W output power (6dBi antenna gain), with a 25 dB port isolation from the circulator, the interferer power from the transmitter is,

$$A_I = EIRP - G_a - Isolation = 36 - 6 - 25 = 5(\text{dBm}) \tag{2.60}$$

This means a 9.77 dBm IIP3 and 0.14 dBm 1 dB compression point for the receiver. It can be seen that the receiver has to be highly linear if the transceiver shares one single antenna. For two separated antennas like a stationary RFID reader, the port isolation for the two antennas can be as high as 40 dBm. A -10 dBm IIP3 is then required for the overall system, which relaxes the linearity requirement. Generally, for the same receiver architecture, a tradeoff between noise figure and IIP3 exists. A relaxed IIP3 requirement can contribute a better noise figure performance and thus increase the overall reading range.

### 2.7.4 RFID link-budget and reading range

A homodyne receiver based on [17] is redrawn in Fig. 2.14 with a certain simplification. The input signal and interferer are accepted by the antenna and then passed through a

circulator to a LNA. After they are down converted to the baseband frequency by a LO and mixer, they are filtered by a low pass (LP) filter and amplified by a VGA. The $SNR_{out}$ represents the minimum SNR at that point to guarantee a certain BER after demodulation.

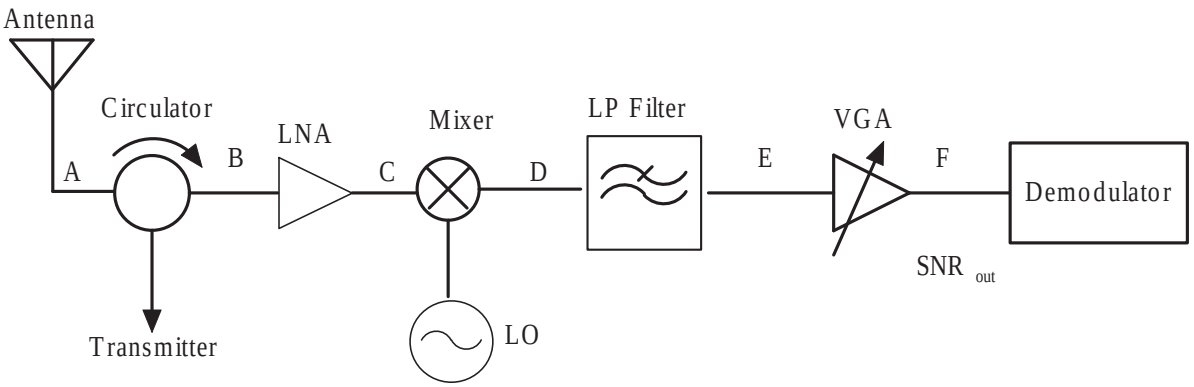


Fig. 2.14 A homodyne receiver structure

A level diagram was built to visualize the NF, IIP3 and gain performance of the receiver. The parameters for the LNA, mixer, LPF and VGA are typical specifications from the datasheet or literature [13].

With a mixer with a 10 dBm IIP3, the overall system has only -4.9 dBm IIP3. For a circulator with 25 dB isolation, the required IIP3 is 9.77 dBm. To achieve the IIP3 requirement, a mixer with 30 dBm IIP3 is required. Therefore, a passive mixer may have to be applied instead. Otherwise some other techniques have to be taken to cancel the interferer from the transmitter.

From Table 2.2, it is also clear that the LNA dominates the noise figure performance when the VGA is in high gain mode. The passive components before the LNA will introduce additional noise figure equal to their loss in dB. When the VGA is in a low gain mode, the

Table 2.2 Level diagram corresponding to the Homodyne receiver

| | Circulator A-B | LNA B-C | Mixer C-D | LPF D-E | VGA E-F |
|---|---|---|---|---|---|
| Stage Voltage Gain /dB | -0.2 | 15 | 10 | -5 | Low Gain: 7.5<br>High Gain: 50 |
| Stage Power Gain /dB | -0.2 | 15 | 1 | -5 | |
| Cumulative Voltage Gain/dB | -0.2 | 14.8 | 24.8 | 19.8 | Low Gain: 27.3<br>High Gain: 69.8 |
| Stage NF/dB | 0.2 | 1.4 | 12 | 5 | Low Gain: 44<br>High Gain: 4 |
| Cumulative NF dB (Low Gain) | 33.2 | 33.0 | 48.0 | 49.0 | 44 |
| Cumulative NF dB (High Gain) | 3.26 | 3.06 | 13.3 | 9.0 | 4 |
| Stage IIP3 (dBm) | ∞ | 12 | 10 | ∞ | 38 |
| Cumulative IIP3 (dBm) | -4.9 | -5.1 | 10.0 | 43.0 | 38 |

noise figure is dominated by the NF of the VGA. The VGA is used to increase the dynamic range of the receiver. The receiver has an overall NF of 3.26 dB. For a far-distance reception, the receiver works at the high gain mode, which corresponding to an IIP3 of -4.9 dBm. The sensitivity of the receiver is calculated by (2.42), which is -106.1 dBm and corresponding to a 1.57 uV signal for a 50 ohm system. For this receiver structure, the maximum received

signal is defined by the IIP3 and noise floor, which is given by (2.45). The noise figure of the receiver is 33.2 dB for the low gain case, which gives a maximum input signal level -12.51 dBm. The SFDR is 89.1 dBm.

Now we're ready to determine the limiting factors for the reading distance of the UHF RFID transponder. For a backscattering communication, the maximum communication distance *R* can be found from (2.37),

$$R = \sqrt[4]{\sigma \frac{P_{in}\lambda^2 G_t^2}{P_r (4\pi)^3}(1-|\Gamma_t|^2)^2 \left|\hat{\rho}_s \bullet \hat{\rho}_r\right|^2} = \sqrt[4]{\sigma \frac{P_{in} c^2 G_t^2}{P_r (4\pi)^3 f^2}(1-|\Gamma_t|^2)^2 \left|\hat{\rho}_s \bullet \hat{\rho}_r\right|^2} \tag{2.61}$$

From (2.23), the RCS is derived as,

$$\sigma = \frac{\lambda^2 G_r}{\pi} \frac{\varepsilon_{cd} R_s^2}{|Z_s + Z_L|^2} = \frac{c^2 D_r}{\pi f^2} \frac{R_s^2 \varepsilon_{cd}^2}{|Z_s + Z_L|^2} \tag{2.62}$$

At the ISM frequency band 902~928 MHz, the center frequency 915MHz is used for the calculation. Assuming there is no polarization loss, the nominal impedance of the RFID transponder IC at -13 dBm input power is 9.9-j60.5 ohms, the radar cross section of the RFID antenna is,

$$\sigma = \frac{D_r c^2}{\pi f^2} \frac{R_s^2 \varepsilon_{cd}^2}{|Z_s + Z_L|^2} = \frac{2.6}{\pi} \times \left(\frac{3\times 10^8 \times 8 \times 0.58}{915 \times 10^6}\right)^2 \times \frac{1}{|8 + j85 + 9.9 - j60.5|^2} \tag{2.63}$$

$$\sigma = 0.00208(\mathrm{m}^2)$$

With a receiver sensitivity of -106.1 dBm, the maximum reading range without mismatch between transmitter antenna and generator and polarization loss is given by (2.61) ,

$$R = \sqrt[4]{\sigma \frac{P_{in} c^2 G_t^2}{P_r (4\pi)^3 f^2}(1-|\Gamma_t|^2)^2 \left|\hat{\rho}_s \bullet \hat{\rho}_r\right|^2} = 92.6(\mathrm{m}), \tag{2.64}$$

which is really large since the normal tested reading range is less than 10 meters.

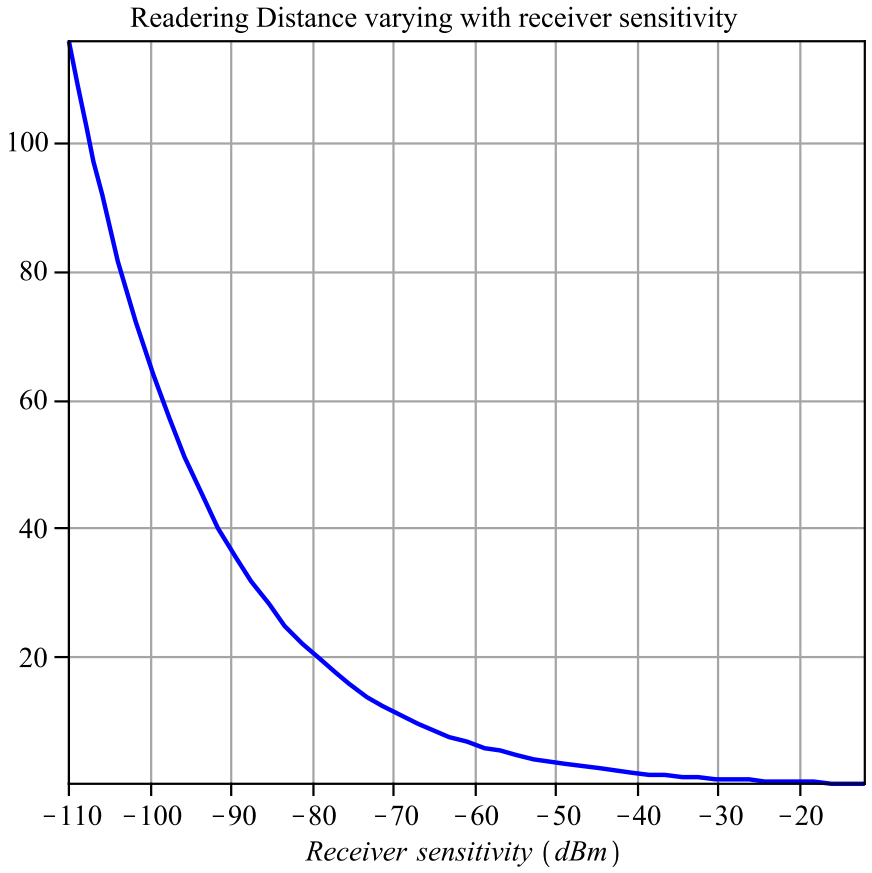


Fig. 2.15 Reading distance vs receiver sensitivity

As shown in Fig. 2.15, for -90 dBm sensitivity, 36.6 m reading range can be achieved. A -80 dBm sensitivity corresponds to 20.6 m reading distance. Perfect matching can boost the reading range of the -80 dBm sensitivity to 28.4 m. Since ASK can not reflect power at all digits, assuming the power is scattered back during the 50% time period, the reading range will reduce 16%. The maximum allowed signal level is -12.51 dBm, which corresponds to a 0.42 m reading distance.

Because the passive RFID tag achieves about 10-meter reading range, some other limitations have to be found out. The passive RFID tag has a rectifier at the front end to

generate DC voltage. The rectifier usually has very low overall efficiency (15%~20%) [15]. It has been reported [15] that a 16.7 uW RF power is possible to power up the passive RFID transponder and perform the communication. For a RFID transponder antenna with a directivity of 4.15 dBi and radiation efficiency 58%, the reading distance tested by a Symbol MC9000-G RFID reader can be calculated by the Friis Transmission Equation [5],

$$R = \frac{\lambda}{4\pi}\sqrt{\frac{P_t G_t G_r}{P_r}} \approx 15.68(\text{m}) \tag{2.65}$$

The distance is closer to the practical maximum reading distance for most of the passive RFID transponders tested by a handheld RFID reader. Our tested results in Chapter 4 will verify that the key limiting factor to the reading range of a passive RFID transponder is the low efficiency of the rectifier and multiplier. For an active RFID transponder, the dominant limiting factor to the reading range is the sensitivity of the receiver.

# CHAPTER 3 METAMATERIAL AND ITS APPLICATION TO METAL SURFACE MOUNTED RFID

## 3.1 Introduction

When a RFID dipole antenna is placed horizontally above a metal surface, due to the out of phase image current immediately below the metal surface, the electromagnetic waves radiated by the original and image currents will approximately cancel each other so that the total radiated power is approximately zero. Since the antenna is a reciprocal device, for the same reason, the antenna is not able to receive the signal or power from a RFID reader.

In this chapter, it'll be shown that metal surface mounted dipole antenna has a very low radiation efficiency. Our analyses in Chapter 2 demonstrate that when the transponder antenna has radiation efficiency approximately zero, the reading distance will be zero.

Some potential solutions to improve the radiation efficiency of metal surface mounted RFID transponder are discussed. The distinct properties of a metamaterial such as a frequency selective surface (FSS) [22] and a mushroom-like electromagnetic bandgap (EBG) surface [23] are explored. Our study shows that the FSS and mushroom-like EBG exhibit very similar reflection phase profiles and bandgap properties. Their application to boost the efficiency of the metal-surface mounted RFID dipole antenna is experimentally verified.

## 3.2 Potential solutions for metal surface mounted RFID transponders

- **Increasing the distance between a UHF RFID transponder antenna and metal ground**

The similarities between transmission of a plane wave and a transmission-line equation allow us to treat the free space as an array of parallel plate waveguides. If the dipole antenna has a minimum distance $\lambda/4$ from the PEC ground, as shown in Fig. 3.1 (a), the input impedance of the dipole antenna can be found from the equivalent transmission model shown in Fig. 3.1 (b). The input impedance at the antenna position is derived by the following equation [6],

$$Z_{in} = Z_0 \frac{Z_L + jZ_0 \tan(\beta l)}{Z_0 + jZ_L \tan(\beta l)} = jZ_0 \tan(\frac{\pi}{2}) = j\infty \qquad (3.1)$$

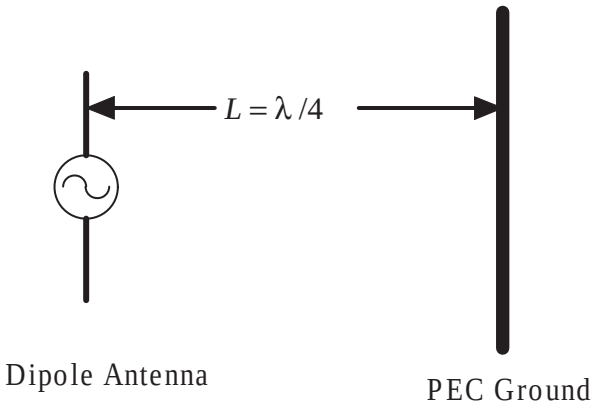


Fig. 3.1 (a) Dipole antenna above a PEC ground at a quarter-wavelength distance

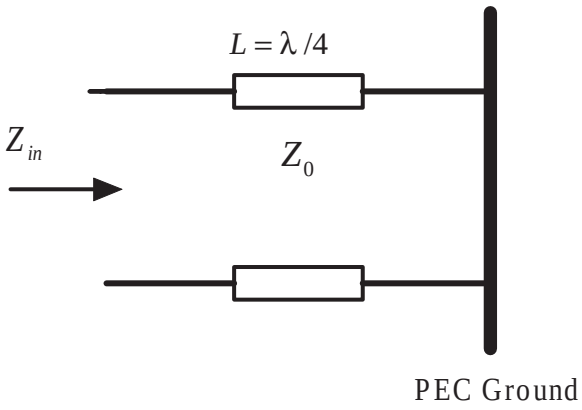


Fig. 3.1 (b) Equivalent circuit to calculate the input impedance

The major disadvantage of this approach is that a quarter-wavelength in free space at 915 MHz is about 8 cm, which is too large for most RFID applications. The method to calculate the radiation impedance of the dipole antenna is not fully accurate since the distance between the dipole antenna and ground surface is less or equal to $\lambda/4$, which is still in the Fresnel near-field region. In this region, an existing electric field in the radial direction can't be accounted for by the parallel plate transmission line model. However it shows approximately that at a distance of $\lambda/4$ from the PEC ground, the antenna input impedance would be boosted rather than being shorted out.

A quarter-wavelength dipole antenna at 915 MHz with a radius of 0.5 mm has an input impedance of 83+j56 in free space according to the HFSS simulation. If the dipole antenna is located at $\lambda/4$ distance from an infinite PEC ground, the input impedance of the dipole antenna increases to 99.6+j92. Therefore, for a real good impedance matching, the distance between the dipole antenna and ground has to be different from a quarter wavelength.

- **Inserting high permeability isolator**

Magnetic material with a high permeability would increase the characteristic impedance of the material between the antenna and ground. In this way, even with a distance smaller than one quarter wavelength in air, the source driving the antenna still sees a relatively large impedance. The disadvantage with this method is that the magnetic material is lossy in the GHz frequency range, which dramatically reduces the radiation efficiency of the dipole antenna as will be shown in Chapter 4. These materials are very heavy and their cost is high.

- **Using metamaterial or left-handed material to isolate the metal ground**

Recently, it has been reported [22] [23] [24] that metamaterials' or left-handed materials' own distinct characteristics in a certain frequency band which can be used to block the shorting effects of the ground surface. Another similar idea was to build an electromagnetic (EM) absorber such as placing a frequency selective surface (FSS) above a PEC ground plane to absorb the incident wave without reflection.

- **Changing the structure of the RFID tag antenna**

Some antenna structures are known to be able to work on metal, for example a microstrip antenna. It may be possible to shrink the size and thickness of the microstrip antenna to make it suitable for use on a metal surface. Two major types of novel metal-surface mountable RFID transponder antenna were invented, simulated and experimentally verified. The details are developed in Chapter 4.

## 3.3 Frequency Selective Surface

### 3.3.1 Introduction

One of the largest challenges for the RFID industry has been the low radiation efficiency of the transponder when it is horizontally attached to a smooth conductive surface. A modified conductive surface with a periodic structure was discovered to exhibit a high impedance electromagnetic band gap (EBG) characteristic in a certain frequency band [24]. The mushroom-like structure would reflect an incident plane wave in phase rather than out of phase as would be expected from a smooth metal surface. The tangential electric field on the surface isn't shorted out as with a normal metal ground surface. Its application to antennas

has been extensively studied in [22] [23] [24] [25] [26]. It is shown that EBG structures can be utilized to improve radiation efficiency of a metal-surface mounted wire antenna.

Although mushroom-like EBG structures [24] can be built on RF boards by modern printed circuit technology, vias in the mushroom-like structure connecting the upper and lower metal surfaces increase the production cost. A periodic mushroom-like structure without vias can be classified as a frequency selective surface (FSS) [27]. The integration of a square patch FSS and dipole antenna has been found to constitute a surface wave antenna [28]. Their application to high gain planar antennas is reported in [29]. Previous work considered mainly the reflection phase characteristics of a FSS. With a zero degree reflection phase, the material can be specified as a perfect magnetic conductor (PMC). However, this approach needs to be improved since it doesn't consider the complex near field interaction between an antenna and a FSS. In this dissertation, a novel design approach based on transverse magnetic (TM) and transverse electric (TE) wave properties is demonstrated [22]. The topic of a FSS on boosting the radiation efficiency of a half-wavelength dipole is treated in more detail.

A planar 2D periodic patch array was first designed based on an LC equivalent model and 3D electromagnetic simulation. In order to experimentally study the effects of the FSS to boost the radiation efficiency of metal-surface mounted dipole antennas, the structure was fabricated on a FR4 board. Transmission properties of a TM and a TE wave along the surface were studied and measured in the lab. Our study found that when dipole antennas are resonant in a frequency band where a TM wave is suppressed but a TE wave is supported, the dipole antennas can be easily integrated onto a FSS with very good input matching and radiation efficiency.

With the purpose of simulating the real wireless communication environment, a two-port

network analyzer was operated as a transmitter and a receiver. Two half-wave dipole antennas were connected to the transmitting port and receiving port of the network analyzer. By means of S parameter measurements, the radiation efficiency of a dipole antenna in free space, horizontally above a normal metal surface and above a FSS were evaluated. Measured results of return loss and transmission coefficient demonstrate that the FSS structure can be utilized to effectively enhance the radiation efficiency when low profile wire antennas backed by a metal surface are desired.

### 3.3.2 Reflection phase above a PEC, PMC and FSS

As shown in Fig. 3.2, a TEM plane wave propagates along the negative $x$ direction and is perpendicularly incident to an FSS at the $yoz$ plane. The incident and reflected electric fields are written as,

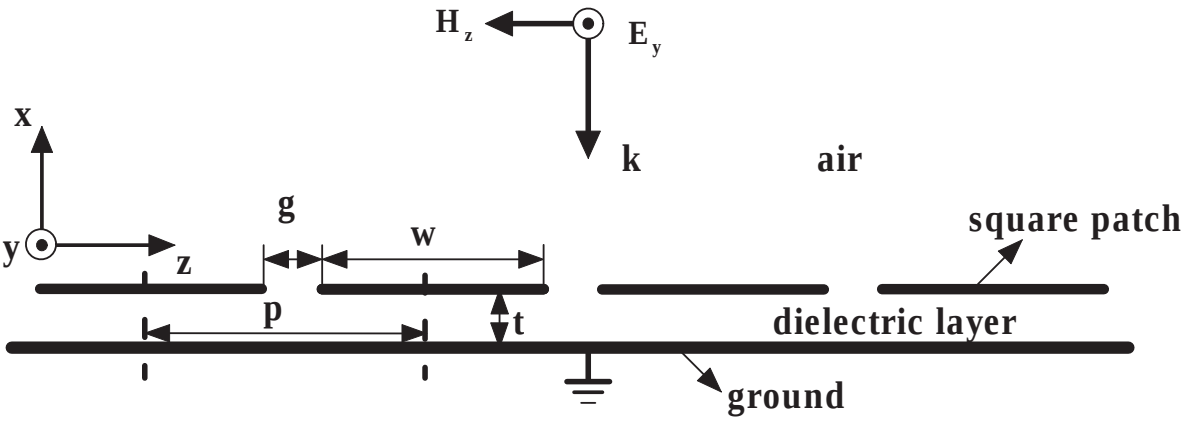


Fig. 3.2 A plane wave incident to a FSS backed by metal ground

$$\boldsymbol{E}_{inc} = \mathbf{a}_{\mathrm{y}} E_0 e^{jkx} \tag{3.2}$$

$$\boldsymbol{E}_{ref} = \mathbf{a}_{\mathbf{y}} \Gamma E_0 e^{-jkx} \tag{3.3}$$

where $k$ is the wave number and $\Gamma$ is the reflection coefficient, the phase of $\Gamma$ defines the reflection phase of the surface.

The similarities between the transmission of a plane wave and a transmission-line wave allow us to treat the free space as an array of parallel plate waveguides. Assuming each parallel plate waveguide has a width $w$ and a height $h$, a simple relationship between the electric field $E$ and voltage $V$ and the magnetic field $H$ and current $I$ holds,

$$E = \frac{V}{h}\ ,\ H = \frac{I}{w} \tag{3.4}$$

Therefore the wave impedance $\eta$ can be written as,

$$\eta = \frac{E}{H} = \frac{V}{I}\frac{w}{h} \tag{3.5}$$

It is then obvious that the voltage reflection coefficient is equal to the reflection coefficient of the electric field. For the square patch case, we choose $w$ equal to $h$.

Therefore the wave impedance is equal to the characteristic impedance of the transmission line,

$$\Gamma_L = \frac{Z_L - Z_0}{Z_L + Z_0} = \frac{Z_L - \eta}{Z_L + \eta} \tag{3.6}$$

Mushroom-like EBG structures can be approximated by a LC circuit model [30]. Fringing capacitance C between two metal patches is derived by conformal mapping. Inductance L at resonance is derived by a solenoidal approximation. Even though the LC model was developed based on a mushroom-like EBG structure, our simulated and experimental results demonstrate that the formula from [30] predicts the resonant frequency of a FSS reasonably well. The formulas are listed here,

$$C = \frac{w\varepsilon_0(1+\varepsilon_r)}{\pi}\cos h^{-1}(\frac{p}{g}) \tag{3.7}$$

$$L = \mu_r t \tag{3.8}$$

where the period $p$ is defined as the shortest distance between the centers of any two metal patches, $g$ is the space between two metal patches, and $t$ is defined as the distance from the top metal layer to the ground metal layer and is equal to the thickness of the board material.

For an infinite square array with a period of 19 mm, width 18 mm, gap 1 mm, dielectric thickness 1.5 mm and dielectric constant 4.17, (3.7) and (3.8) give an effective capacitance of 0.95 pF and an equivalent inductance of 1.89 nH, respectively. The calculated resonant frequency is 3.76 GHz. The FSS was made on a FR4 board, whose photograph is shown in Fig. 3.3.

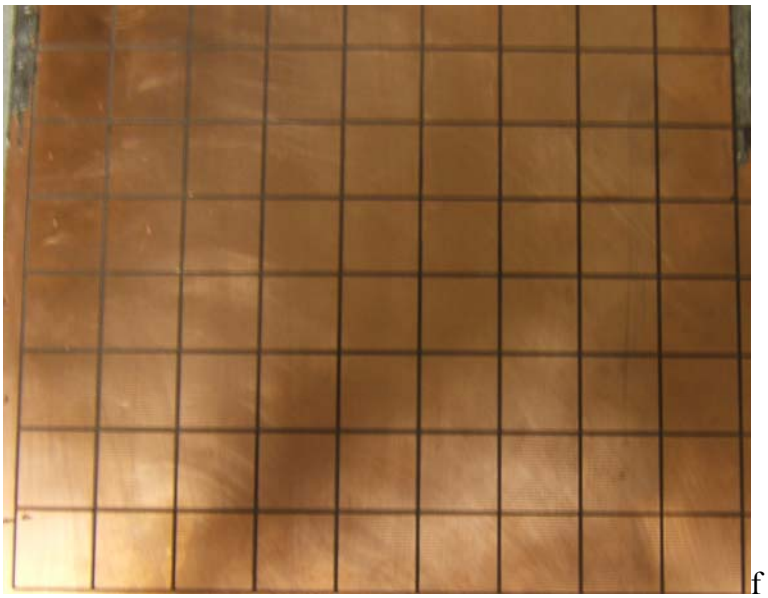 f

Fig. 3.3 Fabricated square patch FSS using FR4 board with a period of 19 mm, width 18 mm, gap 1 mm and board thickness 1.5 mm

When the artificial parallel plate transmission line has the FSS as its load terminal, the load is equivalent to a shunt inductance $L$ and capacitance $C$. The equivalent model for a plane wave normally incident to the EBG surface is shown in Fig. 3.4.

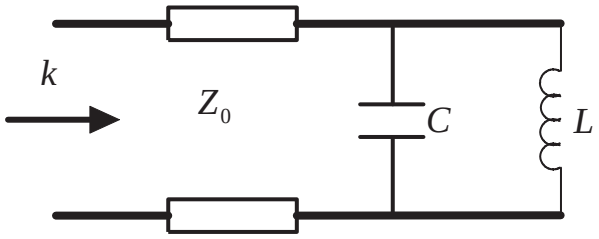


Fig. 3.4 Transmission line equivalent circuit for a plane wave incident to the EBG surface

The load impedance is written as,

$$Z_L = \frac{j\omega L}{1-\omega^2 LC} \tag{3.9}$$

The inductance in a unit cell and the gap capacitance between two square patches are calculated by (3.7) and (3.8).

At the parallel resonance frequency, magnetic energy and electric energy exchange back and forth between them. The load input current is zero for a lossless resonator. Thus the equivalent load impedance is infinite. From (3.6), the reflected electric field is in phase with the incident field.

From (3.6) and (3.9), the reflected phase of the EBG surface is derived as,

$$phase(\Gamma_L) = phase(\frac{j\omega L - \eta(1-\omega^2 LC)}{j\omega L + \eta(1-\omega^2 LC)}) \tag{3.10}$$

In phase reflection in a certain frequency band is a major nature of a FSS or a mushroom-like EBG structure. An infinite periodic array can be simulated more efficiently by a unit cell

since the electric field and magnetic field at different cells are related by a phase shift. Time harmonic electric field in an infinite planar periodic array with a period $D_x$ and $D_y$ can be found by Floquet's equation [27],

$$\boldsymbol{E}(x+D_x, y+D_y, z) = \boldsymbol{E}(x,y)e^{-j(\beta_x D_x+\beta_y D_y)}e^{-j\beta_z z} \tag{3.11}$$

where $\beta_x$ $\beta_y$ and $\beta_z$ are wave numbers in x, y and z direction, respectively.

A full-wave 3D EM simulation software HFSS [10] is utilized to analyze the infinite periodic structure. The reflection phase characteristics of a FSS are extracted using the same

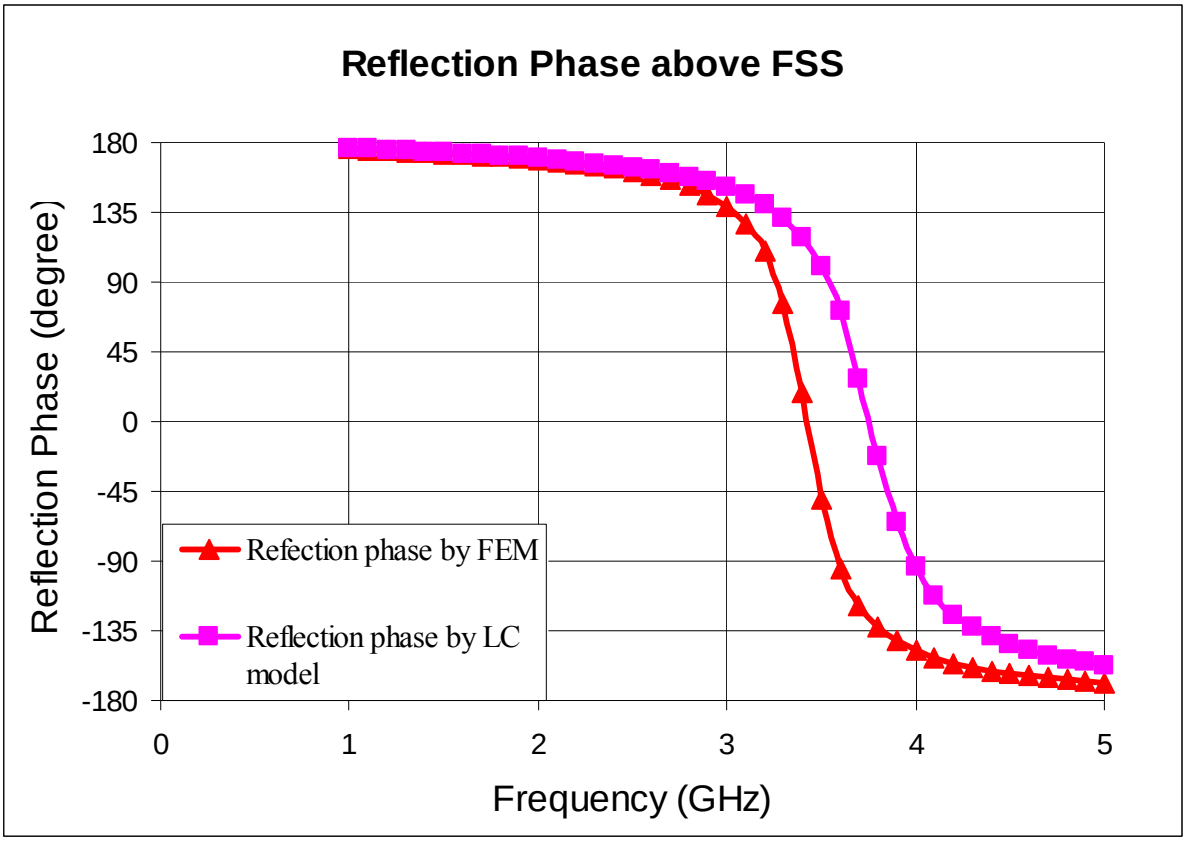


Fig. 3.5 Calculated and simulated reflection phases above a FSS made by FR4 board with a period of 19 mm, width of metal patch 18 mm and thickness 1.5 mm

method as [24]. The resonant frequency is defined when the reflection phase at the FSS is equal to zero. In Fig. 3.5, the reflection phase derived from HFSS simulation is plotted in solid line with triangle symbols, which shows a resonant frequency of 3.42 GHz. The calculated reflection phase based on (3.10) is plotted in solid line with square symbols. A good agreement is observed but the analytical model gives a higher resonant frequency. The reason is that the capacitance derived by the conformal mapping doesn't account for the effects of the ground metal surface, which makes the calculated capacitance smaller than it should be.

The zero degree reflection phase corresponds to a parallel resonant frequency of the unit cell, where magnetic energy and electric energy exchange forever. The lossless parallel LC resonator has infinite input impedance and zero input current. From (3.6) and (3.9), it can be seen that the reflected electric field is in phase with the incident electric field. The FSS at the resonant frequency resembles a perfect magnetic conductor (PMC). Since on a PMC surface, in order to satisfy the boundary condition, the sum of the total tangential magnetic fields should be zero, the reflected tangential magnetic field should be 180 degrees out of phase compared to the incident magnetic field near the surface. Therefore, the tangential electric field doesn't have any phase change in order to maintain the propagation direction of the reflected wave. For a PEC surface, to satisfy the boundary condition of zero tangential electric field, the tangential electric field has to be 180 degrees out of phase compared to the incident electric field near the surface, which is seen from (3.9) by letting load impedance to be zero for a PEC case.

### 3.3.3 Radiation characteristics based on reflection phase

By image theory, a dipole antenna above a PEC surface can be treated as a two-dipole antenna array which has a 180 degree phase difference between the two excitation currents [5]. Based on the theory of a phase array, the radiation characteristics of a dipole antenna above a surface which has any reflection phase can be derived analytically.

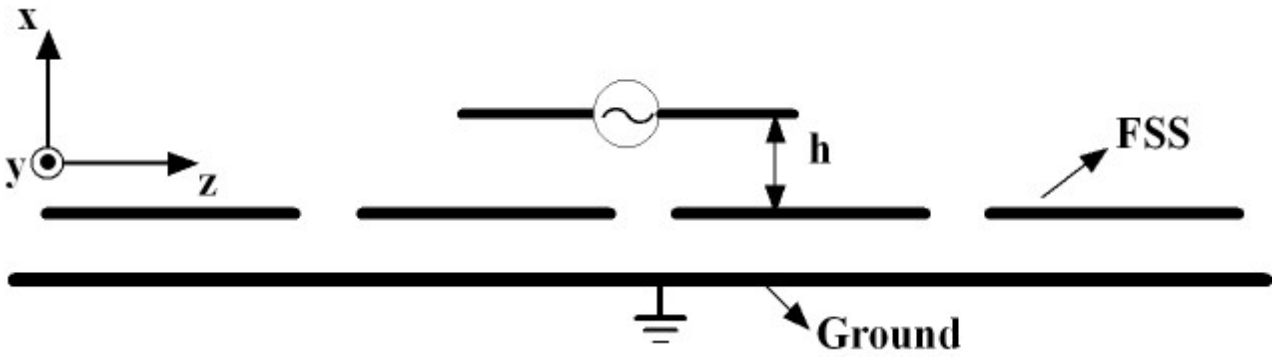


Fig. 3.6 Dipole antenna horizontally placed above a FSS

As shown in Fig. 3.6, a dipole oriented in the z axis is placed on the x axis with a vertical distance h from the FSS with reflection phase $\beta$. The array factor can be derived as [5],

$$\text{Array factor} = 2\cos(kh\sin\theta\cos\phi - \beta/2) \tag{3.12}$$

The element factor based on the placement of the dipole can be written as:

$$\text{Element factor} = j\eta\frac{I_0 e^{-jkr}e^{j\beta/2}}{2\pi r}\left[\frac{\cos(\frac{kL}{2}\cos\theta)-\cos(\frac{kL}{2})}{\sin\theta}\right] \tag{3.13}$$

where $L$ is the length of the dipole antenna

The total far field $E_\theta$ is equal to the product of array factor and element factor. The radiation resistance, gain and radiation pattern can then be derived once the total field is known.

If the dipole is placed closely above a PEC surface, β is equal to 180 degrees and $kh \approx 0$. The array factor is almost zero. In the limit, no electric field would be radiated and the radiation resistance becomes,

$$R_r = \frac{P_{rad}}{I^2} \approx 0(\Omega) \tag{3.14}$$

When the dipole is placed closely above a PMC surface, β is 0 degree and $kh \approx 0$. The array factor is equal to two. The electric field radiated by the dipole array is twice of that of one dipole antenna. It is predictable that the radiation resistance should be doubled. The array factor shows that the total radiation pattern is affected by the distance *h* and reflection phase β. One of the limitations of this approach is that the near field interaction between dipole antennas and the substrate surface have not been considered since the above formulas are based on the far field approximation.

### 3.3.4 Radiation impedance of the dipole antenna above a finite PEC surface

When a dipole antenna is placed closely above a PEC surface, a TEM plane wave propagates in the region immediately between the antenna and PEC surface. In other words, the metal conductor of the antenna and the PEC surface create a microstrip line. Due to the odd symmetry, in order to short out the dipole antenna, the PEC plane doesn't require a huge size. Table 3.1 shows the variation of the input impedance when the width of the PEC plane is varied but the length is kept the same as is computed by HFSS V10 [10]. The vertical distance is 1 mm between the dipole antenna and PEC surface. The width of the dipole arm is w. The results show that a very narrow PEC or conductor can short out the dipole antenna.

Table 3.1 Input impedance of a quarter-wavelength dipole above a PEC Plane by HFSS simulation

| Width of the PEC/PMC plane Length = $\lambda/2$ | Input Impedance (Ohms) |
|---|---|
| Infinite large | 0.27-j13.1 |
| 64w | 0.50-j12.0 |
| 32w | 0.51-j12.0 |
| 16w | 0.77-j11.8 |
| 8w | 1.28-j11.6 |
| 4w | 2.84-j9.7 |
| 2w | 5.6-j7.2 |
| 1w | 9.4-j4.4 |
| 0.5w | 13.3-j6.6 |
| 0 (in free space) | 71.7-j0.71 |

### 3.3.5 TM, TE wave measurements

Since any field configuration can be derived by a linear superposition of TE and TM modes, it is very instructive to measure the transmission properties of TE and TM waves across the FSS. Two monopole probes fed by coaxial cables were built and soldered to the FSS board. For TM wave measurements, as shown in Fig. 3.7, two vertical monopole probes oriented in the x direction were placed on the surface [24]. In this case, the magnetic field primarily has a tangential y component, and electric fields have normal x and tangential z components. The existence of an electric field in the z direction is necessary in order to compensate for the loss

and sustain the flow of surface current along the z direction.

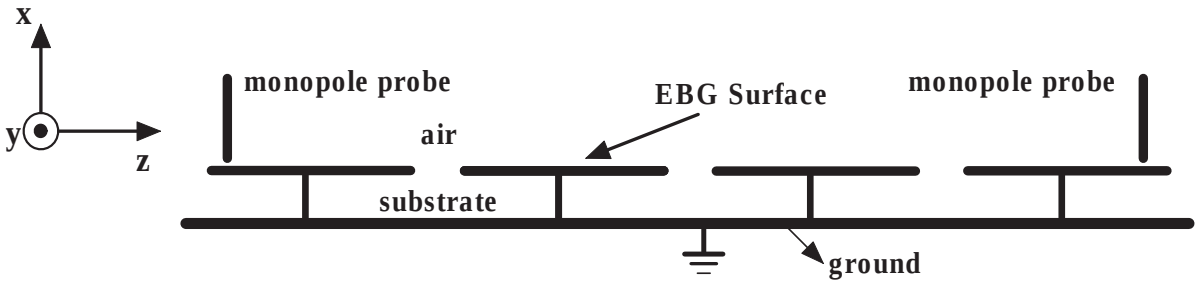


Fig. 3.7 Cross-section view of the TM wave measurements

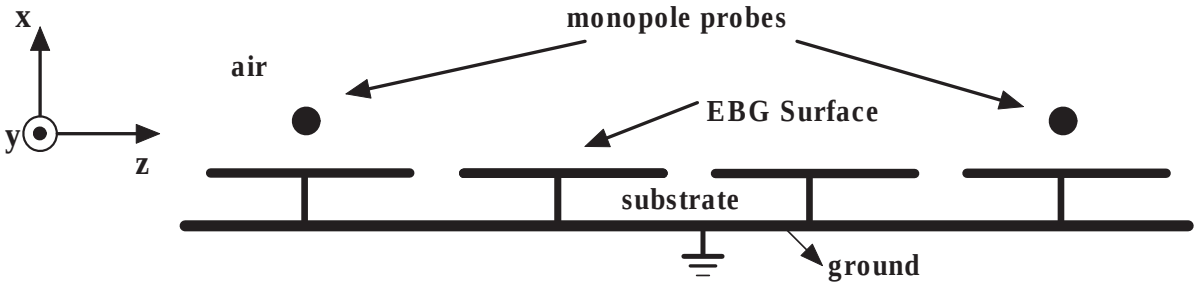


Fig. 3.8 Cross-section view of the TE wave measurements

For TE wave measurements as shown in Fig. 3.8, two horizontal monopole probes oriented in the y direction were placed above the surface with a small distance [24]. The electric field primarily has a tangential y component, and magnetic fields have normal x and tangential z components.

Measured transmission properties of TM and TE waves across the FSS are illustrated in Fig. 3.9 (a) and (b), respectively. Transmission of the TM wave drops significantly from -25 dB at 3.3 GHz to below -50 dB at 3.8GHz, which is the TM wave bandgap frequency band.

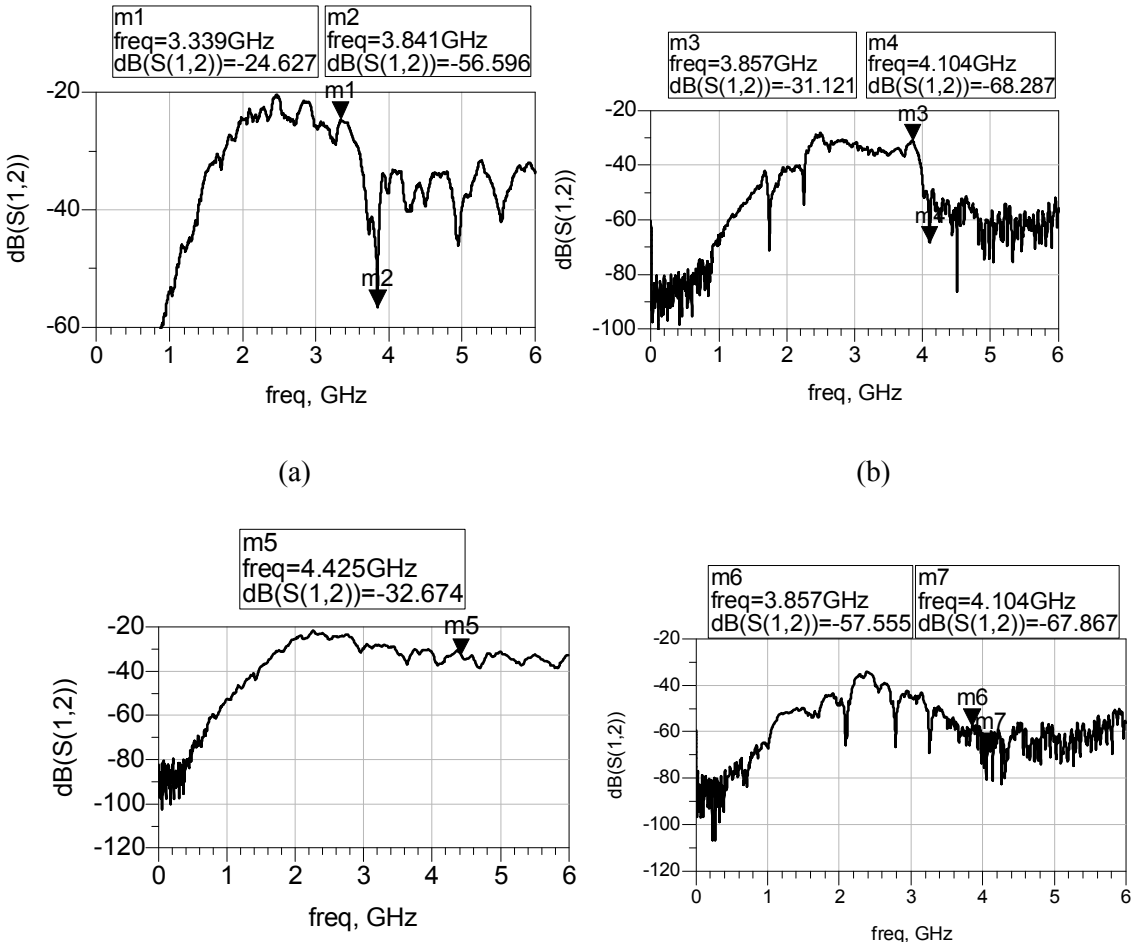


Fig. 3.9 (a) Transmission of TM wave across the frequency selective surface

(b) Transmission of TE wave across FSS

(c) Transmission of TM wave across a smooth metal surface

(d) Transmission of TE wave across a smooth metal surface

Transmission of the TE wave drops noticeably around 3.85 GHz from -31 dB to below -60 dB at 4.0 GHz. From 2.5 GHz to 3.85 GHz, the transmission coefficient is maintained at a relatively flat level about -30 dB. In order to examine the difference, the transmission property of a TM wave across a metal surface is shown in Fig.3.10 (c) and is relatively flat at

around -33 dB. It is clear from Fig. 3.10 (d) that the TE wave can not be supported by a flat metal surface.

### 3.3.6 Metal-surface mounted dipole antenna

#### A. Metal surface mounted dipole antenna design issues

Metal surfaces can be combined with an antenna to build reflector antennas and increase radiation in a certain direction. However, when a metal surface is horizontally placed below a dipole antenna, the image current forces the tangential electric field at the metal surface to be zero. The image current becomes 180 degree out of phase with the original current. The driving-point impedance of two side-by-side antennas 1 and 2 can be represented by the following equations [5],

$$Z_{1d} = \frac{V_1}{I_1} = Z_{11} + Z_{12}\frac{I_2}{I_1} \tag{3.15}$$

$$Z_{2d} = \frac{V_2}{I_2} = Z_{22} + Z_{21}\frac{I_1}{I_2} \tag{3.16}$$

where $Z_{11}$ and $Z_{22}$ are the input impedances of antennas 1 and 2 in free space, $Z_{12}$ and $Z_{21}$ are the mutual impedances due to the existence of each other. When the distance between antennas is very small, the mutual impedance becomes equal to the self impedance thus radically changing the driving-point impedance $Z_{1d}$ or $Z_{2d}$. The driving-point impedance would be reduced to zero with two currents of equal magnitude but opposite phases. This corresponds to the case when a dipole antenna is horizontally placed above a PEC plane within a very short distance. The driving-point impedance can also be doubled if the PEC

plane is replaced by a perfect magnetic conductor (PMC) plane.

When a PEC surface is placed horizontally below a dipole antenna, only a vertical electric field and tangential magnetic field exist and propagate along the surface. If the PEC surface is replaced by a flat metal surface, an axial electric field has to exist to compensate for the power loss due to the finite electric conductivity of the metal. A TM surface wave along the surface would be excited and propagate across the metal surface, reducing the driven-point input impedance of the dipole antenna.

When a PMC plane is placed horizontally below a dipole antenna, a normal magnetic field and a tangential electric field exist and propagate along the surface. If the PMC surface is replaced by a magnetic surface with a finite magnetic conductivity, an axial magnetic field would exist. A TE surface wave along the surface would be excited and it would propagate along the surface, increasing the driving-point impedance of the dipole antenna. Since on a PEC surface, the tangent electric field and normal magnetic field are zero, a smooth metal surface has the nature to suppress a TE surface wave but support a TM surface wave across the surface.

In order to boost the input impedance when the dipole antenna is placed horizontally above a FSS, a TM surface wave on the surface should be suppressed since it reduces the input impedance. However a TE surface wave on the surface should be supported since the mode would increase the input impedance. Based on the results of TM and TE wave measurements shown in Fig.2.7 (a) and (b), 3.722 GHz is chosen since it falls into the TM surface wave band gap but is located within the transmission band of a TE surface wave. Experimental results are shown in the next subsection.

**B. S parameters measurements**

Two half-wavelength dipole antennas which have a length around 0.47λ at 3.722 GHz were built and matched to a 50 ohm coaxial cable. They were connected to the transmitter and receiver ports of a network analyzer, respectively. When two well matched (including impedance match and polarization match) dipole antennas radiate in free space with a distance 21.4 cm, the power gain obeys Friis transmission equation [5],

$$\frac{P_r}{P_t} = (\frac{\lambda}{4\pi R})^2 G_t G_r \tag{3.17}$$

By substituting the free space wavelength $\lambda$ at 3.722GHz, the gain of a dipole antenna 1.643, and a spacing of 21.4 cm, $S_{21}$ can be calculated as -26.2 dB since the power gain with perfect matching can be reduced to $S_{21}$ (in dB) [20].

Measured data plotted in Fig.3.10 (a) gives -25.3 dB at 3.722 GHz, which shows a good agreement with the theoretical result. Fig. 3.10 (b) shows that a flat metal plate at a close distance from the antenna will cause an impedance mismatch and low radiation efficiency.

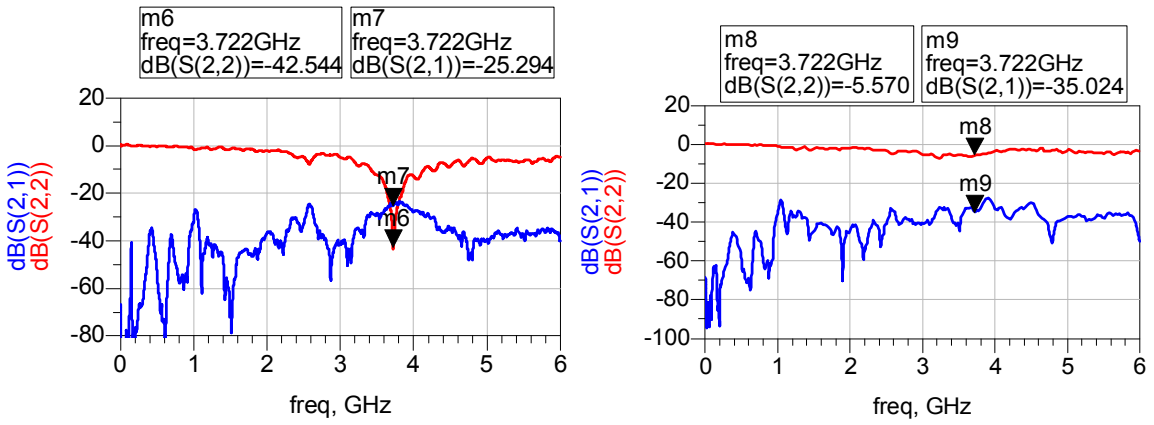


(a) (b)

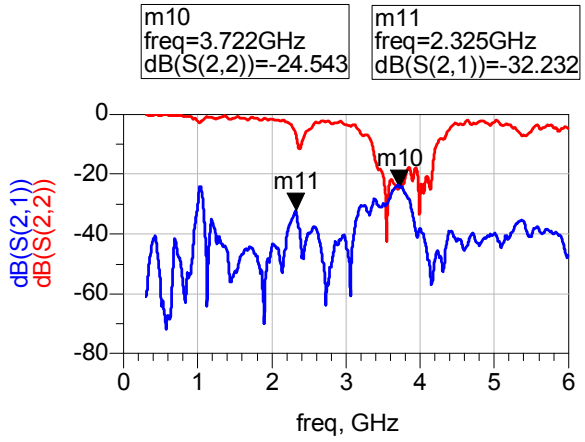


Fig. 3.10 (a) S parameters of two dipole antennas communicating in free space

(b) S parameters when one piece of metal is put parallel to one dipole antenna with 1 mm distance

(c) S parameters when FSS is put parallel to one dipole antenna with 1 mm distance

As shown in Fig. 3.10 (c), when a board with a FSS is placed parallel to one dipole antenna with 1 mm spacing, the transmission coefficient maintains the same level as the free space case but the return loss is enhanced from -5.6 dB to -24.5 dB. Since the impedance mismatching reduces, the radiation efficiency would increase evidently.

## 3.4 Mushroom-like electromagnetic bandgap material

### 3.4.1 Introduction

As an extension of our research on a low profile dipole antenna backed by a frequency selective surface (FSS) [22], further research finds that the same design approach is applicable to a mushroom-like high impedance EBG surface. The mushroom-like EBG surface is shown in Fig. 3.11.

Transmission properties of a TM and a TE wave on the EBG surface were measured using two monopole antennas. Their different effects to vary the antenna input impedance are discussed. A dipole antenna integrated with the EBG ground surface was built based on the new design approach [23]. A two-port network analyzer is utilized to verify the improvement of radiation efficiency of the low profile dipole antenna.

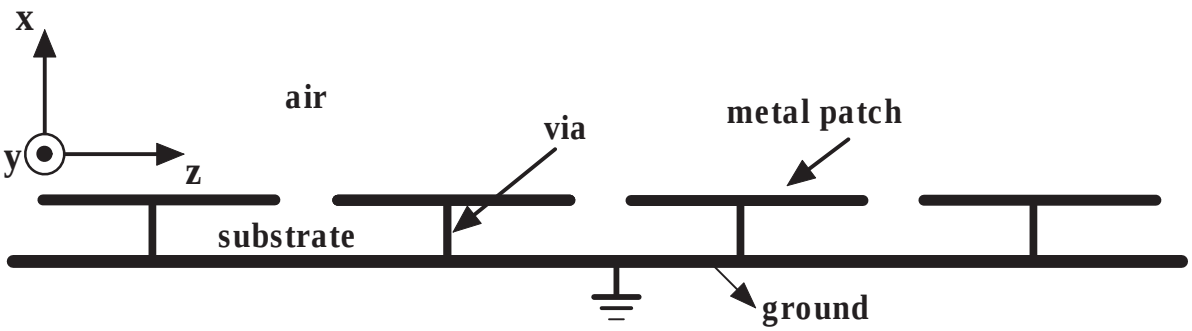


Fig. 3.11 Coordinates and side view of the mushroom-like EBG

### 3.4.2 Design of a mushroom-like EBG structure

For an infinite array with a period of 19 mm, width 18 mm, gap 1 mm, dielectric thickness 1.5 mm and dielectric constant 4.17, the reflection phase profile shows the resonant frequency is around 3.42 GHz, which was derived by a 3D EM simulation tool and shown in Fig. 3.12. If the vias in the mushroom-like EBG are removed and the other parameters are kept the same, the reflection phase is almost the same [22]. A 9 by 8 square patch array was fabricated on a FR4 board with length 18 cm, width 15 cm and thickness 1.5 mm. Each via has a diameter of 0.5 mm made by copper wire. Fig. 3.13 shows the photograph of the fabricated board.

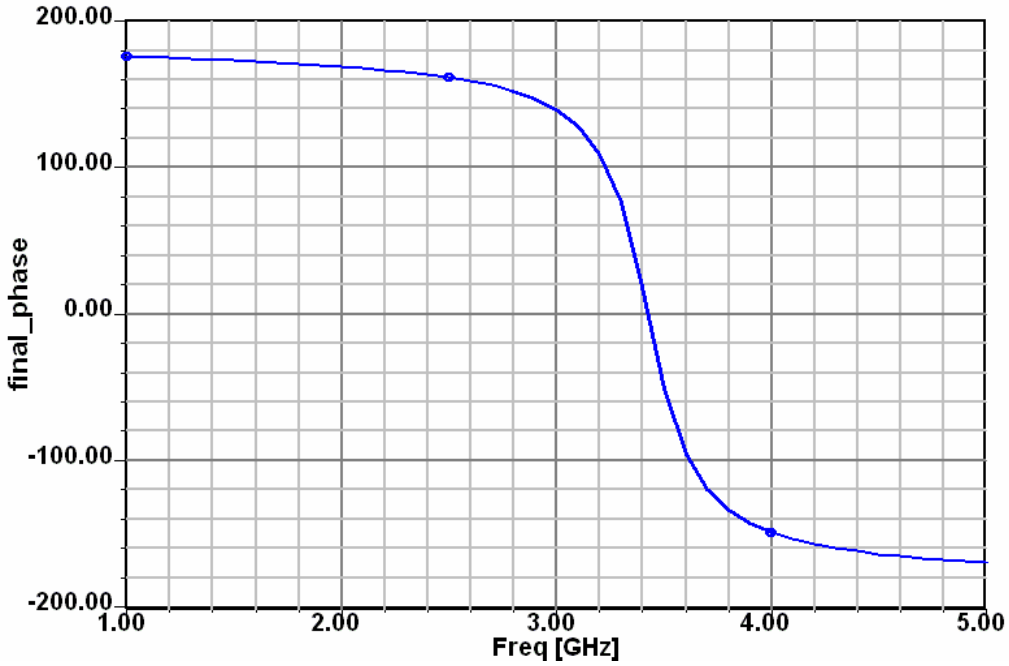


Fig. 3.12 Reflection phase of mushroom-like EBG surface

Fig. 3.13 Fabricated EBG surface using FR4 board with length 18 cm, width 18 cm and thickness 1.5 mm

### 3.4.3 TM and TE waves

When a surface wave is guided by a planar interface, it is very similar to a plane wave except that it has an exponential attenuation normal to the interface. A detailed study of the transmission characteristics of TM and TE waves along the mushroom-like EBG structure would allow us to understand the complex near field interaction between the dipole antenna and EBG surface.

Transmission properties of a TM and a TE wave on the EBG surface and a smooth metal plane are shown in Fig. 3.14. The transmission coefficient of a TM wave across the EBG surface changes from -27 dB at 3.5GHz to below -50 dB at 3.74 GHz, which confirms the existence of the TM wave bandgap. The transmission coefficient of a TM surface wave on a smooth metal surface is kept at a relatively flat level of about -31 dB over the frequency band from 3 GHz to 6 GHz, which shows a smooth metal surface is capable of guiding TM waves. The result agrees with the theoretical conclusion that a TM surface wave should be guided by an inductive surface. During the TM bandgap frequency, the EBG surface exhibits different characteristics from that of a normal metal surface. For a TE wave on a smooth metal surface, the transmission level is almost flat at -60 dB. When the frequency is lower than 4 GHz, transmission coefficients of the TE wave on the EBG surface are always 10 dB higher than on the metal surface. It demonstrated that a planar metal surface naturally suppresses a TE surface wave but the capacitive EBG surface supports it. It is consistent with the conclusion that a TE surface wave has to be guided by a capacitive surface.

When a dipole antenna is placed closely and horizontally above a good metal ground surface, a TM wave is guided on the interface but a TE wave is naturally suppressed. The input impedance of the dipole antenna will decrease dramatically since the vertical electrical

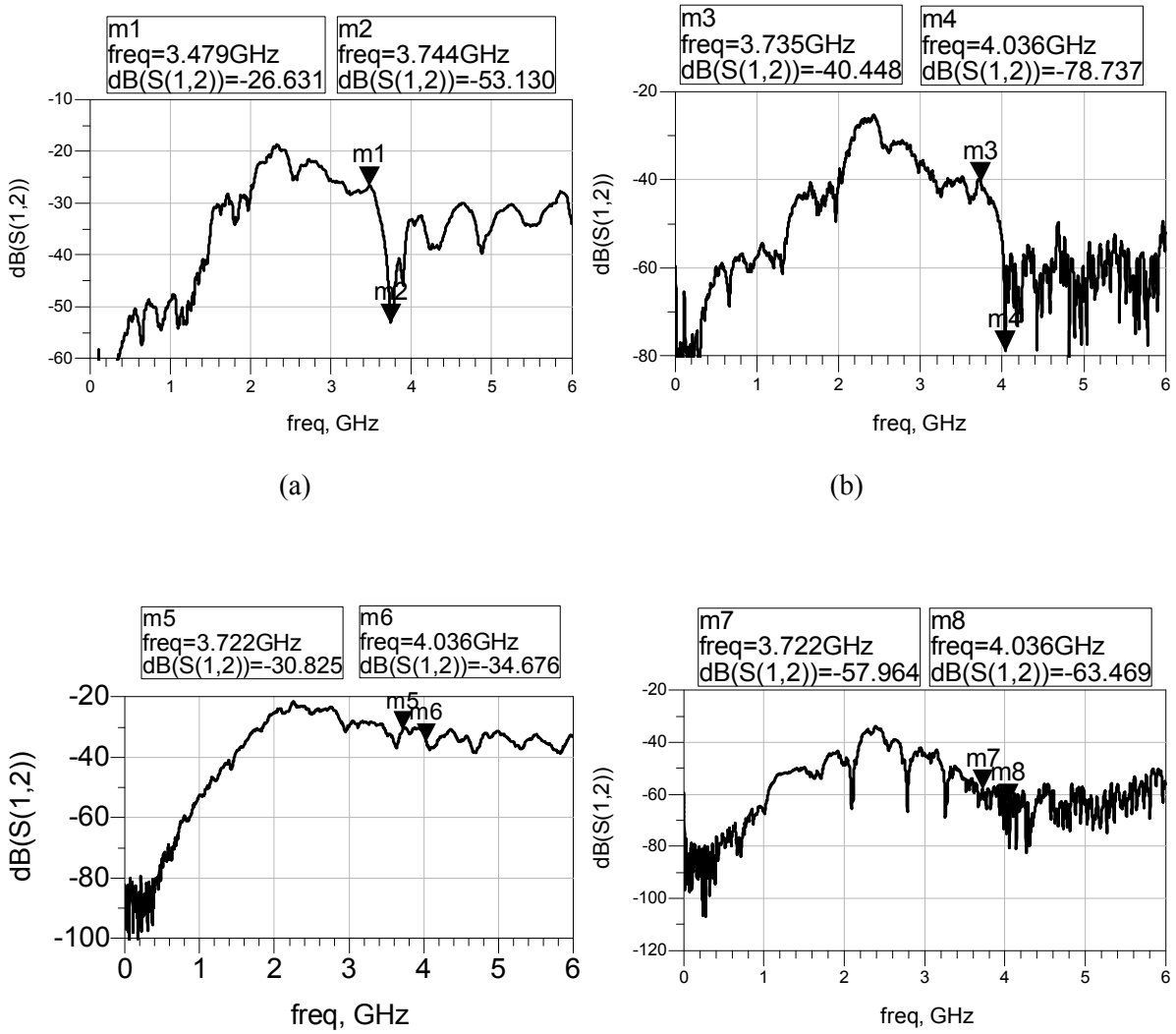


Fig. 3.14 (a) Transmission of TM wave on the EBG surface

(b) Transmission of TE wave on the EBG surface

(c) Transmission of TM wave on a smooth metal surface

(d) Transmission of TE wave on a metal surface

field travels a very short distance to the metal ground surface. For the same reason, when the metal surface is replaced by a mushroom-like EBG ground, the TM wave will tend to reduce the antenna input impedance. In order to achieve larger input impedance, the TM wave has to

be suppressed. Since the tangential electric field and normal magnetic field can't exist on a PEC plane, a very good metal plane has the nature to suppress a TE wave. When a dipole antenna is horizontally and closely placed above a PMC plane, only a tangential electric field and normal magnetic field can exist. The input impedance of the antenna will be nearly doubled due to the tangential electric field being almost doubled by the in-phase image. In order to boost the tangential electrical field and thus increase the antenna input impedance, a surface guiding TE wave is desired.

### 3.4.4 Design and verification of the low profile dipole antenna

Based on the results of the TE and TM wave measurements in Fig. 3.14 (a) and (b), a design frequency 3.722 GHz is chosen since it falls within the TM surface wave band gap but is located in the transmission band of the TE surface wave.

Two half-wave dipole antennas resonant at 3.722 GHz in free space were built. They were connected to the transmitting and receiving port of a network analyzer. The horizontal distance was 21 cm. The arms of the dipole antennas were positioned horizontally above a ground plane and parallel to each other. Based on scattering parameter measurements, the input impedance can be readily read from the $S_{22}$ plot; power gain between the two antennas was read by $S_{12}$ in dB when the antennas are perfectly matched. All of the following discussion about the S parameters measurements considers the design frequency 3.722GHz only. Fig. 3.15 (a) shows the S parameters when the two dipole antennas radiate in free space. For the two well matched dipole antennas with zero polarization loss, Friis transmission equation gives a power gain of approximately -26 dB. Our measured results

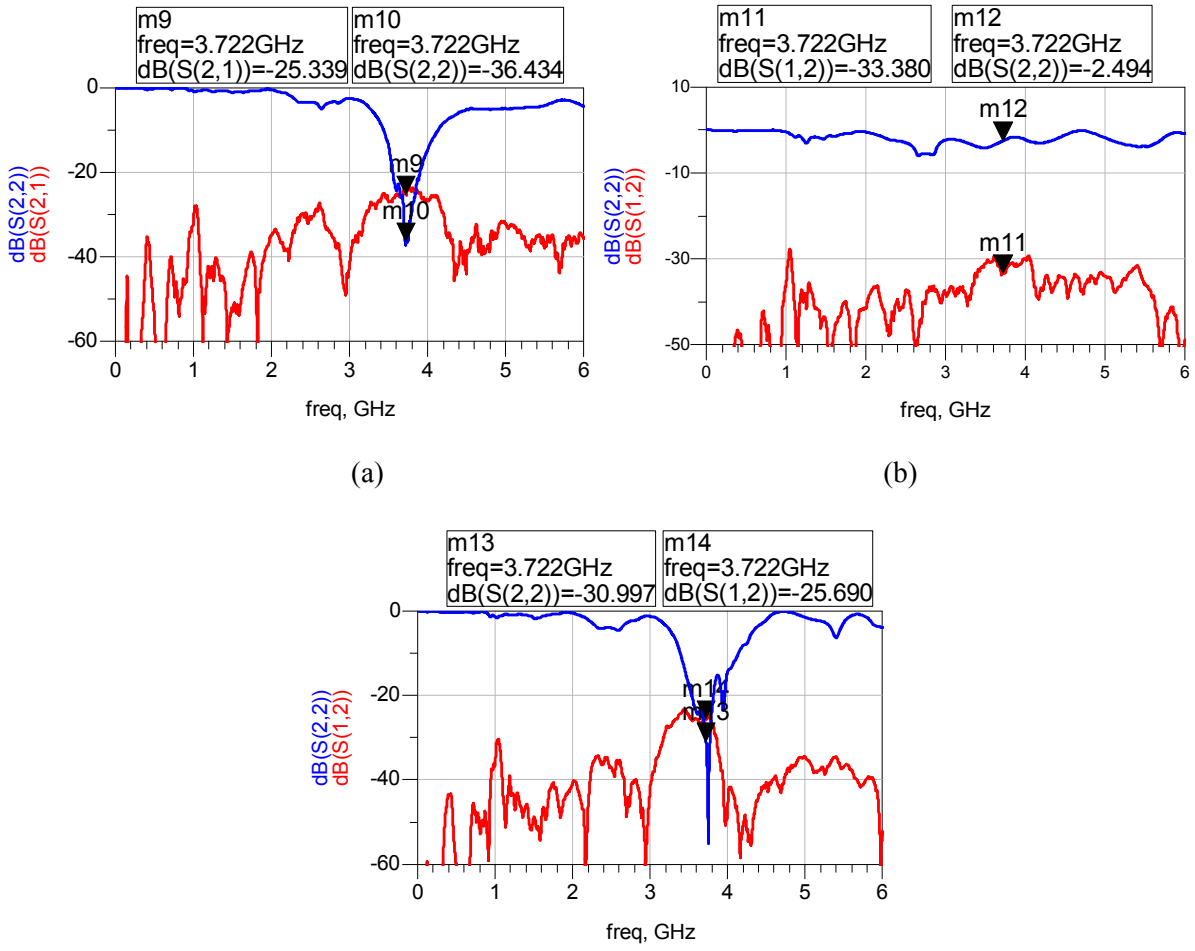


Fig. 3.15 (a) S parameters when dipoles are placed in free space

(b) S parameters when one metal plate is placed parallel to one dipole antenna with 0.5mm distance

(c) S parameters when the EBG surface is placed parallel to one dipole antenna with 0.5 mm distance

show when input reflection coefficient $S_{22}$ is -36 dB, the power gain $S_{12}$ reaches -25.3 dB, which agrees well with the calculated results. When a smooth copper sheet with the same size as the EBG surface is closely and horizontally (0.5 mm distance) placed above the dipole

antenna at port 2, the input impedance matching degrades dramatically from -36 dB to -2.5 dB, which means more than 56% of the power is reflected back to the source. Mismatch reduces the antenna radiation efficiency to 44% and the transmission coefficient to -29.6 dB if the antenna is assumed to be lossless. The measured data of transmission coefficient show -33.4 dB. The extra power loss likely comes from propagation of TM waves on the copper sheet. Once the cooper sheet is replaced by a mushroom-like EBG ground surface, the radiation efficiency of the dipole antenna recovers to the same level as in free space. The Smith chart displays the antenna input impedance of 50.1+j2.8 ohms, which corresponds to -31 dB if the magnitude of $S_{22}$ is plotted in dB. The transmission coefficient $S_{12}$ is -25.7 dB as in free space. The result confirms the effectiveness of applying the new design approach to the mushroom-like EBG ground surface.

## 3.5 A further exploration of the FSS and Mushroom-like EBG

### 3.5.1 Reflection phase

For the 9 by 9 square patch array made on FR4 board with a period of 19 mm, width 18 mm, gap 1 mm, dielectric thickness 1.5 mm and dielectric constant 4.17, the effective capacitance and equivalent inductance is 0.953 pF and 1.885 nH, respectively. The calculated reflection phase based on (3.10) is plotted in Fig. 3.16 with a solid line. The reflection phase of mushroom-like structure is plotted with circles in Fig. 3.16. The reflection phase of a FSS backed by the metal ground is plotted with a dashed line. It shows that the reflection phase profile doesn't depend on whether there are vias connecting the top metal patch to the bottom metal ground. With vias, the structure is a mushroom-like EBG surface. Without vias, the structure is a FSS backed by a metal ground. The reflection phase properties for both of them

have negligible difference. As we have discussed in the previous section, the calculated resonant frequency is a little bit larger than the more accurate results from HFSS simulation.

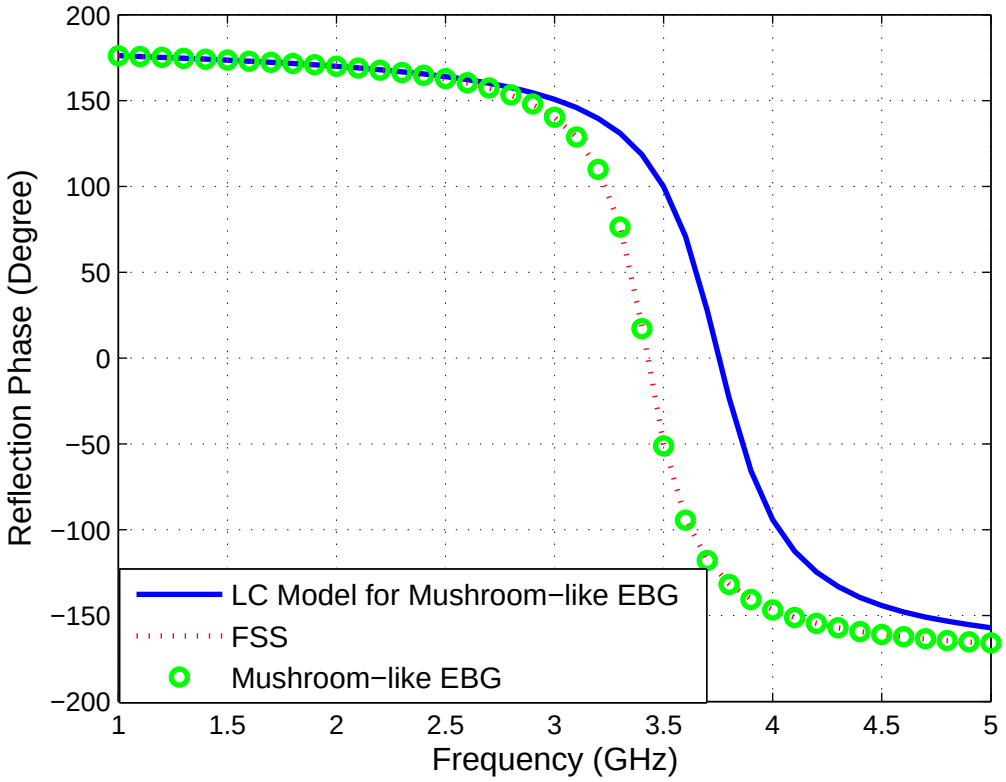


Fig. 3.16 Reflection phase above FSS and mushroom-like EBG surface

### 3.5.2 TM waves

**A. TM wave across the FSS and mushroom-like EBG surface**

Transmission properties of a TM wave across the EBG surfaces are illustrated in Fig.3.17. The solid line plots the transmission coefficient of a TM wave across the mushroom-like EBG surface. The solid line with "+" mark is the transmission coefficient of a TM wave across the FSS. The dash-dot curve shows the simulated transmission coefficient of a TM wave across the FSS computed by Ansoft HFSS V10 [10].

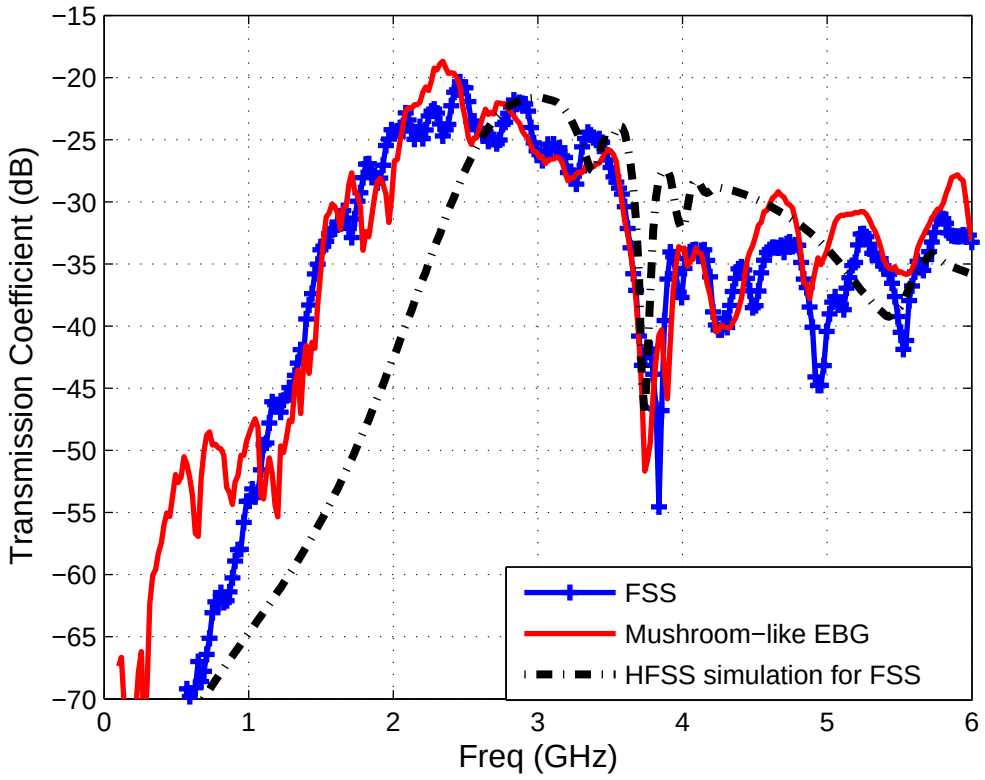


Fig. 3.17 Measured and HFSS simulated transmission coefficient of a TM wave across the FSS and mushroom-like EBG surface with a period of 19mm, width of metal patch 18 mm and thickness 1.5mm

Fig. 3.17 shows that both the FSS and mushroom-like EBG exhibit very similar transmission properties for a TM wave. The transmission of a TM wave drops clearly from -25 dB at 3.3GHz to below -50 dB at 3.8GHz, which shows the bandgap characteristics. The transmission coefficient of a TM wave across a 9 by 9 FSS array is derived by 3D HFSS simulation. All of the components for measurements including the board material with a 9 by 9 FSS, two monopole probes and metal ground are accurately modeled in HFSS V10 [10]. Due to the complicated geometry, large aspect ratio, unusual bandgap properties and wide frequency range, the simulated results have to be divided into several frequency bands in

order to generate meaningful results. From 0.122 GHz to 3.122 GHz, the simulated frequency step is set as 0.1 GHz due to the relatively smooth transition. From 3.122 GHz to 4.522 GHz, a 0.01 GHz frequency step is applied to reveal the bandgap properties. From 4.522 GHz to 5.922 GHz, a 0.1 GHz frequency step is used since the transition is smooth. The center frequency of the simulation is set to 3.722 GHz. The transmission property was computed for a total of 185 frequency points. With Ansoft HFSS V10 [10] and a Dell PC with 3.6 GHz CPU and 3.25GB memory, the overall simulation takes more than 40 hours. Fig. 3.17 shows a good agreement between simulation and measurements for this complicated EBG structure.

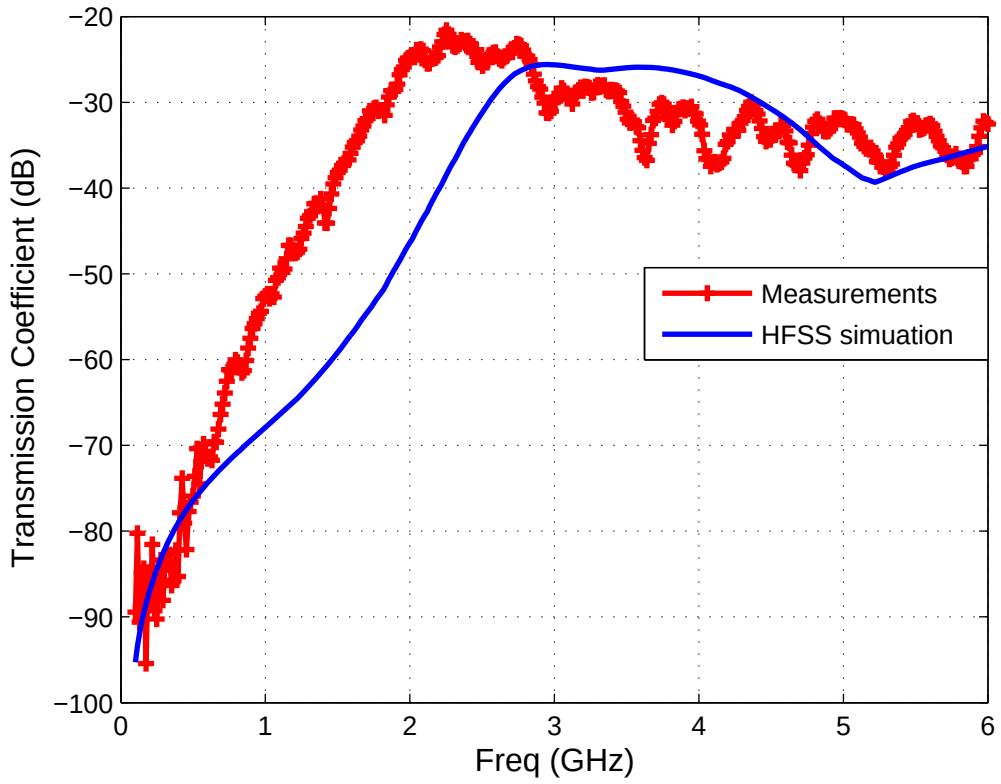


Fig. 3.18 Measured and simulated TM wave across a flat metal surface at the same size as the board for FSS

As a comparison, the transmission coefficient of a TM wave across a flat metal surface the same size as the FSS board is measured and plotted in Fig. 3.18. It is plotted with a solid line marked by "+" symbol. The simulated results given by HFSS are plotted with a solid line. It can be seen that from 3 to 5 GHz, the transmission coefficient is relatively flat, which shows a smooth metal surface (inductive) is capable of guiding a TM wave.

**B. A circuit model for a TM wave across the EBG surface**

The surface impedance for a TM surface wave can be written as [31],

$$Z_s^{TM} = \frac{j\alpha}{\omega\varepsilon} \tag{3.18}$$

where $\alpha$ is the decay constant. It shows that a TM surface wave should be supported by an inductive surface, for example, a smooth metal plane. Fig. 3.18 is an example of an inductive surface that supports the TM wave including the TM surface wave.

When a TEM plane wave is normally incident on an EBG surface, the equivalent circuit of the EBG surface is described as a parallel LC resonator as shown in Fig. 3.4.

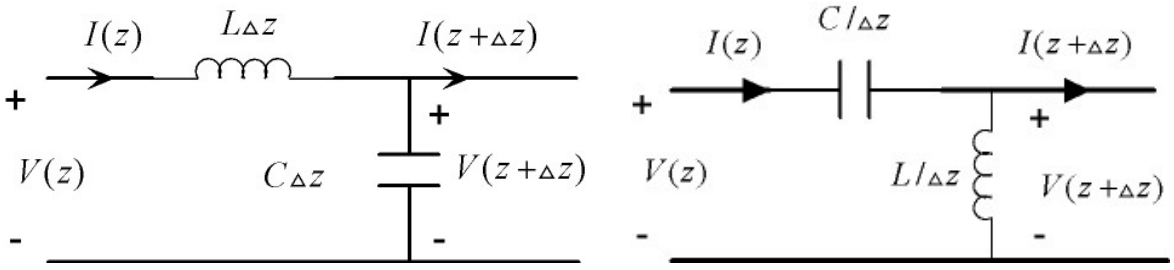


Fig. 3.19 (a) Forward transmission line LC model (b) Backward transmission line CL model

When a TM wave is launched onto a lossless microstrip transmission line [20], the excited

electromagnetic wave will propagate along the metal surface, and is associated with a surface current. For this case, a distributed LC equivalent circuit model as shown in Fig. 3.19 (a) is named as a forward transmission line (TL).

Similarly, when a TM wave is launched onto an EBG surface, a surface current will be excited and propagate along the surface. A dual CL equivalent circuit is shown in Fig. 3.19 (b), to model the transmission of a surface current across the EBG surface [32]. It is designated as a backward transmission line (TL) [33].

For a forward transmission line shown in Fig. 3.19 (a), and considering the time harmonic case, the equations can be easily derived by Kirchhoff's voltage law (KVL) and Kirchhoff's current law (KCL),

$$\frac{dV(z)}{dz} = -j\omega LI(z) \tag{3.19}$$

$$\frac{dI(z)}{dz} = -j\omega CV(z) \tag{3.20}$$

As the dual of the forward transmission line, the backward transmission line [33] in Fig. 3.19 (b) obeys the following equations,

$$\frac{dV(z)}{dz} = -\frac{1}{j\omega C}I(z) \tag{3.21}$$

$$\frac{dI(z)}{dz} = -\frac{1}{j\omega L}V(z) \tag{3.22}$$

$$\frac{d^2V(z)}{dz^2} = \frac{1}{j\omega C}\frac{1}{j\omega L}V(z) = \gamma^2 V(z) \tag{3.23}$$

$$\gamma = j\beta = \sqrt{\frac{1}{j\omega C}\frac{1}{j\omega L}} = -\frac{j}{\omega\sqrt{LC}} \tag{3.24}$$

$$v_p = \frac{\omega}{\beta} = -\omega^2\sqrt{LC} \tag{3.25}$$

$$v_g = \frac{d\omega}{d\beta} = \omega^2\sqrt{LC} \tag{3.26}$$

For an x polarized plane wave propagating in the z direction in a lossless and source-free region, the governing first order wave equations are written as,

$$\frac{dE_x(z)}{dz} = -j\omega\mu H_y(z) \tag{3.27}$$

$$\frac{dH_y(z)}{dz} = -j\omega\varepsilon E_x(z) \tag{3.28}$$

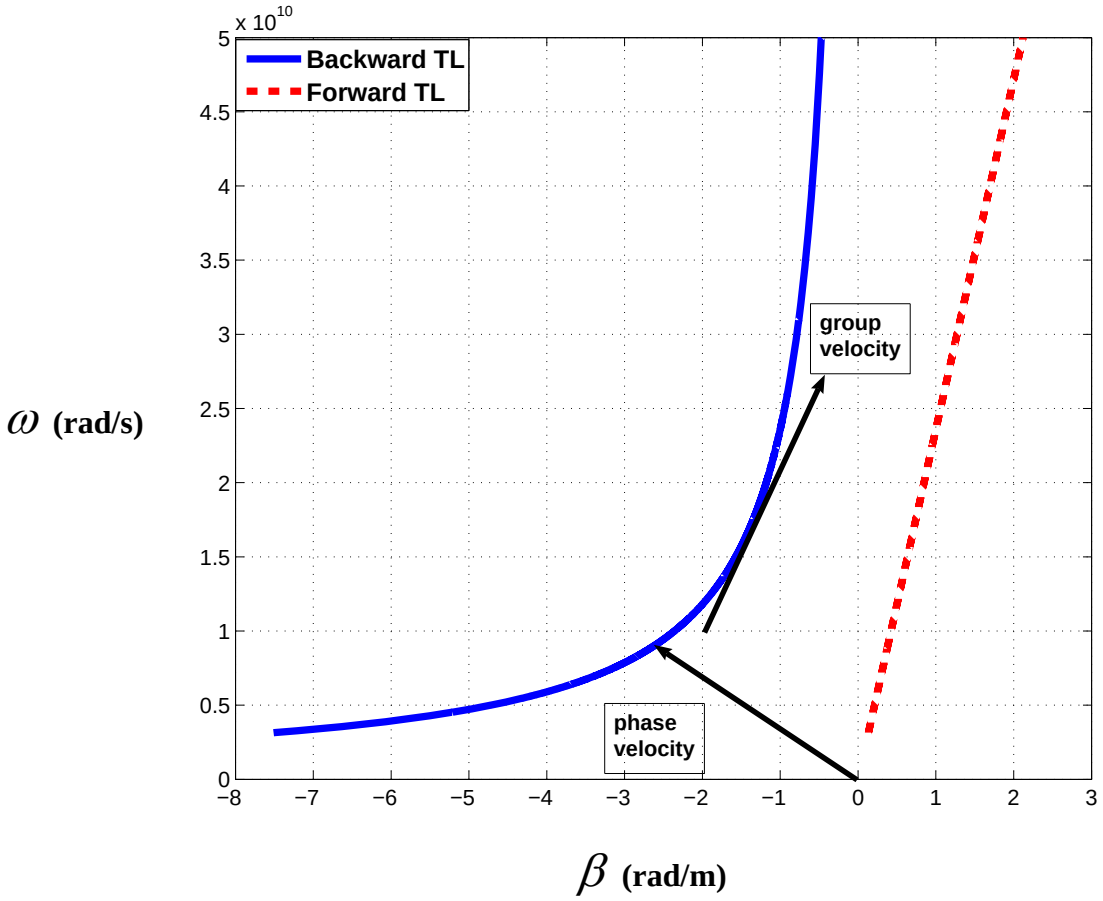


Fig. 3.20 Phase velocity and group velocity of backward and forward transmission lines

For the backward wave transmission line, as compared to the plane wave case, the equivalent permeability and permittivity are negative.

$$\mu = -\frac{1}{\omega^2 C} \qquad \varepsilon = -\frac{1}{\omega^2 L} \tag{3.29}$$

As shown in Fig. 3.20, the phase velocity and group velocity for a backward transmission line have opposite signs. For a forward transmission line, they have the same signs.

A common forward transmission line has a series L and a shunt C. The shunt C is not able to hold the charge in the unit cell since the charge can be readily discharged to the next LC unit cell. However, a unit cell in a backward transmission line has a series C and a shunt L. The series C is in the center of the unit cell and when C discharges, the electric energy will be transformed into magnetic energy inside the unit cell. This is the essential difference between a backward transmission line and forward transmission line. The distinct property of the backward transmission makes a parallel resonator possible.

A well-known equivalent circuit model considering the parasitic capacitance and inductance [32] is redrawn in Fig. 3.21. $C_g$ represents the gap capacitance between metal patches. $L_s$ represents the parasitic serial inductance. $L_p$ represents the equivalent parallel inductance to

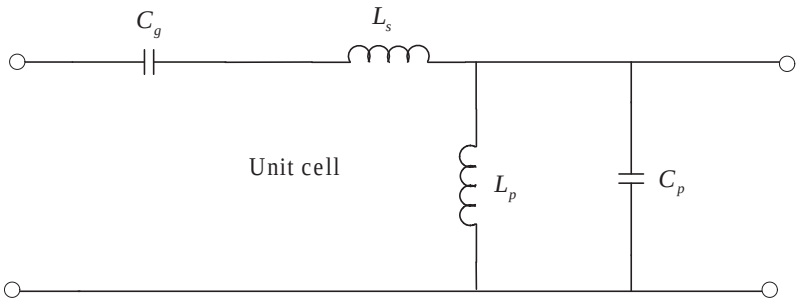


Fig. 3.21 Equivalent circuits for TM wave across the FSS or Mushroom-like EBG [32]

ground. $C_p$ represents the parasitic parallel capacitance. Based on the distributed circuit model, the bandgap frequency band can be found from the $\omega - \beta$ diagram [32]. If the parasitic capacitance and inductance are ignored, the equivalent circuit model includes series capacitance and parallel inductance, as we have discussed before, which represents a backward transmission line.

### 3.5.3 TE waves

**A. TE wave across the FSS and mushroom-like EBG surface**

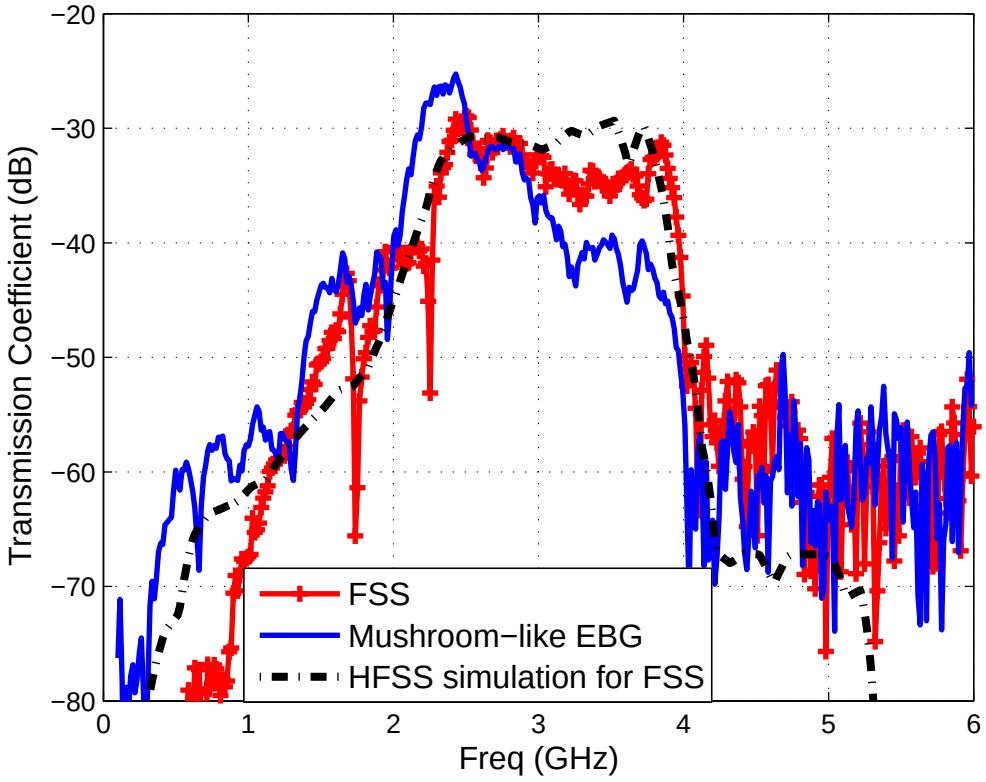


Fig. 3.22 Measured and HFSS simulated transmission coefficient of a TE wave across the FSS and mushroom-like EBG surface with a period of 19mm, width of metal patch 18 mm and thickness 1.5mm

The measured and simulated transmission coefficients of a TE wave across the FSS and mushroom-like EBG surface are shown in Fig. 3.22. The solid line represents the transmission coefficient of a TE wave across a mushroom-like EBG surface. The solid line marked by "+" is the transmission coefficient of a TE wave across the FSS. The dash-dot line is the simulated results of a TE wave across the FSS computed by 3D HFSS V10 [10]. It's shown that the transmission of TE waves maintain at a relatively flat level from 2.5 GHz to 3.85 GHz. However, after 3.9 GHz, the transmission coefficients drop and never rises up again, which shows that the TE wave is unable to be supported by the EBG surfaces above that frequency. The FSS array and mushroom-like EBG surface demonstrate similar TE wave properties, which agree well with the 3D HFSS simulation. Different from a TM case, there are no observed bandgap regions for TE waves.

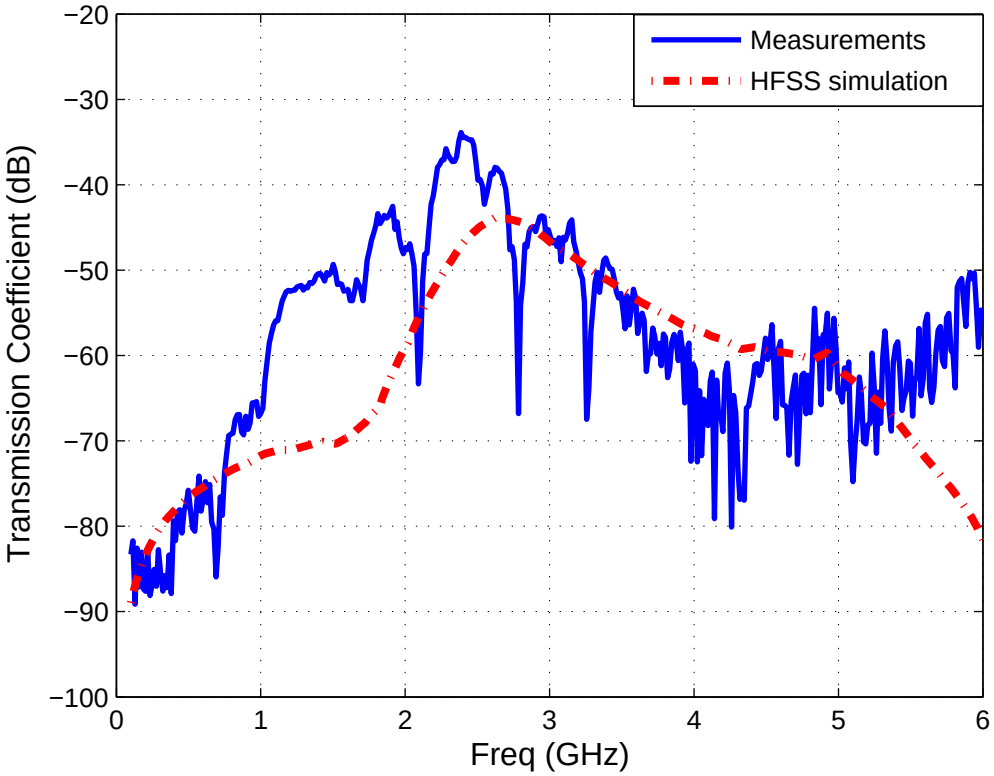


Fig. 3.23 Measured and simulated TE wave across a flat metal surface

The transmission properties of a TE wave across a metal surface are plotted in Fig. 3.23. The solid line represents the measured transmission coefficient. The dash-dot is the simulated results computed by HFSS. It's clear that the metal surface is not able to support the propagation of TE wave.

**B. A circuit model for a TE wave across the EBG surface**

The surface impedance for a TE surface wave can be written as [31],

$$Z_s^{TE} = \frac{-j\omega\mu}{\alpha} \tag{3.30}$$

When a TE surface wave is launched at the interface, a necessary condition for its existence and propagation is that the surface impedance is capacitive. If the surface impedance is inductive such as a smooth metal surface, the TE surface wave will be suppressed, which can be seen from Fig. 3.23. It can be understood since a TE wave includes a tangential electric field and vertical magnetic field but a smooth metal surface supports a normal electric field and tangential magnetic field, therefore the smooth metal surface would suppress a TE wave in nature. To sustain a tangential electric field and vertical magnetic field for the TE case, it requires the surface current to be formed into a loop on the surface. As shown in Fig. 3.24, when the TE wave propagates in the positive z direction along a FSS or mushroom like EBG, the gap capacitance between two patches will allow the existence of the tangential electric field. The loop currents generate vertical magnetic fields. The opposite currents in the two loops will cancel each other and create a net equivalent current or E field along the y direction. For the TE wave, since only tangential electric field exists, there is no direct coupling between the top metal patches and bottom metal ground.

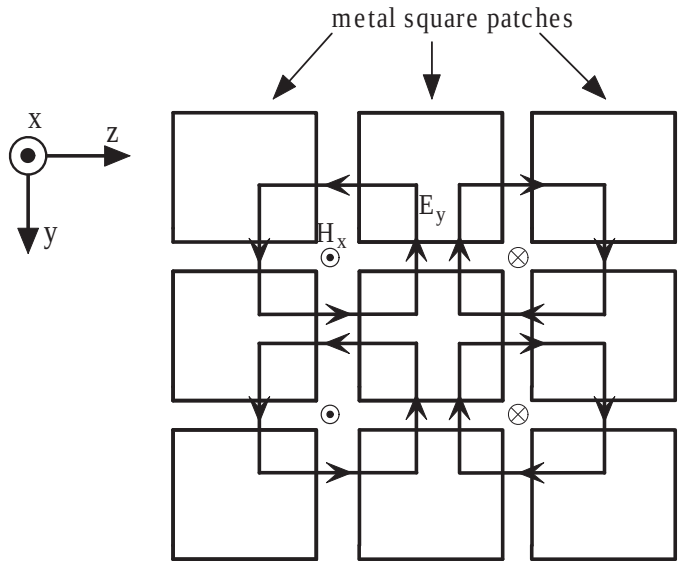


Fig. 3.24 Surface current due to TE wave on the EBG surface

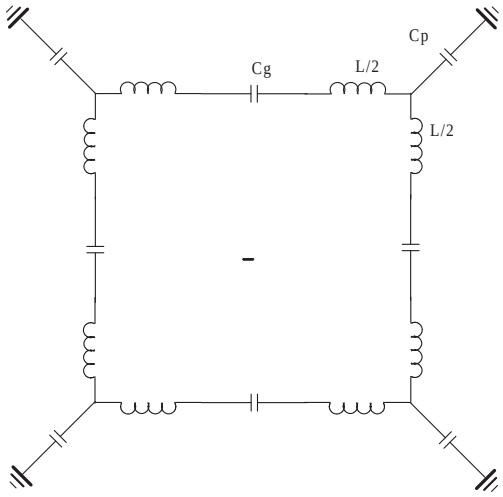


Fig. 3.25 The equivalent LC circuit model for the TE wave across the EBG surface

As shown in Fig. 3.25, for a TE wave across the EBG surface, the equivalent circuit of serial LC circuits connected in a loop is originally proposed here. A split ring resonator has

been broadly studied in [34] [35]. From the series LC equivalent circuit, it can be seen that the FSS backed by metal ground or mushroom-like EBG surface is similar to the split ring resonator. The capacitor C represents the gap capacitance between metal patches. The inductor L represents the loop inductance. The current flows in a loop on the surface for the TE case, which is different from the TM case where the current flows in the backward TL. When loss is included, a series RLC circuit connected in a loop should be applied to represent the TE wave across the EBG surface. The L and C values for both TE and TM waves are the same.

As we have known, for a series LC resonator, at low frequency, the impedance is capacitive. Above the series resonant frequency, the impedance is inductive. From (2.30), a TE surface wave requires a capacitive surface impedance. Therefore a TE surface wave will be supported at a lower frequency range but suppressed at higher frequency. This conclusion is applied to the surface currents excited by all of the TE modes in agreement with the measured and simulated data shown in Fig. 3.26.

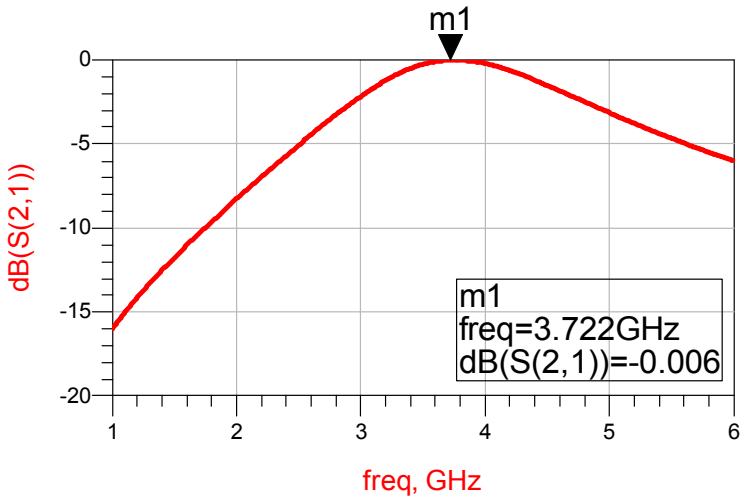


Fig. 3.26 The calculated $S_{21}$ for a unit cell on TE wave across the EBG surface

Based on the previous calculation, Cg = 0.95 pF, L = 1.89 nH. The simulated transmission coefficient of 4 unit cells based on the LC parameters is plotted in Fig. 3.26 which shows a similar propagation property as the measured TE case. A series resistor R coming from the metal surface impedance equal to 0.016 ohms is included here.

## 3.6 Hilbert curve

A Hilbert curve has the theoretically infinite length in any finite area. Fig. 3.27 shows a fifth order Hilbert curve [36].

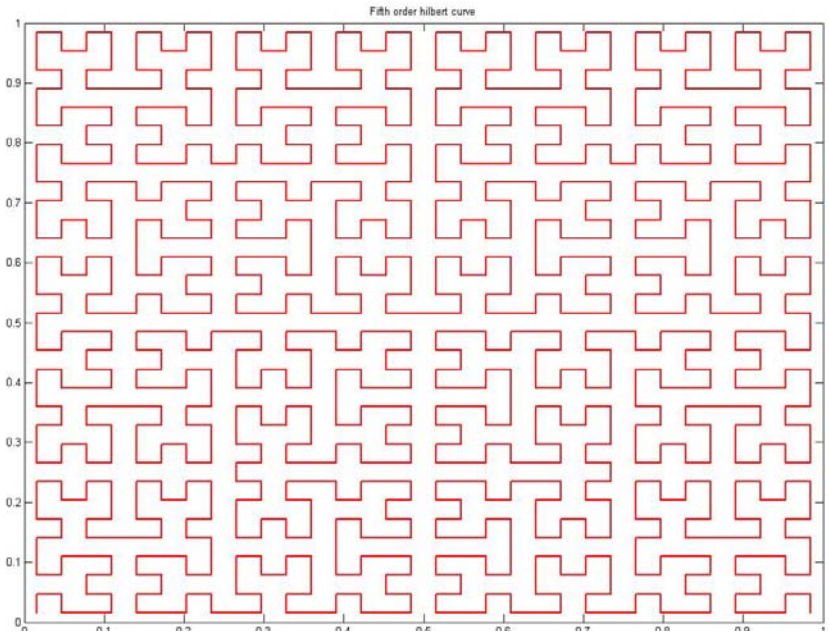


Fig. 3.27 Fifth order Hilbert curve

For a metal trace, a longer length and thinner width means a larger inductance. It is also one type of metamaterial and demonstrates electromagnetic bandgap (EBG) properties [37]. For a

unit cell, if the inductance increases, with the same capacitance, the resonant frequency of the structure should be decreased [37]. The Hilbert curve is promising to reduce the size of the overall EBG material, however, due to the complexity of manufacture, further study was not conducted.

# CHAPTER 4

# METAL-SURFACE MOUNTED RFID TRANSPONDER

## 4.1 Introduction

In Chapter 3, the metamaterial has been demonstrated to be able to recover the radiation efficiency of dipole antennas horizontally mounted above metal surface. It is easy to be built by using the modern printed circuit board technique and integrate it with the RFID tag antenna. A major disadvantage for this approach is the relatively large area which is required by the metal material. For a very low profile design, each unit cell has dimension around a quarter wavelength. Even with a high dielectric material, an EBG material with a 9 by 9 array still occupies a large area, which is not desirable for the RFID industry. A good low-loss dielectric material such as Rogers' material is relatively expensive. A superior approach is to change the antenna structure so that the antenna is able to radiate efficiently above a metal surface. The antenna of a RFID transponder should have an omnidirectional radiation pattern, high directivity and high radiation efficiency. The omnidirectional radiation pattern is important since we want any object attached by a RFID transponder to be recognized no matter where it is placed at a certain distance. As we have shown in Chapter 3, a higher directivity and higher efficiency corresponds to a larger reading/writing range. The overall geometry of the antenna should be as small as possible. A relatively small thickness is more important relative to the horizontal geometry. To make the design practical and low cost, the antenna design should have a simple geometric shape and adopt inexpensive material. In one word, the antennas for RFID transponders should have superior performance, low profile,

compact size and low cost. The commonly used dipole antenna obviously is a good candidate even though it has a relatively small directivity. However, it is unable to work horizontally above a metal surface.

We invented two major types of planar antennas for metal-surface mounted RFID transponders that meet the above requirements. One type of antenna has an inverted-L shape, which is a compact and low profile design. The other type of antenna is a slotted planar antenna design, which has a very high gain and longer reading range (> 10 m). Both of them are in the process of patent application and licensing [38] [39].

## 4.2 A low profile metal-surface mounted RFID transponder antenna with a slotted inverted-L shape

### 4.2.1 Introduction

This invention proposes a high efficiency metal-surface mounted radio frequency identification (RFID) tag antenna which is operated in the ultra high frequency (UHF) band. This antenna has a slotted inverted-L shape. It has a compact size (1.3 inches by 2.6 inches), low profile (32 mils or 64 mils) and excellent reading range. The antenna is built on foam with 64 mils thickness and was tested with a Symbol RFID handheld reader (MC9000-G) with 4W EIRP. The reading range is more than 20 feet. Commercially, the radiation patch and ground patch can be easily built on one thin layer by using an inexpensive silver printing process. The final antenna is built by folding the printed metal layer around an inexpensive foam substrate, which demonstrates that it has a very low fabrication cost. By simulation using a 3D electromagnetic simulation software HFSS, the antenna shows a 58% radiation

efficiency above 64 mils thick foam. It also exhibits an omnidirectional radiation pattern, which shows a directivity of 3 to 4 dBi in all of the elevation planes. Based on a 2:1 VSWR bandwidth standard, the proposed antenna has a bandwidth of 30 MHz, which is broader than the desired Industrial, Scientific and Medical (ISM) frequency band (902 ~ 928 MHz).

### 4.2.2 Structure and performance of a slotted inverted-L antenna

The geometry of the proposed RFID tag antennas is shown in Fig. 4.1 to Fig. 4.4. Fig. 4.1 (a) and (b) illustrates the plan view and cross section view of the antenna. It is designed using a thin foam layer. The substrate thickness is variable. If the thickness is increased, the radiation efficiency would increase proportionally. The biggest challenge for a metal surface mounted antenna is to maintain a very low profile but at the same time to achieve a very good radiation efficiency. For this design, a 64 mils (1.6 mm) thick foam layer with a dielectric constant of 1.2 and tangent loss of 0.001 is used as the substrate. The antenna is folded through the dotted line. Thus the overall horizontal size is about 2.6 inch by 1.3 inch. The radiation patch and ground patch is built on a 1.4 mil copper layer. The commercial Symbol RFID handheld reader (MC9000-G) with a 4W EIRP was applied to test the performance of the antenna above a 5 inch by 6 inch copper board. The maximum reading range at a horizontal direction is more than 20 feet (6 meters) which is good for most of the applications. If a higher reading range is desired, the patch size, slotted area and thickness can be adjusted. For this antenna structure, a bigger area and higher substrate height contribute to a larger directivity and radiation efficiency. Overall, a larger reading distance can be achieved. If a smaller or thinner structure is desired, the size and height can be decreased by trading with the reading range. With a 32 mils thick substrate and the same

horizontal size, a reading range of 10 feet is achieved. By changing the width and length of the slotted air gap, the RFID tag antenna impedance can be varied and matched to the RFID chip impedance. No extra impedance matching elements are required.

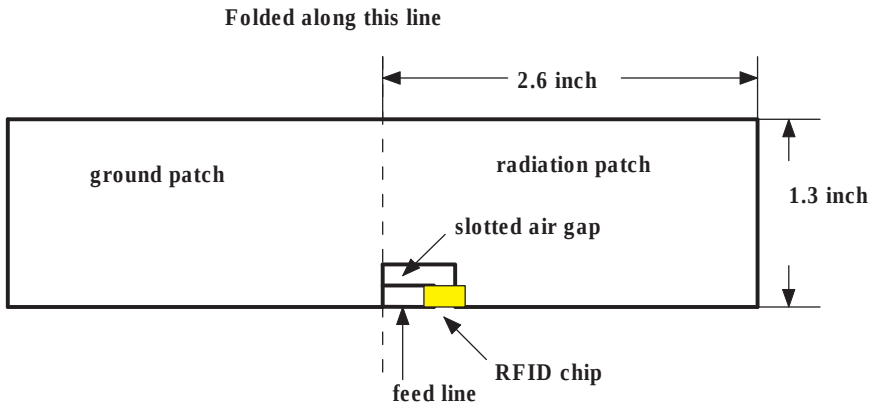


Fig. 4.1 (a) Plan view of a slotted inverted-L RFID antenna built on foam

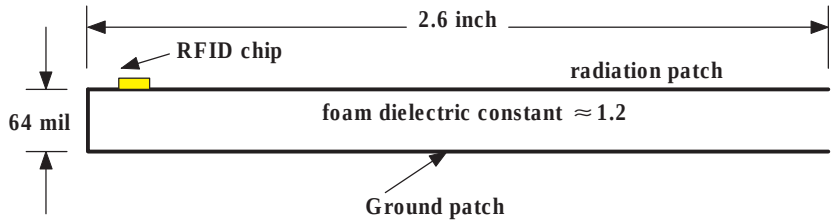


Fig. 4.1 (b) Cross section view of the slotted inverted-L RFID antenna built on foam

Fig. 4.2 demonstrates a variation of the slotted inverted-L RFID tag antenna, which is folded along a line which is a little farther from the edge of the slotted gap. The microstrip lines connected to the RFID chip are extended from the main body of the radiation patch. This structure may have a better reliability for manufacturing.

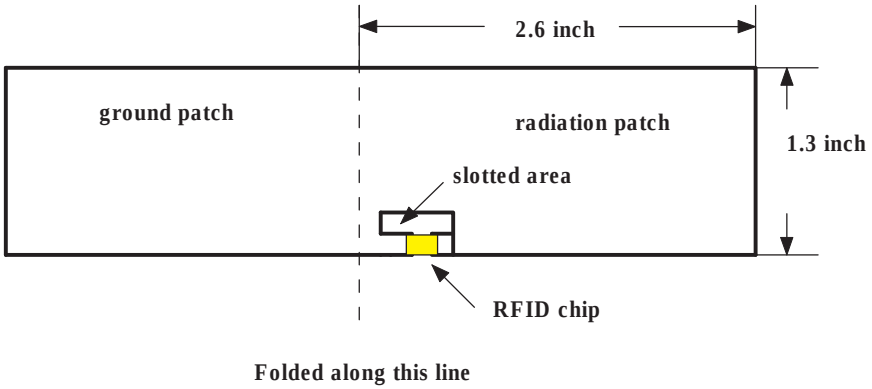


Fig. 4.2 Plan view of a slight different slotted inverted-L RFID antenna built on foam

Fig.4.3 (a) and (b) demonstrates the structure built on RT/DUROID® R 5880. The dielectric constant is 2.2 and tangent loss is 0.0009. The horizontal size for a similar performance (20 feet reading range) is smaller, about 2 inches by 1.2 inch. The thickness is 62 mils.

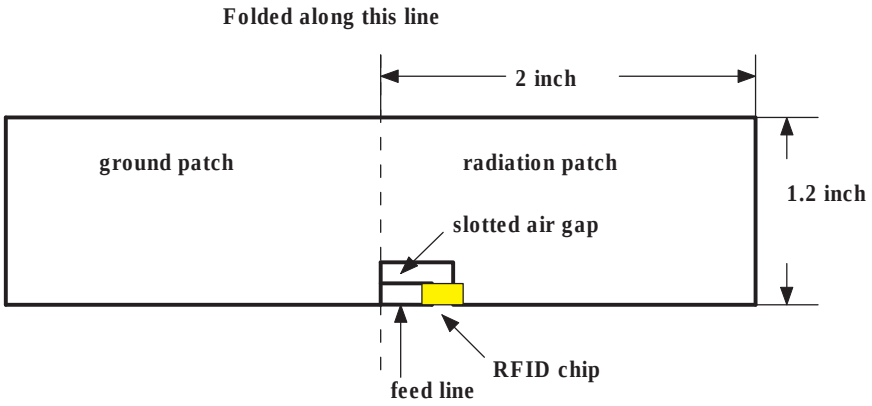


Fig. 4.3 (a) Plan view of a slotted inverted-L RFID antenna using RT/DUROID® R 5880

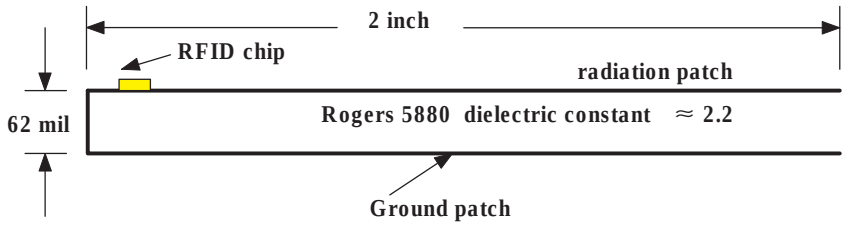


Fib. 4.3 (b) Cross section view of the slotted inverted-L RFID antenna using RT/DUROID® R 5880

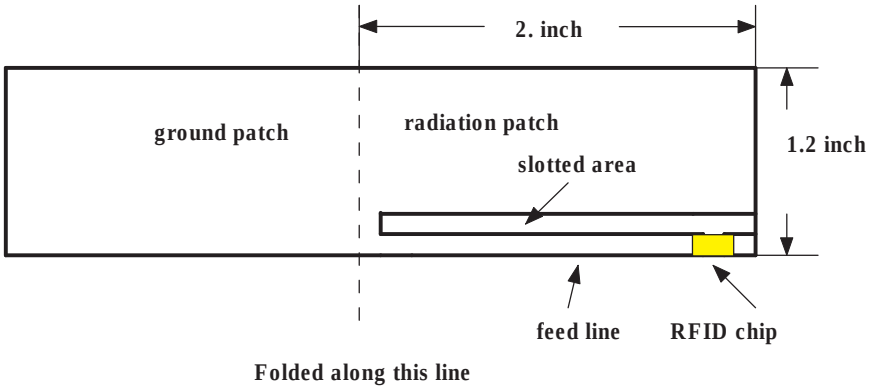


Fig. 4.4 Plan view of a slotted inverted-L RFID antenna with a longer slot using RT/DUROID® R 5880

Fig. 4.4 shows another variation of the slotted inverted-L RFID tag with a longer slot on the radiation patch.

By using a silver printing process, the radiation patch and ground patch can easily be built on one thin layer. Then a folding process can be applied to fold the structure onto a dielectric substrate (foam or other material). Foam is one of the most inexpensive substrates available in the market. Silver silk screen printing is a mature and inexpensive technology in industry. Therefore the overall cost per unit can be as low as \$0.2, which is much lower than the commercially available \$4~\$6 RFID tag. Currently the best known commercially metal surface mounted RFID tag provided by Metalcraft I.D. Plates and Labels is about 1 inch wide, 5.8 inch long and 200 mil thickness. The reading range is about 12 feet. Its overall size is 5.4 times bigger than our invention made of foam.

### 4.2.3 Prototypes and test

A few prototypes were built on inexpensive foam and RT/ DUROID® R 5880. The antenna shown in Fig. 4.5 (a) is built on foam and is 2.6 inch long, 1.3 inch wide and 0.064 inch thick. The antenna shown in Fig. 4.5 (b) is 2 inch long, 1.2 inch wide and 0.062 inch thick.

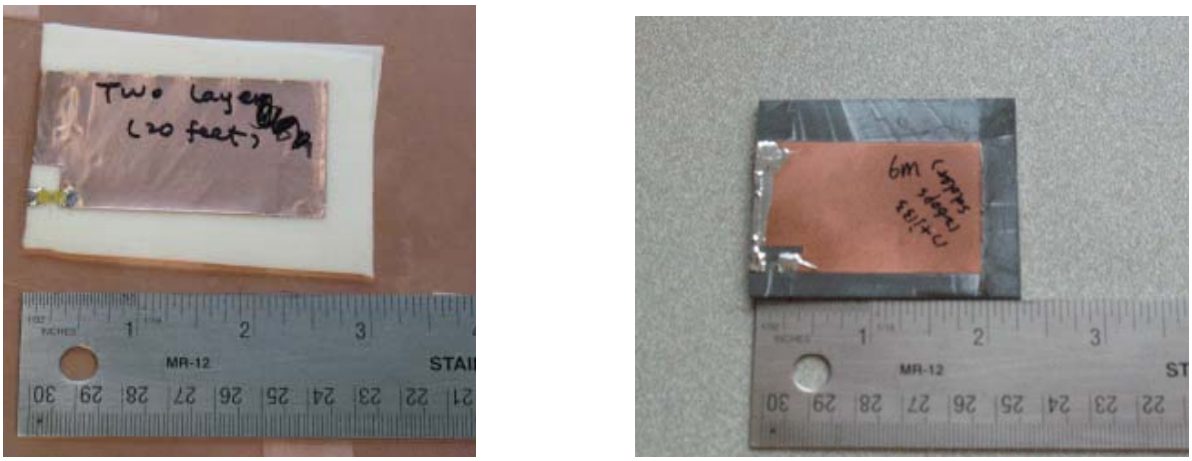

(a) (b)

Fig. 4.5 (a) The prototype of a slotted inverted-L UHF RFID tag built on foam

(b) The prototype of a slotted inverted-L UHF RFID tag built on RT/ DUROID® R 5880

When an antenna, as shown in Fig. 4.5 (a) with a thicker foam structure (64 mil thickness, 2.6 inch by 1.3 inch horizontal size), is placed above a large metal ground surface, the radiation efficiency simulated by HFSS is 58%. The directivity is 2.6, which is almost two times as large as a common dipole type RFID tag antenna. Table 4.1 shows the simulated results of the inverted-L antenna with different thicknesses, which shows the antenna impedance is not very sensitive to the thickness of the substrate for this structure.

Table 4.1 The simulated results for the slotted inverted-L antenna built on foam

| | Length (inch) | Width (inch) | Height (inch) | Directivity | Efficiency | Antenna Impedance (ohm) |
|---|---|---|---|---|---|---|
| Thicker foam | 2.6 | 1.3 | 0.064 | 2.6 | 0.58 | 8+j85 |
| Thinner foam | 2.6 | 1.3 | 0.032 | 2.6 | 0.28 | 13+j80 |

For the inverted-L antenna shown in Fig. 4.5 (a), the antenna input resistance, reactance and VSWR in the ISM frequency band is plotted in Fig. 4.6 (a), (b) and (c), respectively. The VSWR in the whole frequency band is less than 1.8. In the region of 915 MHz, the VSWR is less than 1.2. A good impedance matching is achieved.

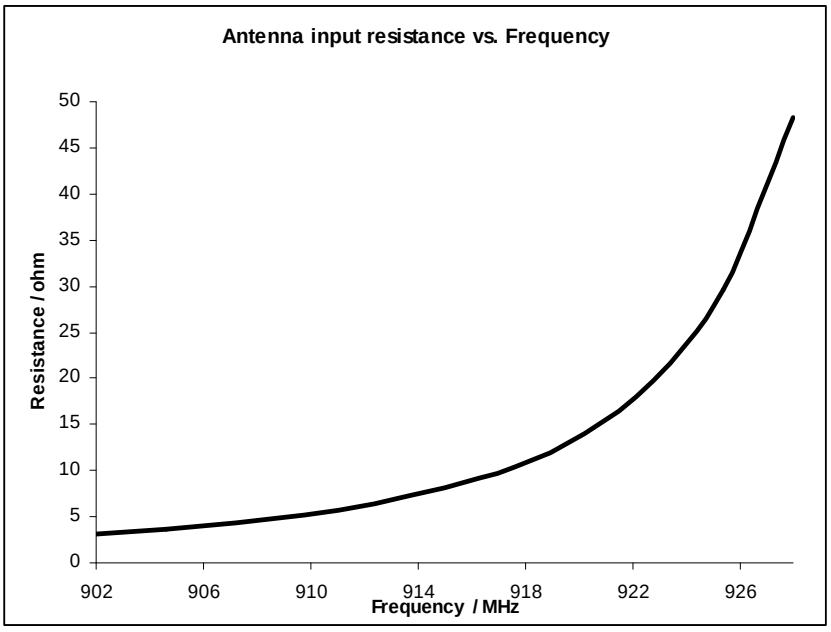


Fig. 4.6 (a) Simulated input resistance of the inverted-L antenna (with length 2.6 inch, width 1.3 inch and thickness 64 mils) as a function of frequency in the ISM frequency band

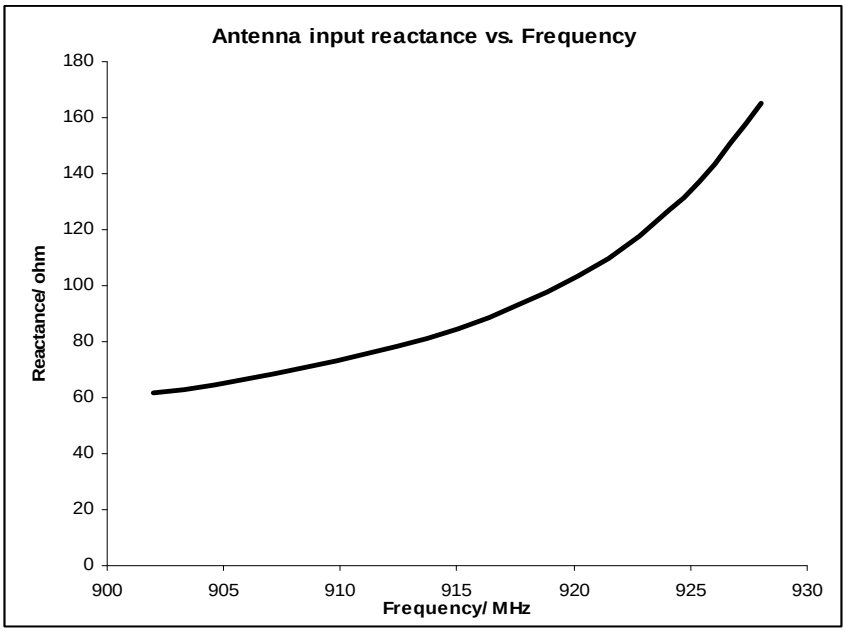


Fig. 4.6 (b) Simulated input reactance of the inverted-L antenna (with length 2.6 inch, width 1.3 inch and thickness 64 mils) as a function of frequency in the ISM frequency band

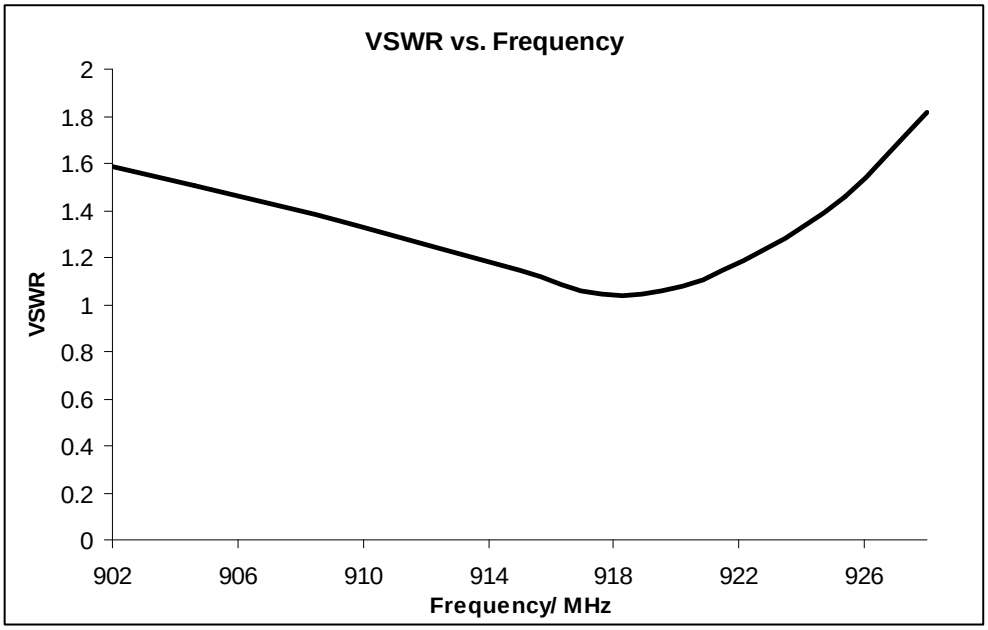


Fig. 4.6 (c) Simulated VSWR of the inverted-L antenna (with length 2.6 inch, width 1.3 inch and thickness 64 mils) as a function of frequency in the ISM frequency band

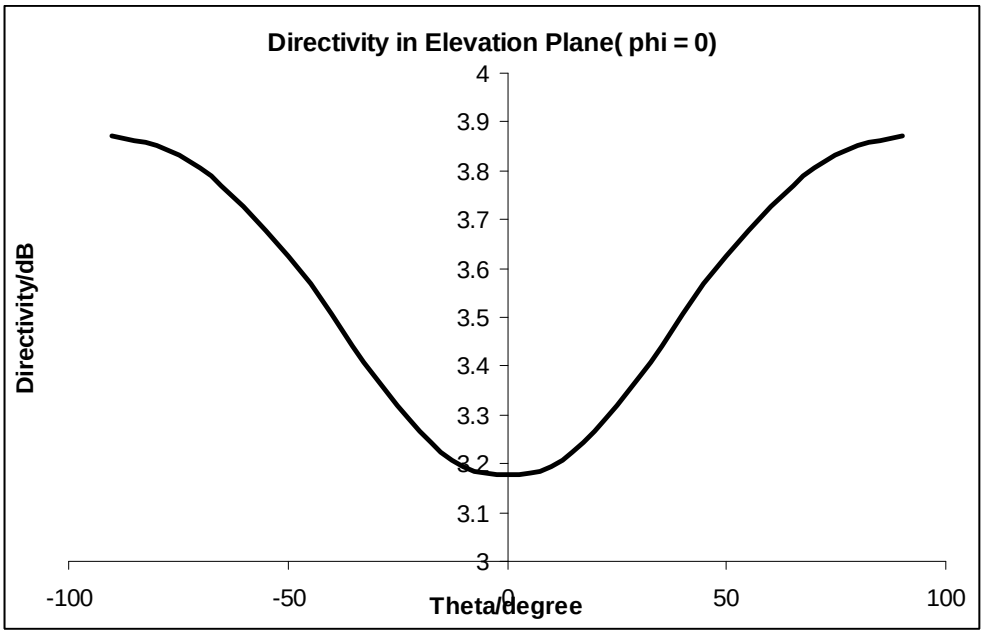


Fig. 4.7 (a) Simulated directivity pattern of the inverted-L antenna (with length 2.6 inch, width 1.3 inch and thickness 64 mils) in elevation plane (phi = 0 degree)

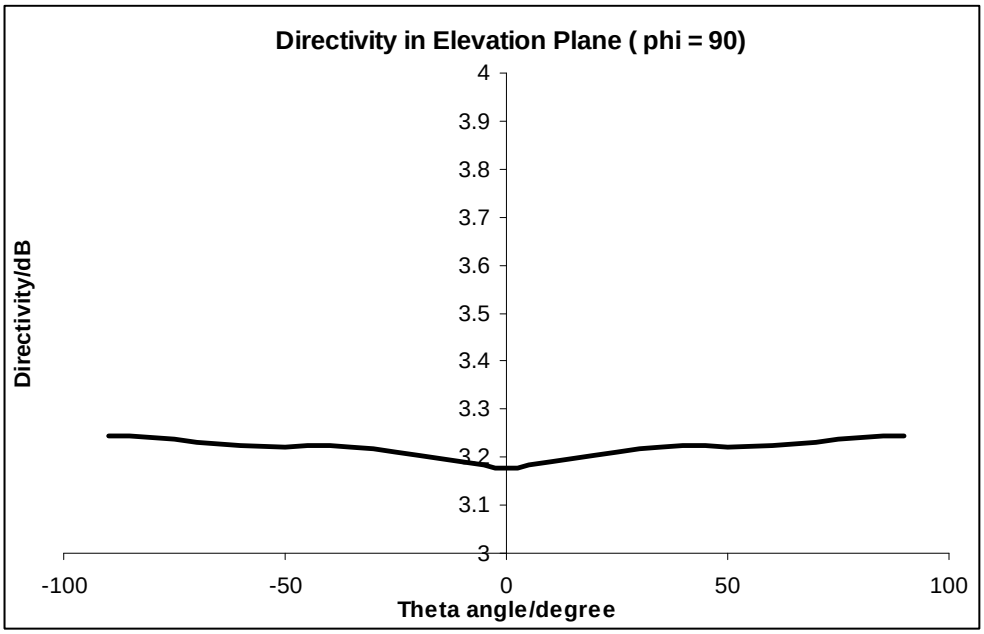


Fig. 4.7 (b) Simulated directivity pattern of the inverted-L antenna (with length 2.6 inch, width 1.3 inch and thickness 64 mils) in elevation plane (phi = 90 degree)

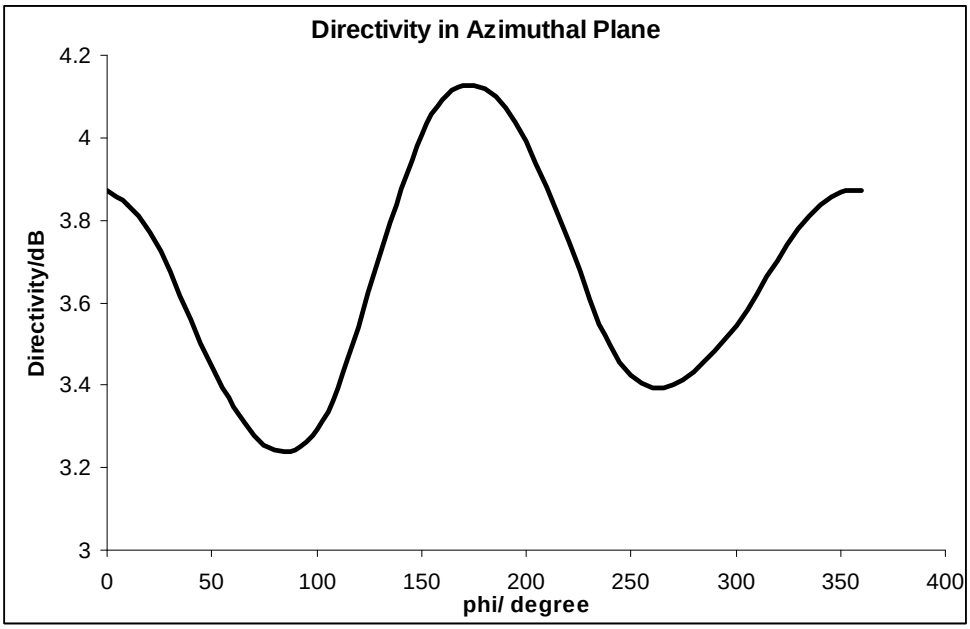


Fig. 4.7 (c) Simulated directivity pattern of the inverted-L antenna (with length 2.6 inch, width 1.3 inch and thickness 64 mils) in azimuthal plane (theta = 90 degree)

Fig. 4.7 (a) shows that the directivity in the elevation plane (phi = 0 degree) varies from 3.3 dBi to 3.9 dBi. Fig. 4.7 (b) shows that the directivity varies from 3.2 dBi to 3.3 dBi in the elevation plane (phi = 90 degree). Fig. 4.7 (c) shows that the directivity varies from 3.2 dBi to 4.2 dBi in the azimuthal plane. The 2D directivity plots illustrate that the inverted-L antenna has an approximately omnidirectional radiation pattern with directivity bigger than 3.2 dBi, which is a significant value for RFID transponder antenna. When the RFID tag antenna is attached to a large metal surface, from 0 to 180 degree, the RFID tag should be able to be read at almost equal distance.

A 3D directivity pattern is plotted in Fig. 4.8, which further supports the conclusion that the directivity varies from 3.2 dBi to 4.16 dBi everywhere above the ground plane.

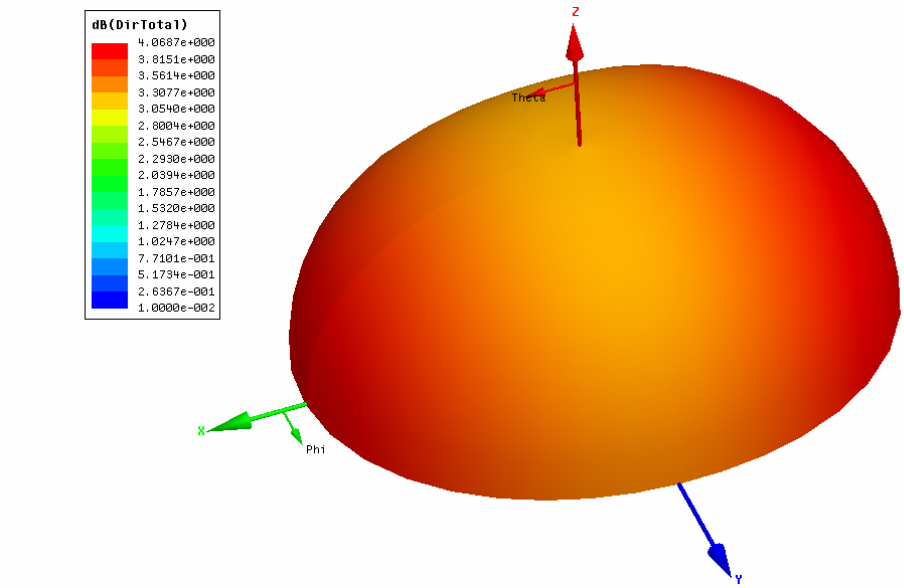


Fig. 4.8 3D directivity pattern of the antenna by HFSS simulation


Fig. 4.9 The Symbol RFID handheld reader (MC9000-G) is the test equipment

Fig. 4.9 shows the picture of the Symbol RFID handheld reader (MC9000-G) we used to test the metal surface mounted RFID transponders. Fig. 4.10 shows a picture of how we did the field test.


Fig. 4.10 The way we field test the reading range

### 4.2.4 Comparison with the published results

Based on the literature, a few metal surface mountable RFID tag antennas have been reported.

From [40], the author proposes a 3-layer antenna design which has a horizontal size 10 cm by 8 cm and thickness 6.455mm, which has a radiation efficiency of 0.6753 and directivity 4.347. Without any doubt, based on this performance, the area and the height are too big. It is a multilayer structure built on Teflon, so it is more expensive to manufacture.

From [41], the authors propose a two-layer structure by using a traditional planar inverted-F antenna. It has a thickness 3 mm and width 45 mm. The deficiency is that the antenna needs two ground connections. It uses Teflon as the substrate. The two shorting plates to ground are in opposite direction, which increases the cost of the fabrication. The best performance is about 5.1 m. For this performance, it is still too wide and too thick.

Based on [30-33], all of the antennas use an inverted-F antenna structure and are mountable on metal. They demonstrates decent reading range but the downside is that they need a relatively expensive substrate material (Teflon), complicated fabrication process, a thick substrate ( 3 mm ~ 4mm) and occupy relatively large areas.

From [46], Kansas University claims that by using about 60 mil thick high density polyethylene, an antenna size of 4 inch by 5.5 inch can achieve a 20 feet reading range. With the same performance, our antenna is only 1.3 inch by 2.6 inch and made using very inexpensive and low dielectric constant foam. Their antenna structure with a higher dielectric constant is still 6.5 times bigger than our invention made by foam.

From US patent No.6329915, the inventers proposed a method of using a high dielectric constant material to reduce the size of the antenna and the distance between antenna and the conducting surface. The cost will be high and the reading range will be low due to the high dielectric material. From US patent No. 7126479 B2, the author discloses a RFID tag which is attachable to a metal container by using a microstrip antenna. The microstrip antenna has a length of a half wavelength, which is two times larger than our invention (less than a quarter wavelengths). From US patent No. 6278369, the inventors present an inverted-F antenna to be applied to conductive surface, but it needs two ground connections and a very thick substrate. From US patent No. 6914562, a surface insensitive antenna structure is proposed. To our knowledge, this kind of antenna doesn't work well on a metal surface.

In conclusion, no ideal solution for a RFID tag mountable on metal has been invented prior to this work. The slotted inverted-L antenna we invented provides an ideal solution. It shows an approximately omnidirectional radiation pattern and enough bandwidth in the ISM (902 ~928 MHz) frequency band. It has a compact size (3 cm by 5 cm), low profile (0.8 mm or 1.6

mm) and good reading range all over the space. It can further be built on an inexpensive foam layer. The fabrication process to do the silver printing and folding is relatively simple. Overall, it is an ideally low cost solution.

## 4.3 An ultra thin and high gain metal-surface mounted RFID transponder antenna with a symmetrically slotted patch

### 4.3.1 Introduction

All of the known commercially available solutions to make the RFID tag antenna working on metal are not long reading range solution. To reach a better reading range, the only way in the present industry is to increase the thickness of the substrate. For a 12 feet reading range, it needs an antenna which is 5.8 inch long, 1 inch wide and 0.2 inch thick. Due to the complicated antenna structure, the cost is about $4 ~ $6 each, which is too expensive and too thick for this performance. In the literature [40] [41] [42] [43] [44] [45], the best reported reading range for an RFID tag is 5.1 m. The substrate thickness is at least 3 mm. Our inverted-L antenna [38] with 62 mils thickness has a reading range typically from 20 feet to 25 feet. In order to achieve a larger reading range, the gain of the antenna should be increased.

In this section, we present an ultra thin and high gain metal-surface mounted RFID tag antenna without requiring a ground connection. Our invention proposes a new antenna structure built on much less expensive foam substrate, which has only 32 mils thick, 1.9 inch wide and 5.2 inch long. It demonstrates a reading range more than 32 feet when it is tested by a Symbol RFID handheld reader (MC9000-G) with 4 W EIRP.

Based on a 3D Electromagnetic simulation, it has directivity bigger than 8.45 dBi but maintain a radiation efficiency of about 30% for a 32 mils thick substrate. For a thicker substrate such as 64 mils, the efficiency can be as high as 54% but the antenna maintains the same directivity, which means a higher reading range ( longer than 40 feet) is achievable.

### 4.3.2. Structure and performance of the slotted RFID antenna patch

Fig. 4.11 (a) and (b) shows an antenna structure which is built on foam. The antenna has a horizontal size 5.2 inch by 1.9 inch and a thickness of 32 mils. The reading range is more than 32 feet at 4 W EIRP.

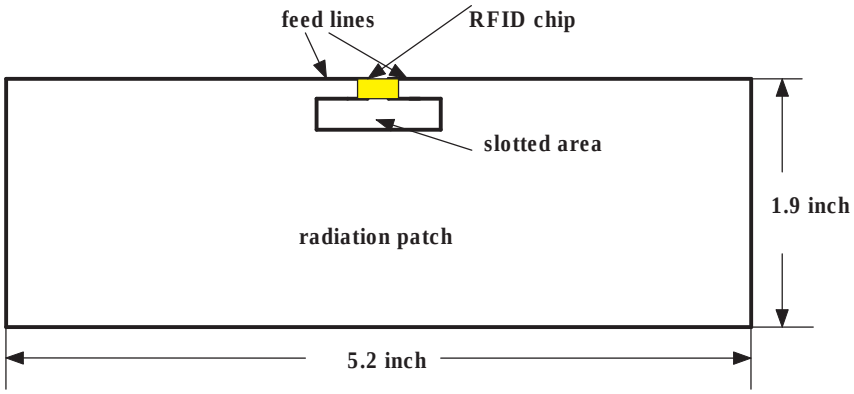


Fig. 4.11 (a) Plan view of a novel slotted microstrip RFID antenna built on foam

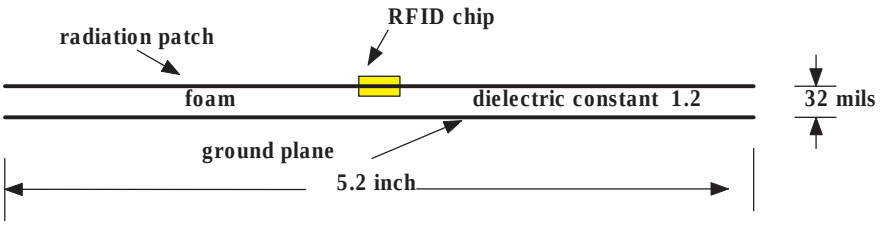


Fig. 4.11 (b) Cross section view of a novel slotted microstrip RFID antenna built on foam

Fig. 4.12 shows the plan view of the novel slotted microstrip antenna for RFID transponder built on foam with a different feeding structure.

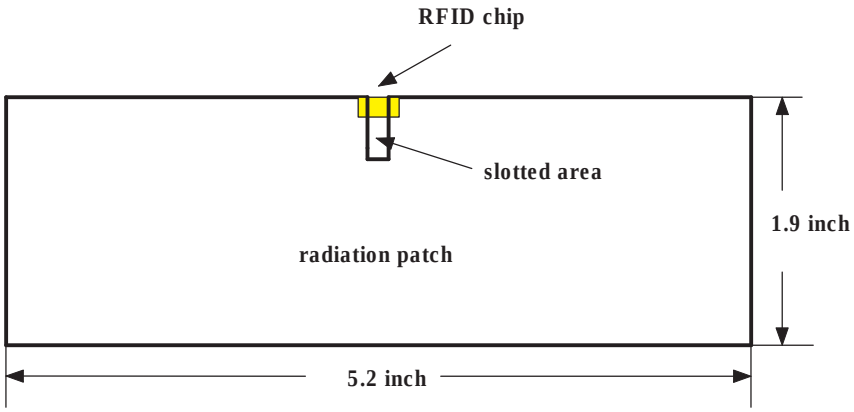


Fig. 4.12 Plan view of a RFID antenna with a different feed built on foam

By using a substrate with a higher dielectric constant, the horizontal size can be further decreased to 4 inch by 1.9 inch. An antenna with the geometry shown in Fig. 4.13 has a tested reading range more than 32 feet. If a smaller size is more desired rather than the long reading range, the antenna size can be decreased to 0.9 inch wide and 3.8 inch long, which still has more than 18 feet reading range.

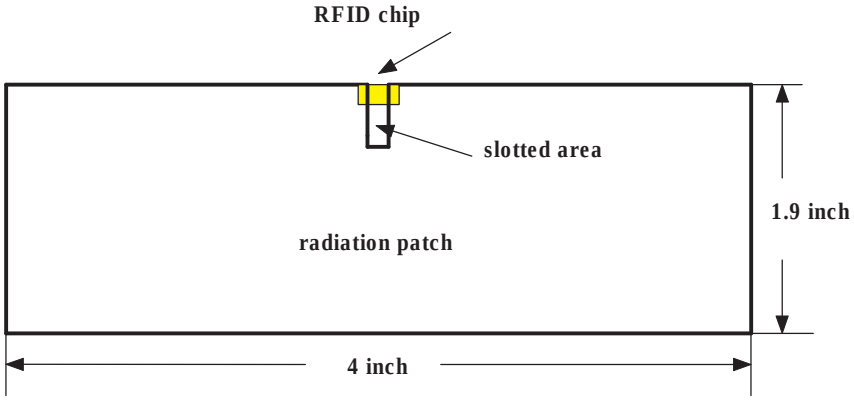


Fig. 4.13 (a) Plan view of a novel slotted microstrip RFID antenna built on RT/DUROID® R 5880

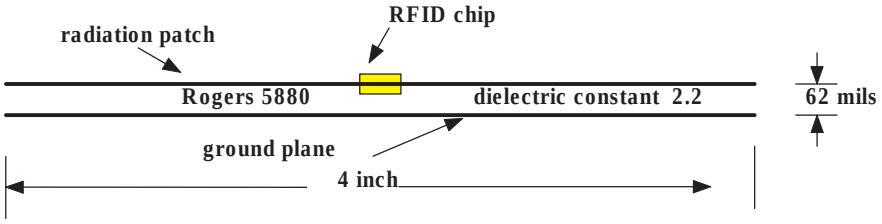


Fig. 4.13 (b) Cross section view of a novel slotted microstrip RFID antenna built on RT/ DUROID® R 5880

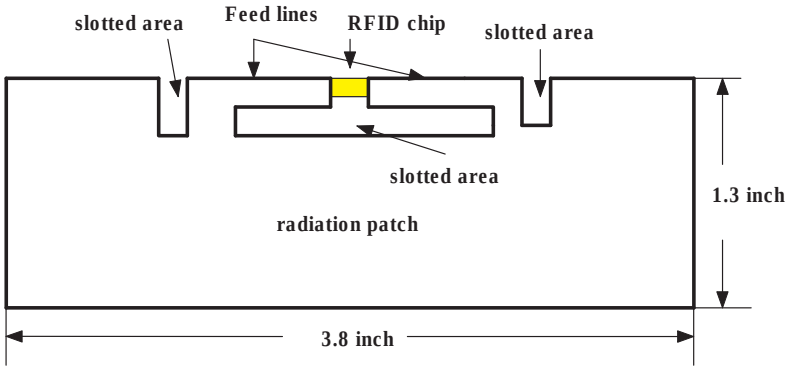


Fig. 4.14 Plan view of a novel slotted microstrip RFID tag with multiple slots and smaller size built on RT/DUROID® R 5880

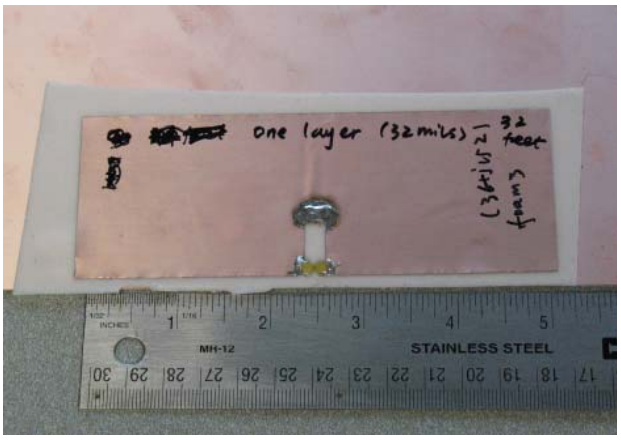


Fig. 4.15 The picture of the proposed slotted microstrip RFID antenna built on foam.

As shown in Fig. 4.14, the horizontal size can be further decreased by introducing multiple

slots in the radiation patch. Fig. 4.15 shows the fabricated slotted microstrip RFID built on one layer (32 mils thickness) foam substrate.

(a) (b)

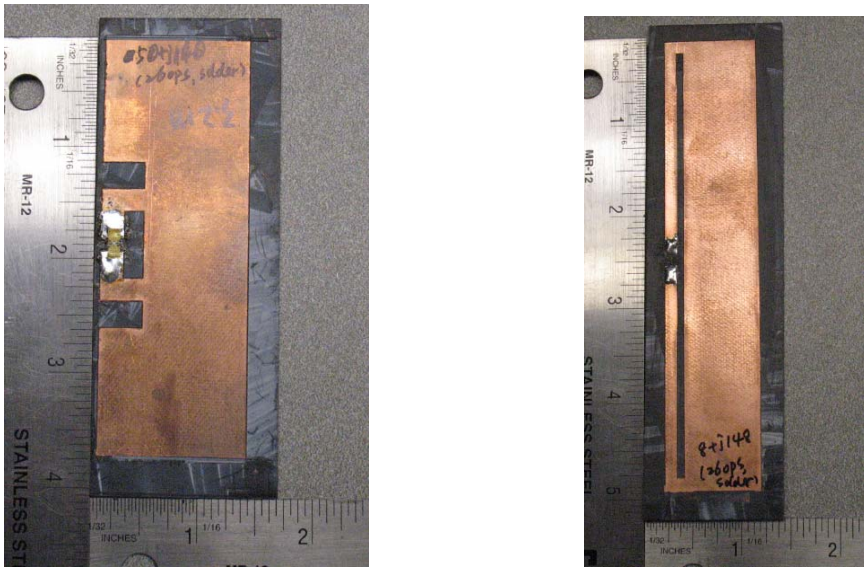

( c) (d)

Fig. 4.16 (a) (b) (c) (d) The pictures of the proposed slotted microstrip RFID antenna built on Rogers RT/DUROID® R 5880

Fig. 4.16 (a) (b)(c)(d) shows the pictures of the various fabricated slotted microstrip RFID antenna built on RT/DUROID® R 5880.

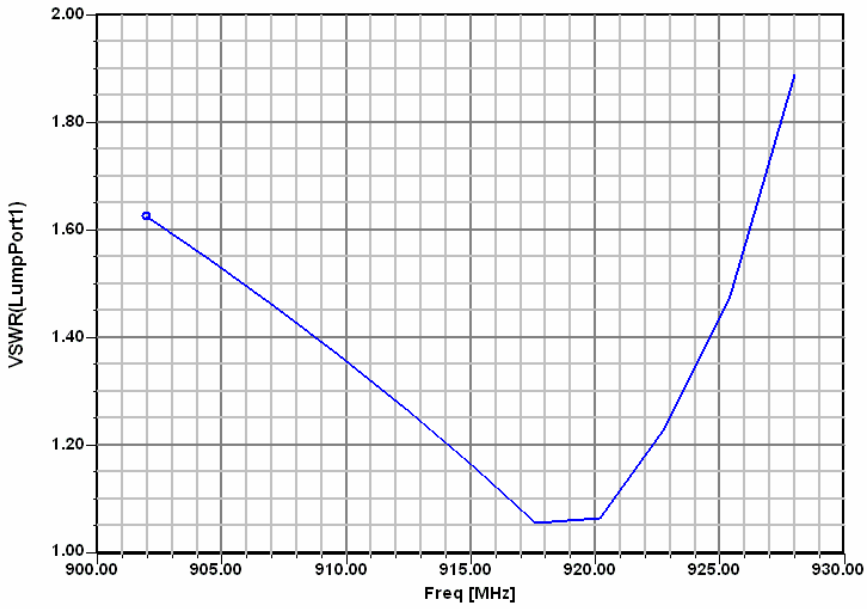


Fig. 4.17 Simulated VSWR of the proposed RFID tag antenna shown in Fig. 4.15 made on foam

The simulated VSWR of the invented RFID tag antenna shown in Fig. 4.15 is plotted in Fig. 4.17, which is less than 2 in the ISM frequency band.

The antenna shown in Fig. 4.15 has a directivity pattern in the elevation plane plotted in Fig. 4.18. The directivity pattern at the azimuthal plane derived by HFSS is plotted in a solid line. The measured directivity pattern is plotted in a dashed line, which is calculated based on the reading distance. It is normalized to the calculated maximum directivity. The simulated results shows a maximum directivity about 7 or 8.45 dBi, which is about twice as large as the inverted-L antenna. The price paid is a larger horizontal size. The antenna shows a half power bandwidth (HPBW) about 45 degree and a first null bandwidth (FNBW) 90 degree.

The antenna has a gain about 3 dBi even at the horizontal angle of 60 degree, which is desired for RFID application.

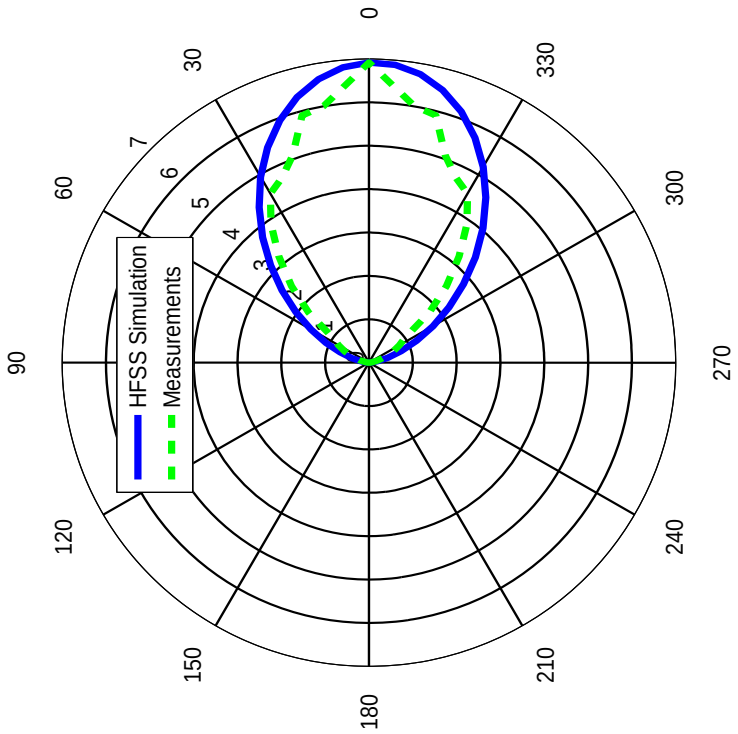


Fig. 4.18 Simulated and measured directivity pattern (numeric value) in the azimuthal plane for the antenna shown in Fig. 4.17

The 3 D directivity pattern is plotted in Fig. 4.19, which shows the radiation pattern is symmetrical about the vertical direction.

Compared with any other known long range (larger than 20 feet) metal-surface mounted RFID tag, this invention represents the thinnest structure, the smallest size, the lowest fabrication cost and better reading range.

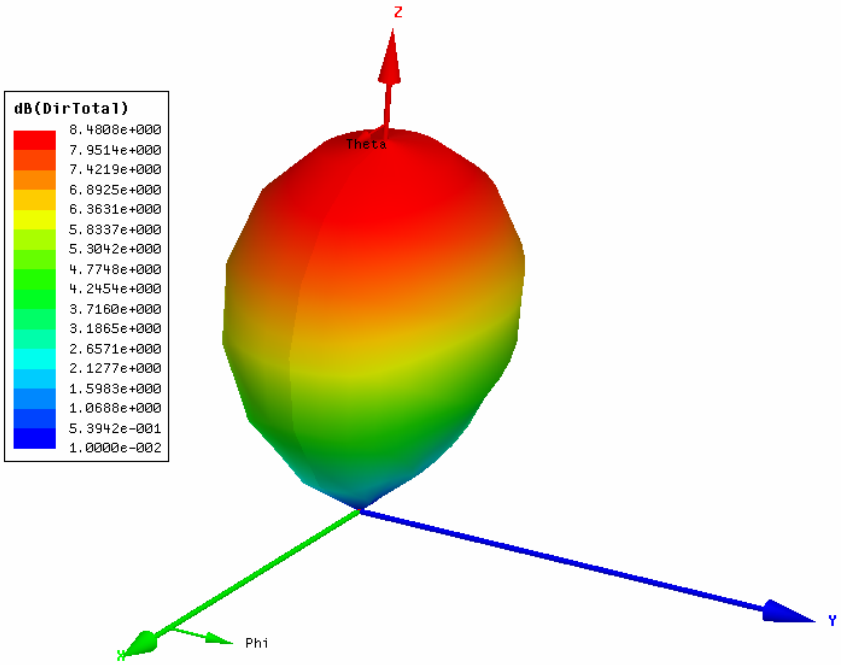


Fig. 4.19 A 3D directivity pattern of the slotted microstrip antenna derived by HFSS

## 4.4 Antenna differential input impedance measurements

In the RF world, almost always people are dealing with single ended circuits which have an immediate reference to ground. The commonly used network analyzer such as HP85047A in our lab uses 50 ohms coaxial cable and is designed for that purpose. The RFID antenna is unfortunately a differential structure. The network analyzer using coaxial cable is not able to measure the differential input impedance since the coaxial cable is unbalanced. It is a well known technology to use a BALUN (balance to unbalance) to measure or feed differential circuits. However, building a broadband BALUN is extremely difficult and expensive.

In order to do broadband measurements for the differential antenna input impedance, a way based on matrix transformation is applied to do that.

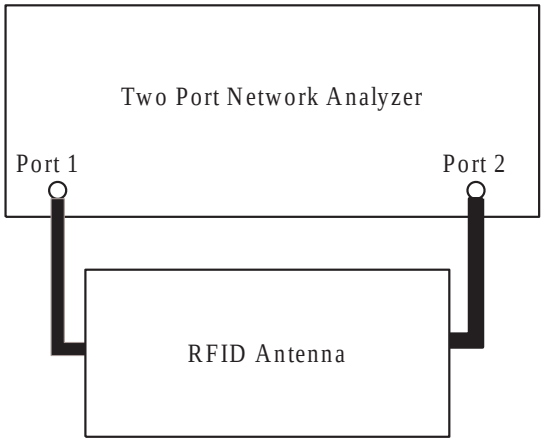


Fig. 4.20 Two-port S parameters measurements

As shown in Fig. 4.20, the two-port S parameters are measured by using the single ended two-port network analyzer and coaxial cables. Then the S matrix is transformed into a Y matrix using the following equations [20],

$$Y_{11} = Y_0 \frac{(1-S_{11})(1+S_{22})+S_{12}S_{21}}{(1+S_{11})(1+S_{22})-S_{12}S_{21}} \tag{4.1}$$

$$Y_{12} = Y_0 \frac{-2S_{12}}{(1+S_{11})(1+S_{22})-S_{12}S_{21}} \tag{4.2}$$

$$Y_{21} = Y_0 \frac{-2S_{21}}{(1+S_{11})(1+S_{22})-S_{12}S_{21}} \tag{4.3}$$

$$Y_{22} = Y_0 \frac{(1+S_{11})(1-S_{22})+S_{12}S_{21}}{(1+S_{11})(1+S_{22})-S_{12}S_{21}} \tag{4.4}$$

In Fig. 4.21, the Y matrix is derived from the measured S matrix by equations (4.1) to (4.4). A differential voltage source is then applied to the input terminals. Then the differential input impedance can be easily found based on the two-port Y parameters. The method is accurate

for any frequency range. The final derived input admittance is derived as,

$$Y_{in} = \frac{(Y_{11} + Y_{12})(Y_{21} + Y_{22})}{Y_{11} + Y_{12} + Y_{21} + Y_{22}} - Y_{12} \tag{4.5}$$

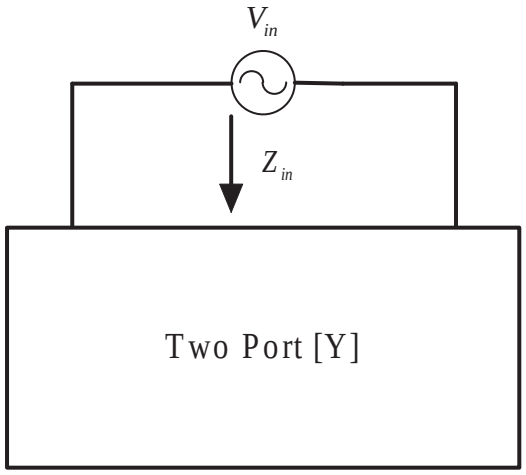


Fig. 4.21 Differential input impedance is derived by the two-port Y matrix

## 4.5 Analysis of a planar RFID antenna

A full-wave 3D EM simulation tool like HFSS [10] is able to model a complicated antenna structure. The simulated results like radiation pattern and input impedance are shown in sections 4.2 and 4.3. To gain a better understanding of the antenna, in this section we use the slotted inverted-L antenna as an example to demonstrate how to analyze the antenna input impedance by using transmission line theory. We'll show even though the transmission line modeling is good for predicting the input impedance of the antenna, it is not sufficient to predict the radiation efficiency if the radiation impedance of the antenna is ignored. A simple resonator model is proposed to model the power loss due to the substrate and finite

conductivity of the metal. The effect of the substrate tangent loss on the radiation efficiency is analyzed in detail.

### 4.5.1 Antenna input impedance

The input impedance of a transmission line with characteristic impedance $Z_0$, length $d$ and load impedance $Z_l$ is expressed as [47],

$$Z_{in} = Z_0 \frac{1+\Gamma_L e^{-2\gamma d}}{1-\Gamma_L e^{-2\gamma d}} \tag{4.6}$$

$$\gamma = \alpha + j\beta \tag{4.7}$$

$$\Gamma_L = \frac{Z_l - Z_0}{Z_l + Z_0} \tag{4.8}$$

where $\gamma$ is the propagation constant, $\alpha$ is the attenuation constant and $\beta$ is the phase constant.

The radiation impedance of the RFID microstrip antenna is difficult to be accurately derived analytically although some approximate formulas are available. For a better accuracy, the radiation impedance of a microstrip line with line-width of W is derived by HFSS simulation. For an open ended microstrip transmission line, when the length of the microstrip line is set to be a half wavelength at the design frequency, the input impedance is equal to the load impedance, which will be the radiation impedance. The transverse current in the microstrip antenna can't be modeled by transmission line equations since the transmission line model is based on a TEM plane wave approximation and only longitudinal current is considered. The effect of the transverse current is modeled as inductors, which are derived by the unit inductance of the transmission line in the transverse direction. A microstrip line built with

RT/DUROID® R 5880 with a thickness of 62 mils, a width of 1 inch has the radiation impedance 18-j197 ohms. The whole inverted-L antenna shown in Fig. 4.22 (a) is divided into six transmission lines sections connected by three inductors. The following derivation gives the formula to calculate the inductance of the microstrip line,

$$Z_0 = \sqrt{\frac{L}{C}}, \quad \frac{L}{C} = Z_0^2 \tag{4.9}$$

$$v = \frac{1}{\sqrt{LC}}, LC = \frac{1}{v^2} \tag{4.10}$$

$$L^2 = \frac{Z_0^2}{v^2} \tag{4.11}$$

$$L = \frac{Z_0}{v} = \frac{Z_0\sqrt{\varepsilon_r}}{c} \tag{4.12}$$

where $v$ is the wave velocity, $\varepsilon_r$ is the relative dielectric constant of the substrate dielectric, $L$ is the inductance per unit length and $C$ is the capacitance per unit length. The characteristic impedance was derived by LineCalc in ADS 2005. Then the input impedance can be calculated by (4.6). To facilitate the calculation, an ADS modeling is setup and the input impedance is computed by the software. The modeling interface is shown in Fig. 4.22 (b).

The ADS simulation shows the antenna input impedance equal to 11.8+j61.0 ohms, which is close to 15.0+j120.0 ohms derived by HFSS simulation at 915 MHz. The impedance difference may come from an inaccurate inductance modeling of the small circular loop in the feeding area. The result of ADS simulation is shown in Fig 4.23. Fig 4.23 (a) plots the radiation impedance of the microstrip line. After adding a less than quarter- wavelength transmission line (TL), the input impedance is shifted close to the short point in Smith Chart, which is plotted in Fig. 4.23 (b). Fig 4.23 (c) shows the input impedance of the grounded

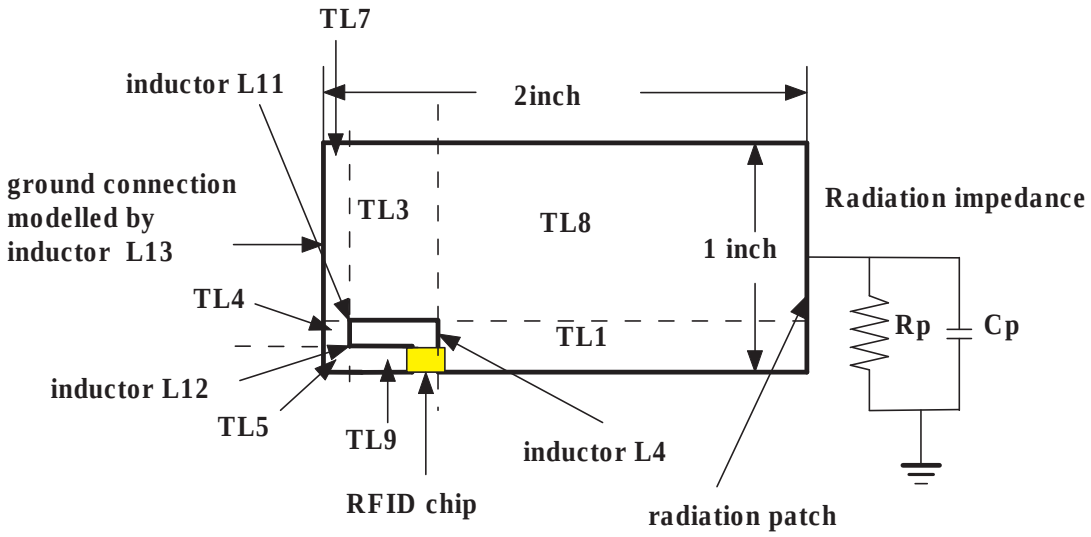


Fig. 4.22 (a) Model the slotted inverted-L RFID antenna using transmission line and inductors

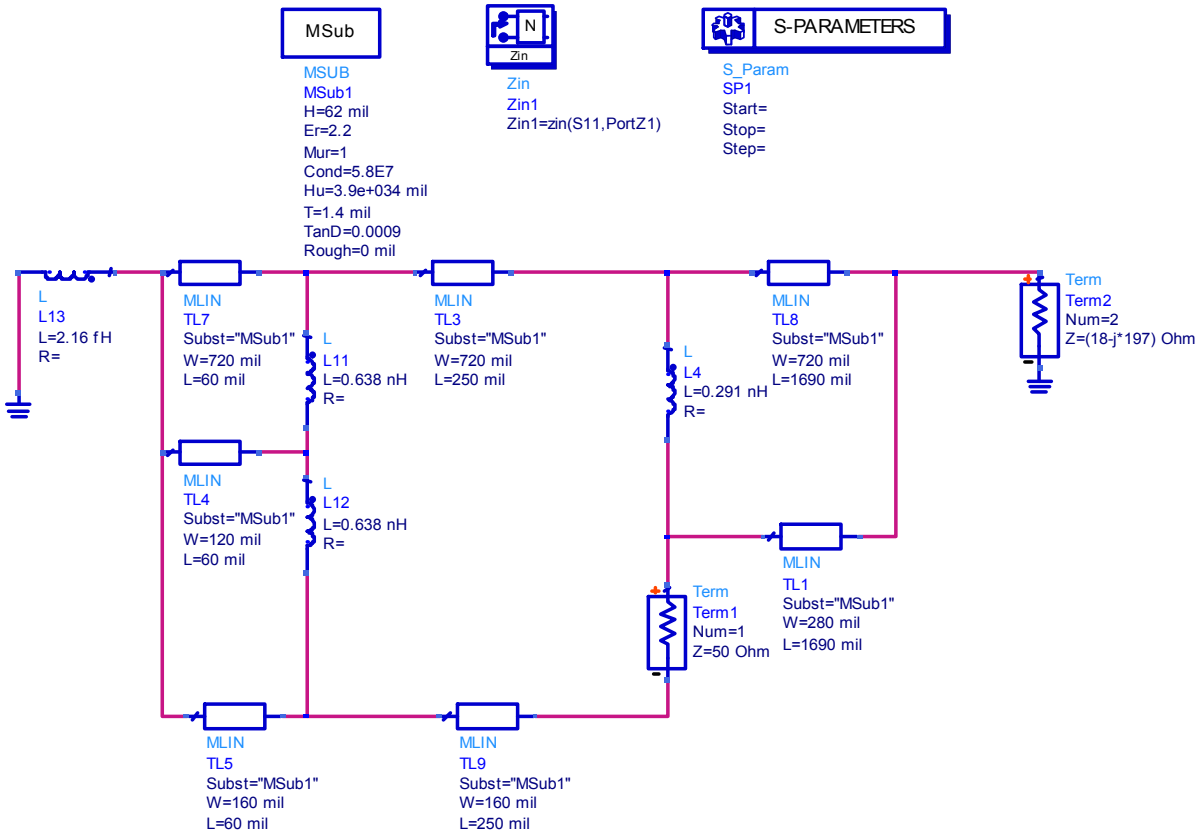


Fig. 4.22 (b) The corresponding ADS transmission line modeling of the inverted-L antenna

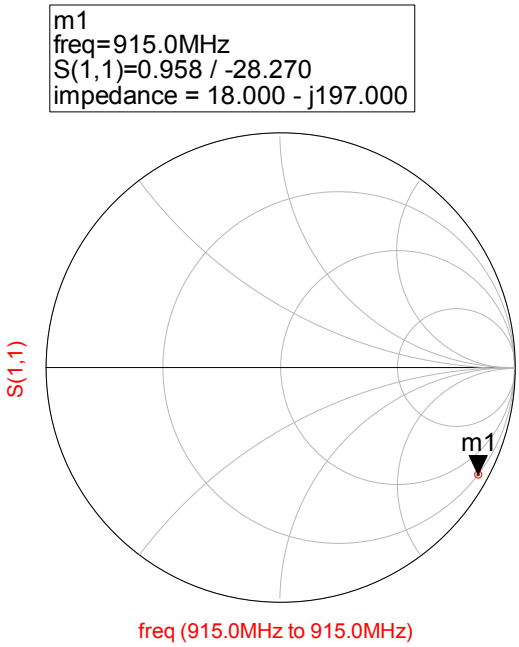


(a) S11 of the radiation impedance

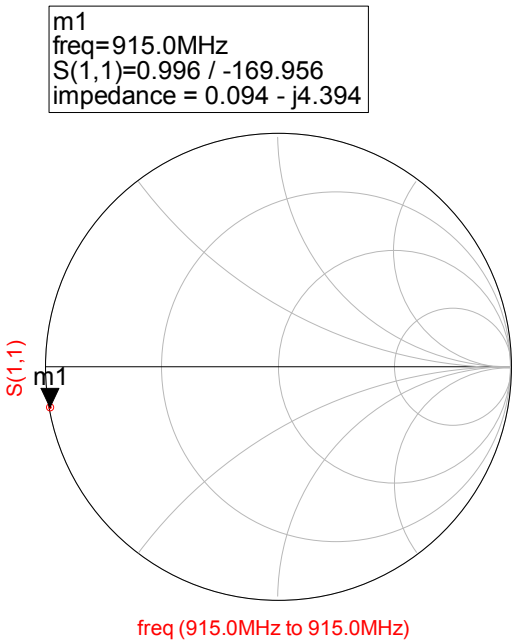


(b) S11 after 1690 mil TL

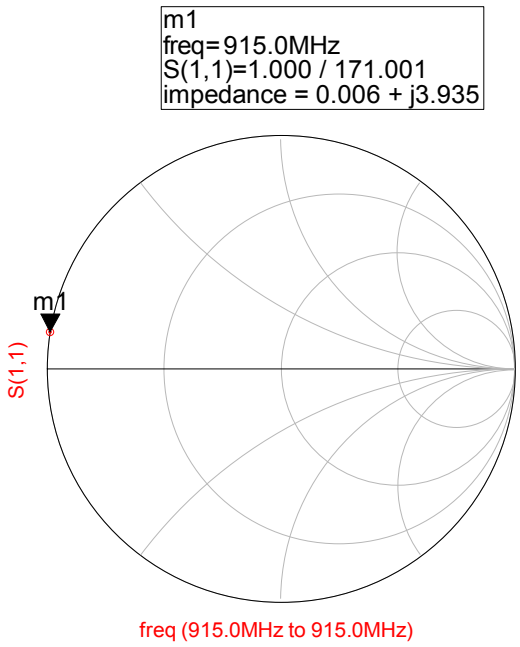


( c) S11 of the grounded TL

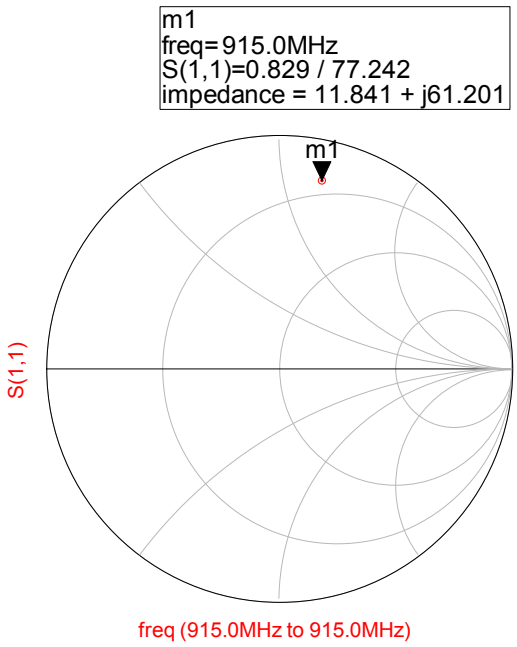


(d) S11 of the overall antenna

Fig. 4.23 The input impedance of the RFID tag antenna by transmission line modeling

short stub, which represents a small inductance. The parallel combination of Fig. 4.23 (b) and (c) generates the desired antenna impedance, which is shown in Fig 4.23 (d). The antenna surface current on the top metal layer is plotted in Fig. 4.24. It reaches the minimum at the radiation slot or open end. It has the maximum value at the feeding area. As shown in Fig. 4.25, the E field distribution has the maximum value at the radiation slot or open end. It has the minimum value at the feeding area. The results are predictable based on transmission line theory. By virtue of the equations from [47], the voltage and current distribution on a loaded lossless transmission can be written as,

$$V(z') = V_L\left[\cos(\beta z') + j\frac{Z_0}{Z_L}\sin(\beta z')\right] \tag{4.13}$$

$$I(z') = I_L\left[\cos(\beta z') + j\frac{Z_L}{Z_0}\sin(\beta z')\right] \tag{4.14}$$

$$V_L = I_L Z_L \tag{4.15}$$

The load impedance is equal to the radiation impedance, which is 18-j197 ohms. The characteristic impedance of a width 1000 mils microstrip line RT/DUROID® R 5880 derived by LineCalc is 13.5 ohms. Therefore the characteristic impedance is much less than the load impedance. From (4.13), the first term will be dominant. Therefore an approximate standing wave is formed in the transmission line section, which has a voltage maximum at the load ($z' = 0$) and voltage minimum at the feeding area ($z' = 1000$ mils, about 80 degree electric length). From (4.14), the second term is dominant. As a result, the current minimum appears at the load ($z' = 0$) and a current maximum is on the input end ($z' = 1000$ mils). The theoretical analyses predict the results shown in Fig. 4.24 and 4.25.

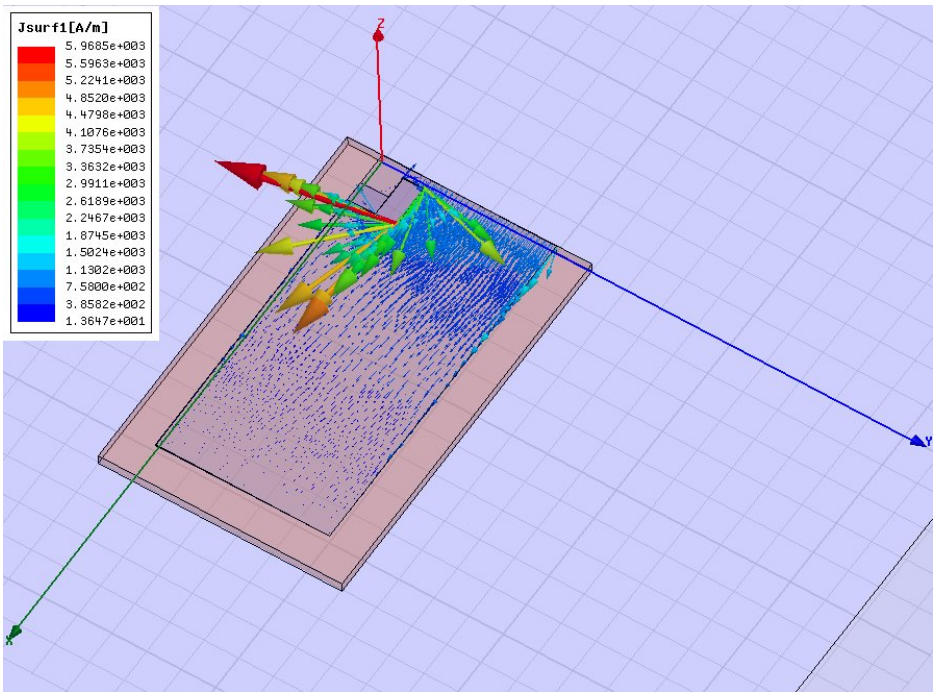


Fig. 4.24 Antenna surface current distribution

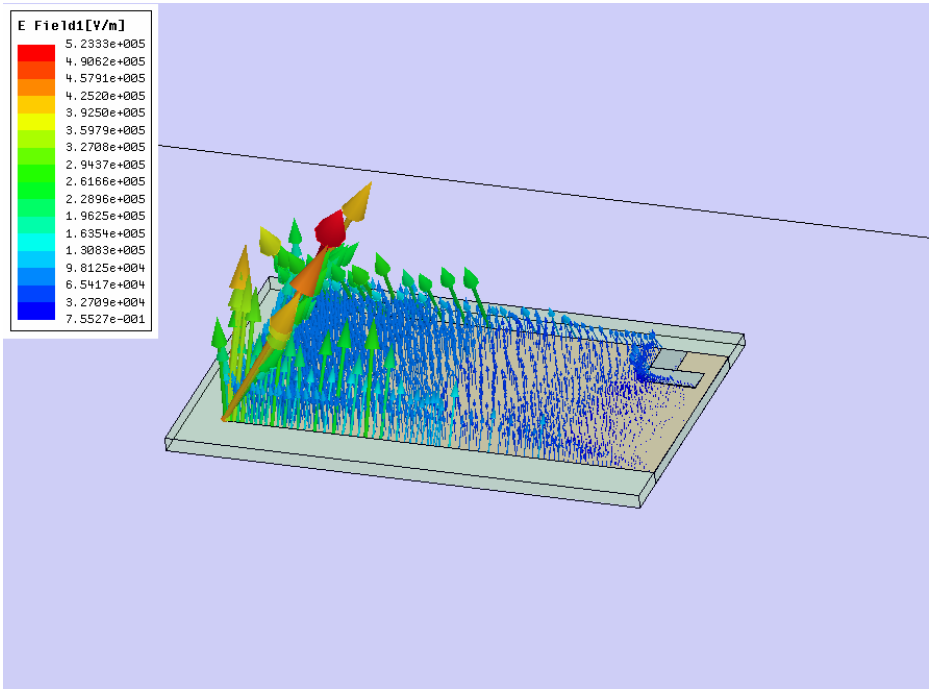


Fig. 4.25 Antenna electric field distribution

### 4.5.2 Antenna radiation efficiency

Increasing the antenna radiation efficiency is a good part for the low profile microstrip antenna design. In this section, we'll show that a transmission line model is insufficient to predict the radiation efficiency. To predict the power loss due to the substrate material, a simple resonator model is derived and demonstrates its effectiveness.

A microstrip line can be closely approximated by the parallel-plate transmission line [47]. The unit length resistance R, inductance L, capacitance C and conductance G are calculated as,

$$R = 2\frac{R_s}{W} = \frac{2}{W}\sqrt{\frac{\omega\mu}{2\sigma_c}},\ L = \mu\frac{d}{W},\ C = \varepsilon\frac{W}{d},\ G = C\frac{\sigma_d}{\varepsilon} \tag{4.16}$$

From Maxwell's equation, the equivalent conductivity for the dielectric is derived as follows,

$$\begin{aligned}\nabla \times H &= j\omega\varepsilon E = j\omega(\varepsilon' - j\varepsilon'')E = j\omega\varepsilon'(1 - j\frac{\varepsilon''}{\varepsilon'})E = j\omega\varepsilon'(1 - j\tan\delta)E \\ &= j\omega\varepsilon' E + \omega\varepsilon'\tan\delta E\end{aligned} \tag{4.17}$$

From (4.17), the equivalent conductivity for the dielectric is derived as $\sigma_d = \omega\varepsilon'\tan\delta$.

An inverted-L antenna made on two-layer foam has a width of 1300 mil, length of 2600 mil and thickness of 68 mils. The conductivity of the metal layer is $\sigma_c = 5.1\times10^7$ s/m. The relative dielectric constant $\varepsilon_r$ is 1.19. The tangent loss ($\tan\delta$) of the substrate material is 0.001 at 915MHz. Based on the above parameters, the R, L, C and G of the microstrip line is calculated as,

$$\begin{aligned}&R = 0.5096(\Omega/\text{m}), C = 2.0134\times10^{-10}(\text{F/m}), \\ &L = 6.573\times10^{-3}(\text{H/m}), G = 1.157\times10^{-3}(\text{S/m})\end{aligned} \tag{4.18}$$

The characteristic impedance is calculated as $Z_0 = \frac{d}{w}\sqrt{\frac{\mu}{\varepsilon}} \approx 19.7\Omega$.

The attenuation constant by $\alpha \approx \frac{1}{2}(\frac{R}{Z_0} + GZ_0)$ [47] is 0.0243(Np/m) or 0.21(dB/m). For a matched transmission line with a total length of 2600 mils, the overall attenuation due to the power transmission is about 0.014 dB, which means a 0.32% power loss. It is understandable due to the low loss material for power transmission. By a more accurate HFSS simulation, the antenna has a radiation efficiency of 58%. The big difference tells us that the loading effect of the radiation impedance should be considered to predict the radiation efficiency.

The radiation impedance of the microstrip line is 14.9-j177 ohms, which is equal to a radiation conductance $G_r$ of 4.722E-4 s in parallel with a radiation capacitance $C_r$ of 0.976 pF. The equivalent total capacitance $C_l$ due to the RFID antenna is 13.27 pF, the total equivalent conductance $G_l$ due to the dielectric layer is 7.64E-5 s.

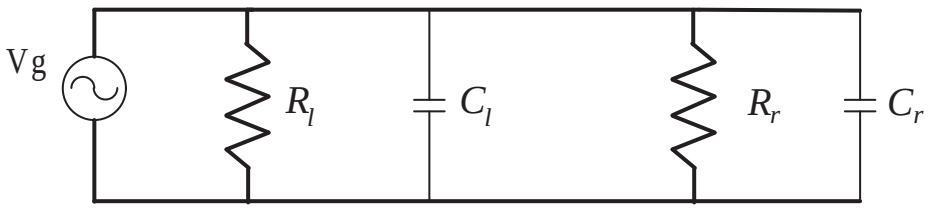


Fig 4.26 A resonator model for the substrate loss

With a resonator model shown in Fig. 4.26, the overall power efficiency is determined by the conductance ratio,

$$\varepsilon_d \approx \frac{G_r}{G_r + G_l} = 0.861 \tag{4.19}$$

where $G_r$ is the radiation conductance, $G_l$ is the loss conductance due to the substrate.

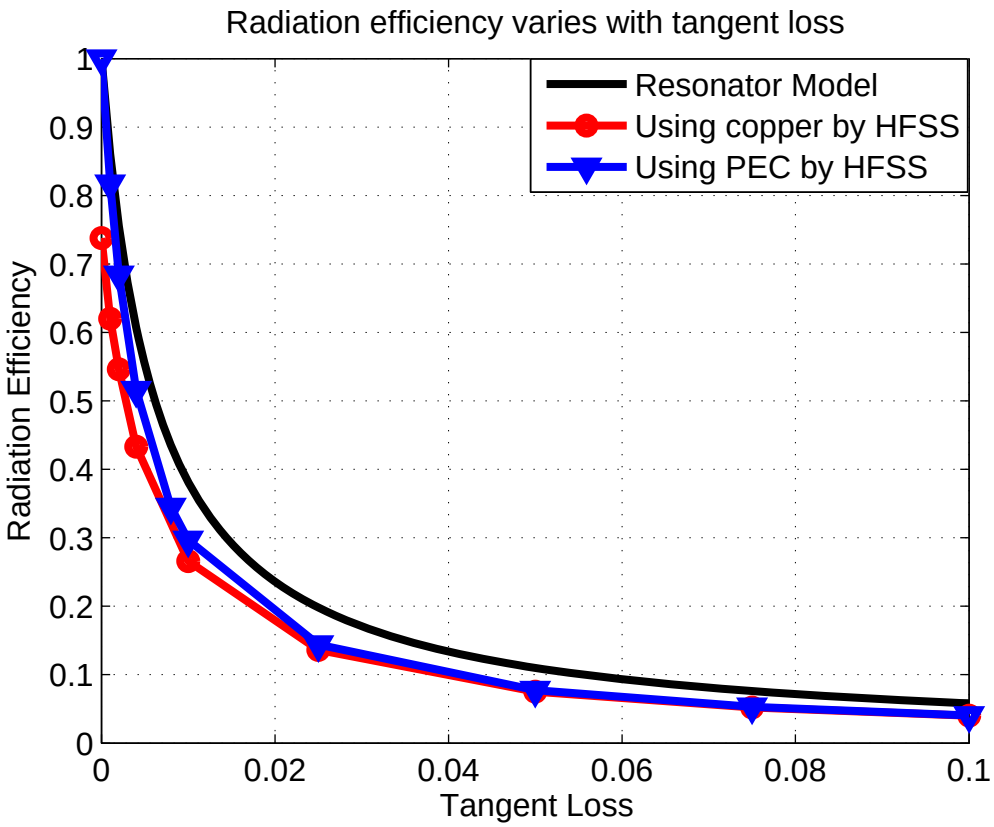


Fig. 4.27 The effects of substrate tangent loss on the antenna radiation efficiency

The radiation efficiency varying with the tangent loss factor is plotted in Fig. 4.27. A more accurate HFSS simulation is conducted to make a comparison. The solid curve is derived from the simple resonator model. The solid line with an inverted triangle is the simulation results from HFSS by changing the real metals to PEC. Therefore, it includes only the power loss due to the dielectric layer. The solid line with a circle is the simulation results from HFSS by applying finite conductivity to metal (5.8E7 s/m). It is clear that the power loss due to the finite conductivity of metal is large when the tangent loss of substrate is small. The power loss due to the finite conductivity of metal is reduced when the tangent loss increases.

From Fig. 4.27, it can be seen that even though the model is simple, it predicts the

efficiency relatively well. When the tangent loss of the substrate is 0.01, the 3D HFSS simulation gives a radiation efficiency of 0.297 with PEC; the simple model gives radiation efficiency of 0.38. When the tangent loss of the substrate is 0.025, the radiation efficiency is 0.144 with PEC given by HFSS simulation and 0.2 given by the simple model. The model is more accurate when the tangent loss increases. It is clear that a low loss substrate material is necessary to achieve a highly efficient microstrip-type antenna.

## 4.6 Reexamine the RFID reading range

A RFID transponder attaches a RFID chip to an antenna. The Symbol MC9000-G RFID reader is applied to do the field test. The RFID chip manufacturer specifies the typical input power for reading is about -13 dBm; the minimum input power for reading is -9 dBm. If the inverted-L antenna with a directivity 4.15 dBi and efficiency 58% is applied, from (2.65), -13 dBm and -9 dBm input powers correspond to a reading distance of 9.05 m and 5.7m, respectively. Our tested results show that the folded inverted-L RFID antenna achieves 20~28 feet reading range, which is 6.1 m ~ 8.53 m reading distance. The good agreement shows that the minimum input power of the RFID chip is a major limitation for the reading range. The minimum input power of the RFID chip is set by the low efficiency of the rectifier and multiplier.

The slotted high gain antenna has a directivity 8.45 dBi and 54% efficiency with 64 mil (1.63 mm) thickness. It has a theoretical reading range from 9.04m~14.3m. Our tested results constantly give 9.75m~11.0 m reading range. A good agreement between theoretical and tested results is achieved.

For an active RFID, with a fixed power supply, the rectifier won't become a limiting factor any more. Therefore the reading distance will be determined by the backscattering and sensitivity of the receiver. For a receiver with a nominal -90 dBm sensitivity, a 36.6 meter reading distance is achievable with the inverted-L antenna design, which is five times longer than the passive RFID transponder. The reading range of an active RFID transponder is limited by the sensitivity of the RFID reader.

# CONCLUSION

As one of the major applications of wireless communications, RFID shows similar properties to the other applications. However, since it communicates by using the reflected power, it exhibits a distinct property. To facilitate the task about how to improve the reading range of a metal surface mounted RFID transponder, the operation principle and internal IC structure of a RFID reader and transponder are presented. A system level link-budget analysis relating the RFID reader and RFID transponder is conducted. The major factors limiting the reading range are derived. It has been shown that for a passive RFID transponder, the low efficiency of the rectifier is the major limiting factor. For an active RFID transponder, the sensitivity of the RFID reader determines the maximum achievable reading range. To be able to improve the reading range for an existing reader and transponder chip, the gain and the radiation efficiency of the transponder antenna are the only variables which can be improved.

In order to boost the radiation efficiency of a metal surface mounted RFID transponder, metamaterials including FSS and mushroom-like EBG surface have been studied. Different from the smooth metal surface, FSS and mushroom-like EBG surfaces exhibit high impedance electromagnetic properties and in-phase reflection profile at a certain frequency band. Our study shows that for a low profile FSS and mushroom-like EBG surface, their reflection phase profiles have negligible difference. The measured transmission coefficients of TM waves or TE waves across the FSS and mushroom-like EBG surface are similar to each other. Both of them exhibits TM bandgap and in-phase reflection and can be named as EBG surfaces.

With a better understanding of the TE wave across the EBG surfaces, we originally proposed a new equivalent circuit model. The distinct effects of TM and TE waves on the radiation impedance of metal-surface mounted dipole antennas are examined. Our research demonstrated that in the frequency range where the TM wave is suppressed but the TE wave is supported, the metal-surface mounted dipole antenna can be integrated onto EBG surfaces and achieve very good impedance matching and radiation efficiency. Even though metamaterials have the potential to be applied to boost the radiation efficiency, the horizontal dimension is relatively large for most of RFID application. To save the overall area and cost of RFID, two major types of antennas for RFID transponders were invented.

One type of antennas has an inverted-L planar structure. The other type of antenna has a symmetric structure without physical connection to the ground. They were designed using inexpensive foam and RT/DUROID® R 5880 high frequency laminates. These antennas have an approximately omnidirectional radiation pattern, high gain, compact size and low profile. With a handheld reader, the reading range can be achieved more than 20 feet for the inverted-L antenna and more than 30 feet for the symmetric antenna. The tested reading range agreed well with the analytical results. A transmission line modeling of the invented RFID antennas is given and proved its effectiveness to predict the input impedance of the antenna. A simple resonator model is proposed to relate the antenna radiation efficiency to the tangent loss of the substrate material. Its effectiveness is verified by HFSS simulation.

These inventions exhibited superior performance relative to the previous solutions. Our work has solved one of the largest challenges in RFID industry to make the UHF RFID transponders readable above metal surface and paved the road for RFID industry to expand their market.

# BIBLIOGRAPHY

[1] H. Stockman, "Communication by means of reflected power," *Proc. IRE.*, pp.1196-1204, Oct. 1948.

[2] J. Landt, "The history of RFID,"ieeexplore.ieee.org/iel5/45/33027/01549751.pdf, 2005.

[3] http://www.idtechex.com/research/articles/rfid_market_to_reach_7_26bn_in_2008_00000169.asp, April, 2005.

[4] K. Finkenzeller, *RFID handbook, Radio-Frequency Identifications Fundamentals and Applications,* 2nd ed. John Wiley & Sons, Inc., 2003.

[5] C. Balanis, *Antenna Theory: Analysis and Design*, 3rd ed. New York: Wiley, 2005.

[6] C. Balanis, *Advanced Engineering Electromagnetics*, New York: Wiley, 1989.

[7] R.Harrington, *Field Computation by Moment Methods*, New York:Wiley-IEEE Press, 1993.

[8] M.Sadiku, *Numerical Techniques in Electromagnetics*, 2nd ed. Boca Raton, FL: CRC, 2000.

[9] Momentum Manual of *Advanced Design System 2005A*, 2005.

[10] HFSS Manual of *Ansoft HFSS V10, 2006.*

[11] L.W.Couch, *Digital and Analog Communication Systems*, 7th ed, Upper Saddle River, NJ: Prentice Hall, 2007.

[12] T.S. Rappaport, *Wireless Communications: Principles and Practice*, 2nd ed, Upper Saddle River, NJ: Prentice Hall, 2002.

[13] B. Razavi, *RF Microelectronics*, 1st ed, Upper Saddle River, NJ: Prentice Hall, 1997.

[14] T. Lee, *The design of CMOS Radio-Frequency Integrated Circuits*, 2nd ed, Cambridge University Press, 2004.

[15] U.Karthaus and M.Fischer, "Fully integrated passive UHF RFID transponder IC with 16.7 uW minimum RF input power," *IEEE Journal of Solid-State Circuits*, vol. 38, no. 10, pp. 1602-1608, Oct. 2003.

[16] J.P.Curty, N.Joehl, C.Dehollain, and M.J.Declercq, "Remotely powered addressable UHF RFID integrated system," *IEEE J. Solid-State Circuits*, vol. 40, no.11, pp. 2193-2202, Nov. 2005.

[17] P.B. Khannur, X.Chen, D. Yan, D. Shen, B. Zhao, M.K. Raja, Y. Wu, R. Sindunata, W. Yeoh, and R. Singh, "A universal UHF RFID reader IC in 0.18-um CMOS technology," *IEEE J. Solid- State Circuits*, vol. 43, no.5, pp. 1146-1155, May 2008.

[18] Data sheet of MC9000-G RFID handheld reader.

[19] G. Gonzalez, *Microwave transistor amplifiers: analysis and design*, 2nd ed. Prentice Hall, 1996.

[20] R. J. Weber, *Introduction to Microwave Circuits: Radio Frequency and Design Applications*, New York: Wiley, 2001.

[21] D. M. Pozar, *Microwave Engineering*, 3rd ed. John Wiley & Sons, Inc, 2005.

[22] S. Y. Zhan, R.J. Weber, and J.M. Song, "Effects of frequency selective surface (FSS) on enhancing the radiation efficiency of metal-surface mounted dipole antenna," *IEEE MTT-S International Symposium*, Honolulu, Hawaii, pp. 1659-1662, June 2007.

[23] S. Y. Zhan, R.J. Weber, and J.M. Song, "A new approach to design a low profile dipole antenna backed by a mushroom-like electromagnetic bandgap (EBG) surface," *IEEE AP-S International Symposium*, Honolulu, Hawaii, pp. 4060-4063, June 2007.

[24] D. Sievenpiper, L. Zhang, R. F. J. Broas, N. G. Alexopolus, and E. Yablonovitch, "High-impedance electromagnetic surfaces with a forbidden frequency band," *IEEE Trans. Microwave Theory and Tech.*, vol. 47, no.11, pp.2059-2074, Nov. 1999.

[25] F. Yang and Y. Rahmat-Samii, "Reflection phase characterization of the EBG ground plane for low profile wire antenna applications," *IEEE Trans. Antennas Propagat.,* vol.51, pp.2691-2703, Oct. 2003.

[26] R. F. J. Broas ,D. Sievenpiper, and E.Yablonovitch, "A high-impedance ground plane applied to a cellphone handset geometry," *IEEE Trans. Microwave Theory and Tech*., vol.49, no.7, pp.1262-1265, July 2001.

[27] B. A. Monk, *Frequency Selective Surfaces, Theory and Design*, Wiley-Interscience, 2000.

[28] F. Yang and Y. Rahmat-Samii, "Wire antennas on artificial complex ground planes: a new generation of low gain antennas," *2004 IEEE Symposium on Antennas and Propagation and USNC/URSI Nation Radio Science Meeting*, Monterey, CA, June 20-26, 2004.

[29] A.P.Feresidis, G.Goussetis, S.Wang, and J.Vardaxoglou, "Artificial magnetic conductor surfaces and their application to low-profile high-gain planar antennas," *IEEE Trans. Antennas Propag*., vol.53, no.1, pp.209-215, Jan. 2005.

[30] D. Sievenpiper, "High-impedance electromagnetic surfaces," Ph.D. Dissertation, Dept. Elect. Eng., Univ. California at Los Angeles, Los Angeles, CA, 1999.

[31] R. Collin, *Field Theory of Guided Waves, second edition.* New York, IEEE Press, 1991.

[32] C. Caloz and T. Itoh, *Electromagnetic Metamaterials: Transmission Line theory and Microwave Applications*, John Wiley & Sons, Inc, 2006.

[33] S. Ramo, J.R.Whinnery, and T.V.Duzer, *Fields and Waves in Communication Electronics*, 3rd ed,

John Wiley & Sons, Inc, 1994.

[34] R.A.Shelby, D.R.Smith, and S.Schultz, "Experimental verification of a negative index of refraction," *Science*, vol.292, no.5514, pp.77-79, 2001.

[35] D. R. Smith, W. J. Padilla, D. C. Vier, S. C. Nemat-Nasser, and S. Schultz, "Composite medium with simultaneously negative permeability and permittivity," *Phys. Rev. Lett.*, vol. 84, no. 18, pp. 4184-4187, May 2000.

[36] H. Sagan,*Space-Filling Curves*. New York: Springer-Verlag, 1994.

[37] J. McVay, N. Engheta, and A. Hoorfar, "High impedance metamaterial surfaces using hilbert-curve inclusions," *IEEE Microwave and Wireless Components Letters,* vol.14, no.3, pp. 130-132, Mar. 2004.

[38] S.Y.Zhan and R.J.Weber, "A low profile metal-surface mounted RFID tag antenna with a slotted inverted-L shape," submitted to IPDR for patent application with a case number of ISURF#03567, Aug. 2007.

[39] S.Y.Zhan and R.J.Weber, "An ultra thin and high gain metal-surface mounted RFID tag antenna with a symmetrically slotted patch," submitted to IPDR for patent application with a case number ISURF #03568, Aug. 2007.

[40] L. Ukkonen, D. Engels, L. Sydanheimo, and M. Kivikoski, "Planar wire-type inverted- F RFID tag antenna mountable on metallic objects," *2004 IEEE AP-S International Symposium*, Monterey, California, vol. 1, pp. 101-104, June 20-26, 2004.

[41] M. Hirvonen, P. Pursula, K. Jaakkola, and K. Laukkanen, "Planar inverted-F antenna for radio frequency identification," *Electronic Letters*, vol. 40, no. 14, pp.848-850, July 2004.

[42] H. Kwon and B. Lee, "Compact slotted planar inverted-F RFID tag mountable on metallic objects," *Electronic Letters*, vol. 41, no. 24, pp.1308-1310, Nov. 2005.

[43] W. Choi, H. W. Son, J.Bae, G. Choi, C.Pyo, and J. Chae. "An RFID tag using a planar inverted-F antenna capable of being stuck to metallic objects," *ETRI Journal*, vol 28, no. 2, pp. 216-218, April 2006.

[44] H. -W. Son, G.-Y. Choi, and C. –S. Pyo, "Design of wideband RFID tag antenna for metallic Surfaces,"*Electronic Letters*, vol. 42, no. 5, pp. 263-265, Mar. 2006.

[45] J.S. Kuo and K. L. Wong, "Dual-frequency operation of a planar inverted-L antenna with tapered patch width," *Microwave Opt Technol Lett*, vol. 28, no. 2, pp. 126-127, Jan. 2001.

[46] http://www.ittc.ku.edu/publications/KU-Tag_flyer.pdf, 2007.

[47] D.K.Cheng, *Field and Wave Electromagnetics* , 2nd ed, Reading, MA, Addison-Wesley, 1989.

# ACKNOWLEDGEMENTS

I would like to express my gratitude to all of the people who have made my PhD study in Iowa State University (ISU) possible and made it a rewarding experience. I appreciate that Prof. John R. Bowler first brought me to ISU and introduced me to the fantastic world of numerical electromagnetics. I would like to thank my major professors: Prof. Rober J. Weber and Prof. Jiming Song, for their guidance, numerous suggestions and encouragement. I would also like to thank Profs. Akhilesh Tyagi and Jaeyoun Kim for spending their precious time to serve as my committee members. I would like to express my appreciation to Prof. Arun K. Somani and Prof. Srinivas Aluru for their time and generous help.

This work is funded by Metalcraft and IPRT company assistance.